

**AFRL-SN-RS-TR-2001-52**

**In-House Report**

**June 2001**



## **NOVEL DIVERSE WAVEFORMS**

**Paul A. Antonik, Hugh Griffiths, Donald D. Weiner and Michael C. Wicks**

*APPROVED FOR PUBLIC RELEASE; DISTRIBUTION UNLIMITED.*

**20010810 025**

**AIR FORCE RESEARCH LABORATORY  
SENSORS DIRECTORATE  
ROME RESEARCH SITE  
ROME, NEW YORK**

This report has been reviewed by the Air Force Research Laboratory, Information Directorate, Public Affairs Office (IFOIPA) and is releasable to the National Technical Information Service (NTIS). At NTIS it will be releasable to the general public, including foreign nations.

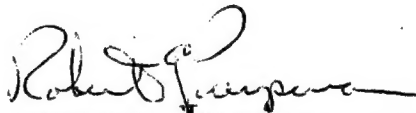
AFRL-SN-RS-TR-2001-52 has been reviewed and is approved for publication.

APPROVED:



GERARD J. GENELLO, Chief  
Radar Signal Processing Branch

FOR THE DIRECTOR:



ROBERT E. PURPURA, Acting Chief  
Rome Operations Office  
Sensors Directorate

If your address has changed or if you wish to be removed from the Air Force Research Laboratory Rome Research Site mailing list, or if the addressee is no longer employed by your organization, please notify AFRL/SNRT, 26 Electronic Pky., Rome, NY 13441-4514. This will assist us in maintaining a current mailing list.

Do not return copies of this report unless contractual obligations or notices on a specific document require that it be returned.

REPORT DOCUMENTATION PAGE			Form Approved OMB No. 0704-0188	
Public reporting burden for this collection of information is estimated to average 1 hour per response, including the time for reviewing instructions, searching existing data sources, gathering and maintaining the data needed, and completing and reviewing the collection of information. Send comments regarding this burden estimate or any other aspect of this collection of information, including suggestions for reducing this burden, to Washington Headquarters Services, Directorate for Information Operations and Reports, 1215 Jefferson Davis Highway, Suite 1204, Arlington, VA 22202-4302, and to the Office of Management and Budget, Paperwork Reduction Project (0704-0188), Washington, DC 20503.				
1. AGENCY USE ONLY (Leave blank)	2. REPORT DATE JUNE 2001	3. REPORT TYPE AND DATES COVERED In-House Mar 99 - Feb 01		
4. TITLE AND SUBTITLE NOVEL DIVERSE WAVEFORMS		5. FUNDING NUMBERS PE - 62204F PR - 7622 TA - SN WU - 00		
6. AUTHOR(S) Paul A. Antonik, Hugh Griffiths, Donald D. Weiner, Michael C. Wicks				
7. PERFORMING ORGANIZATION NAME(S) AND ADDRESS(ES) AFRL/SNRT 26 Electronic Pky Rome NY 13441-4514		8. PERFORMING ORGANIZATION REPORT NUMBER  AFRL-SN-RS-TR-2001-52		
9. SPONSORING/MONITORING AGENCY NAME(S) AND ADDRESS(ES) AFRL/SNRT 26 Electronic Pky Rome NY 13441-4514		10. SPONSORING/MONITORING AGENCY REPORT NUMBER  AFRL-SN-RS-TR-2001-52		
11. SUPPLEMENTARY NOTES  Air Force Research Laboratory Project Engineer: Michel C. Wicks, SNRT, 315-330-2556				
12a. DISTRIBUTION AVAILABILITY STATEMENT Approved for public release: Distribution unlimited.			12b. DISTRIBUTION CODE	
13. ABSTRACT (Maximum 200 words) Use of an interferometer along with a host radar is proposed for simultaneously achieving coherent reference denial and embedded communications. To prevent self-jamming, spatial orthogonality is achieved between the interferometer antenna pattern and main beam of the host radar. Costas and orthogonal frequency division multiplexing (OFDM) signals are suggested for the host radar and interferometer, respectively. Effectiveness of the interferometer masking signal on a non-cooperative bistatic radar is discussed.				
14. SUBJECT TERMS Radar, communications, waveforms, signal processing, coherent reference denial			15. NUMBER OF PAGES 149	
			16. PRICE CODE	
17. SECURITY CLASSIFICATION OF REPORT UNCLASSIFIED	18. SECURITY CLASSIFICATION OF THIS PAGE UNCLASSIFIED	19. SECURITY CLASSIFICATION OF ABSTRACT UNCLASSIFIED	20. LIMITATION OF ABSTRACT UL	

## TABLE OF CONTENTS

Table of Contents .....	i-ii
Table of Figures .....	iii-v
List of Tables .....	vi
1 Introduction .....	1/2-4
1.1 Background .....	1/2
1.2 Proposed Methodology .....	1/2
1.3 Research Objectives .....	3
1.4 Report Organization .....	4
2 Non-Cooperative Bistatic Radar Considerations .....	5-15
2.1 Bistatic Radar Fundamentals .....	5
2.2 Synchronization Issues for a Non-Cooperative Bistatic Receiver .....	8
2.2.1 Transmitter Location .....	9
2.2.2 Antenna Polarization .....	9
2.2.3 Carrier Frequency .....	9
2.2.4 Antenna Beam Pattern and Beamwidth .....	9
2.2.5 Antenna Scan Characteristics .....	9
2.2.6 Complex Envelope Waveform .....	9
2.3 Coherent Reference Denial .....	10
3 Interferometer and Host Radar Antenna Patterns .....	16-65
3.1 Interferometer Antenna Pattern .....	16
3.2 Main Radar Antenna Pattern .....	29
3.3 Steering the Interferometer Along With Positioning the Broad Null .....	34
3.3.1 Steering the Interferometer .....	34
3.3.2 Positioning the Broad Null by Steering the Interferometer .....	37
3.3.3 Placement of the Interferometer Along the y Axis .....	39
3.3.4 Evaluation of Broad Null at $\alpha=0^\circ$ .....	42
3.3.5 Comparison of the Interferometer and Radar Field Strengths Broadside to the Radar ....	46
3.4 Use of Frequency Modulated Signals to Steer the Interferometer .....	48
3.4.1 Quasi-Stationary Considerations .....	50
3.4.2 The Time Variant Array Factor for a Chirp Signal Applied to the Interferometer Elements	52
3.4.3 The Time Variant Array Factor for Two Different Chirp Signals Applied to the Interferometer Elements .....	59

3.4.4	The Time Variant Array Factor for a Frequency-Hopped Signal Applied to the Interferometer Elements .....	62
4	A Radar Waveform Employing Frequency Diversity .....	66-87
4.1	Frequency-Hopped Waveforms .....	66
4.2	The Permutation Matrix .....	67
4.3	Costas Arrays .....	69
4.4	Ambiguity Function of the Costas Signal .....	73
5	An Interferometer Waveform Employing Orthogonal Frequency Division Multiplexing .....	88-111
5.1	Orthogonal Frequency Division Multiplexing .....	88
5.1.1	Overview of OFDM .....	88
5.1.2	OFDM Signal Characterization .....	89
5.1.3	OFDM Signal Recovery Employing a Guard Interval .....	90
5.1.4	Use of Fast Fourier Transform in OFDM Implementation .....	92
5.1.5	Modulation and Demodulation Without Differential Encoding .....	95
5.1.6	Modulation and Demodulation With Differential Encoding .....	96
5.1.7	M-ary Differential Amplitude and Phase Shift Keying .....	98
5.2	Ambiguity Function of the OFDM Signal .....	103
6	Non-Cooperative Bistatic Radar Receiver Performance .....	112-133
6.1	Cross Ambiguity Function for the Costas and OFDM Signals .....	112
6.2	Non-Cooperative Bistatic Radar Detection Statistic Involving the Costas and OFDM Signals ....	113
6.3	Non-Cooperative Bistatic Radar Receiver Performance .....	127
6.3.1	False Alarm Probability .....	127
6.3.2	Detection Probability .....	130
7	Conclusions .....	134-136
7.1	Summary .....	134
7.2	Suggestions for Future Work .....	135
7.2.1	Performance Evaluation of the Complete System Using Realistic Scenarios .....	135
7.2.2	Extension of the Interferometer to More Than Two Elements .....	135
7.2.3	Generalization of the Ambiguity Function to Include Direction of Arrival .....	136
References	.....	137

## TABLE OF FIGURES

1.1	Non-cooperative bistatic receivers require a coherent reference from the host illuminator .....	1/2
1.2	A pair of interferometric elements driven by independent waveform generation, timing and control provides a means to modulate the sidelobes of the host radar main array .....	3
1.3	Pulse-to-pulse phase modulation of the sidelobes denies a coherent reference to non-cooperative receivers. The sidelobe modulation, also, permits embedded communications .....	3
2.1	A bistatic receiver employs separate antennas for transmitting and receiving .....	5
2.2	Bistatic radar geometry is described using the north-referenced coordinate system .....	5
2.3	The bistatic Doppler frequency depends upon the angle between the velocity vector and the bistatic angle bisector .....	7
2.4	The monostatic Doppler frequency depends upon the angle between the velocity vector and the radial line from the target to the radar .....	7
3.1	Both Cartesian and spherical coordinates are used to characterize a point in the far field of the interferometer .....	16
3.2	Each antenna in the interferometer pair consists of a dipole antenna of length, $\ell$ .....	17
3.3	The dipole antennas are placed along the x-axis at A and B and are directed in the z-direction .....	17
3.4	When P is in the near field of the interferometer, the geometry is relatively complicated .....	18
3.5	The geometry simplifies as P moves to the far field .....	18
3.6	When a linear array is placed on the x-axis, the azimuth angle, $\alpha$ , in the array literature is typically measured from the y-axis .....	20
3.7	Radiation patterns are plotted for the dipole antenna with $\ell \leq \lambda_0$ .....	21
3.8	The dipole antenna radiation pattern is plotted for $\ell = 1.25\lambda_0$ .....	22
3.9	The dipole antenna radiation pattern is plotted for $\ell = 1.5\lambda_0$ .....	22
3.10	The antenna configuration consists of a linear grid with equal spacing, d. The main radar array is composed of N elements where N can be either an (a) odd or (b) even integer .....	23
3.11	The azimuthal radiation pattern of the interferometer array factor is plotted for $d = \lambda_0/2$ , $\theta_0 = \pi/2$ , and $d_{IFM}$ equal to (a) $3\lambda_0/2$ , (b) $2\lambda_0$ , (c) $5\lambda_0/2$ , (d) $3\lambda_0$ , (e) $7\lambda_0/2$ , and (f) $4\lambda_0$ .....	26
3.12	The Cartesian plot of $F_{IFM}(\pi/2, \alpha)$ , corresponding to $N=2$ , illustrates the broad null that appears at $\alpha = 90^\circ$ .....	27
3.13	The azimuthal radiation pattern of the interferometer array factor is plotted for $d = \lambda_0/2$ , $\theta_0 = \pi/6$ , and $d_{IFM}$ equal to (a) $3\lambda_0/2$ , (b) $2\lambda_0$ , (c) $5\lambda_0/2$ , (d) $3\lambda_0$ , (e) $7\lambda_0/2$ , and (f) $4\lambda_0$ .....	28
3.14	The vertical radiation pattern of the interferometer array factor is plotted for $d = \lambda_0/2$ , $\alpha_0 = \pm\pi/2$ , and $d_{IFM}$ equal to (a) $3\lambda_0/2$ , (b) $2\lambda_0$ , (c) $5\lambda_0/2$ , (d) $3\lambda_0$ , (e) $7\lambda_0/2$ , and (f) $4\lambda_0$ .....	29
3.15	The azimuthal radiation pattern of the interferometer array factor is plotted for $d = \lambda_0/2$ , $\theta = \pi/2$ , and $N=6$ .....	33

3.16	The azimuthal radiation pattern of the interferometer array factor is plotted when the major lobe at $\alpha=0^\circ$ in Figure 3.11 is steered to $\alpha = 10^\circ$ for $d = \lambda_0/2$ , $\theta_0 = \pi/2$ , and $d_{IFM}$ equal to (a) $3\lambda_0/2$ and (b) $4\lambda_0$ ...	37
3.17	The azimuthal radiation pattern of the interferometer array factor is plotted when nulls in Figure 3.11 are steered to $\alpha = 0^\circ$ for $d = \lambda_0/2$ , $\theta_0 = \pi/2$ , and $d_{IFM}$ equal to (a) $3\lambda_0/2$ and (b) $2\lambda_0$ .....	38
3.18	The dipole antennas are placed along the y-axis at A and B are directed in the z-direction .....	40
3.19	The geometry is shown for evaluation of the electric field at point, P .....	40
3.20	The azimuthal radiation pattern of the interferometer array factor, where the elements are on the y-axis, is plotted for $\theta = \pi/2$ , and $d_{IFM}$ equal to (a) $3\lambda_0/2$ , (b) $5\lambda_0/2$ , and (c) $7\lambda_0/2$ .....	42
3.21	The vertical radiation pattern of the interferometer array factor, where the elements are on the y-axis, is plotted for $\alpha=0^\circ$ and $d_{IFM}$ equal to (a) $3\lambda_0/2$ , (b) $5\lambda_0/2$ , and (c) $7\lambda_0/2$ .....	45
3.22	The azimuthal radiation pattern of the interferometer array factor, where the elements are on the y-axis, is plotted for $\theta = \pi/2$ , $d_{IFM} = 21 \lambda_0/2$ , and $(\Delta f(t)/f_0)$ equal to (a) 0, (b) 0.01, and (c) 0.001 ...	56
3.23	When up and down chirps are applied to the two interferometer elements, the electric field at a fixed point in the far field is a suppressed carrier amplitude modulated signal whose modulation is a linear frequency modulated waveform, as sketched in the figure .....	62
3.24	The azimuthal radiation pattern of the interferometer array factor is plotted for a frequency-hopped excitation with $\theta = \pi/2$ , $k_s=21$ , and $\Delta k_i$ equal to (a) -2, (b) 0, and (c) +2 .....	65
3.25	Positions of the major lobes, indicated by x's, and nulls, indicated by o's, are shown for the three patterns plotted in Figure 3.24 .....	65
4.1	The frequencies of a frequency-hopped pulse may be either (a) consecutive or (b) scrambled .....	67
4.2	The permutation matrix for a stepped frequency linear FM waveform has nonzero entries only along one of the diagonals .....	68
4.3	The permutation matrix shown is one of 200 possible Costas arrays for $N=7$ .....	70
4.4	The ambiguity matrix is shown for the Costas array of Figure 4.3 .....	70
4.5	This difference triangle can be used to construct the ambiguity matrix presented in Figure 4.4 .....	71
4.6	The ambiguity function of the Costas signal generated from the Costas array of Figure 4.3 approximates the shape of a thumbtack .....	72
4.7	Ambiguity matrix does not predict minor peaks along the time shift axis for zero frequency shift ...	72
4.8	Various views of the ambiguity surface for the 10-pulse Welch code are shown: (a) an overview, (b) a different perspective, (c) Doppler response for $x=0$ , (d) delay response for $y=0$ , (e) pedestal region near the highest sidelobe peak .....	83
4.9	Various views of the ambiguity surface for the 30-pulse Welch code are shown: (a) an overview, (b) plot using only integer values for $x$ and $y$ , (c) Doppler response at $x=0$ , (d) delay response at $y=0$ , (e) complete delay axis response, (f) Doppler response at $x=25$ , (g) Doppler response at $x=5$ , (h) Doppler response at $x=1.4$ , (i) pedestal region near the highest sidelobe peak .....	85
4.10	The ambiguity surface is shown for a 10-pulse frequency stepped linear FM signal with spacing equal to $1/T$ .....	87
5.1	The guard and message intervals are shown for (a) the direct path signal and (b) the maximally delayed multipath signal .....	92
5.2	An OFDM communication system typically employs fast Fourier transform techniques, coding, and channel estimation .....	95

5.3	The signal space contains 64 possible symbols when there are 4 possible amplitudes and 16 possible phases .....	99
6.1	$E[ I_7 ^2]$ is evaluated by integrating over the regions indicated .....	122
6.2	A target is declared present when $ L ^2$ falls into the shaded region .....	129
7.1	The tri-element interferometer can be viewed as an equivalent two-element interferometer .....	136



## LIST OF TABLES

3.1	Comparison of Steered Null to Broad Null at $\alpha = 0^\circ$ for $d_{\text{IFM}} = 3\lambda_0/2$ .....	43
3.2	Evaluation of Broad Nulls at $\alpha = 0^\circ$ for $d_{\text{IFM}} = 5\lambda_0/2$ and $7\lambda_0/2$ .....	44
3.3	Evaluation of Broad Nulls at $\theta = 90^\circ$ for $d_{\text{IFM}} = 3\lambda_0/2$ , $5\lambda_0/2$ , and $7\lambda_0/2$ .....	45
3.4	Evaluation of Radar Main Beam .....	47
3.5	Ratio of Interferometer to Radar Electric Field Magnitudes in the Main Beam of the Radar for $d_{\text{IFM}} = 3\lambda_0/2$ , $5\lambda_0/2$ , and $7\lambda_0/2$ .....	48
3.6	Comparison of Major Lobe Positions in First Quadrant for a 1% change in Carrier Frequency. ....	57
3.7	Comparison of Major Lobe Positions in First Quadrant for a 0.1% change in Carrier Frequency ....	58
4.1	Number and Density of Costas Arrays .....	69
5.1	Differential Amplitude Modulation for $p_a = 2$ .....	100
5.2	Optimal Modulation Parameters for Differential Encoding .....	100
5.3	Differential Amplitude Modulation for $p_a = 2$ Without Modulo Arithmetic .....	101
5.4	Thresholding Scheme for Evaluation of Amplitude Information Bits .....	102

## CHAPTER 1

### INTRODUCTION

#### 1.1 Background

The US Air Force has invested heavily in the development of advanced surveillance systems and technologies. Of increasing concern is the threat that potential adversaries may use bistatic technologies to take advantage of our significant investment in advanced sensors. With relatively inexpensive receiver systems, an adversary could host off of our illuminations to operate bistatically. A central requirement for non-cooperative bistatic operation is the estimation of a coherent reference signal. This estimate is used to correlate against received waveforms to extract the desired signal. As illustrated in Figure 1.1, a coherent reference is typically obtained by measuring a direct path signal through the sidelobes of the illuminator. Conventional methods to prevent the interception of the direct path signal include low sidelobe antennas, physical isolation, and the use of spread spectrum waveforms. These methods will become inadequate as surveillance sensors migrate to space.

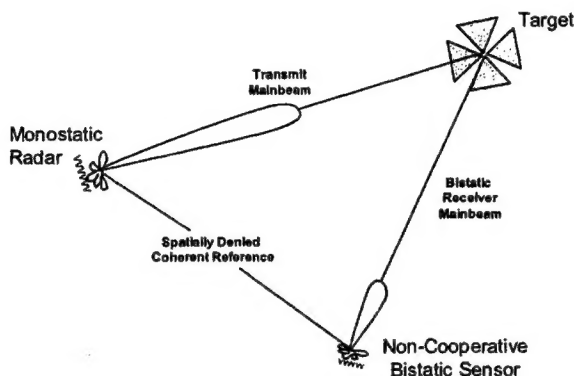


Figure 1.1: Non-cooperative bistatic receivers require a coherent reference from the host illuminator

In addition, to enhance precision engagement, it is desirable that covert data/voice communication be incorporated simultaneously with the surveillance function. This embedded communications capability should allow for the message signal to vary with angle such that separate information can be directed to different receivers located at various angles. Directionally dependent waveforms would be ideal for space based sensing of RF tags on aircraft (IFF), ground equipment and troops and would be especially valuable for search and rescue missions. Of course, the radar and communications waveforms should be designed so that they can be radiated at the same time without self-jamming.

#### 1.2 Proposed Methodology

As shown in Figure 1.2, it is proposed to employ an  $(N+2)$  element antenna array where  $N$  of the elements are used by the host radar for surveillance purposes while two of the elements are used by the interferometer for coherent reference denial and communications purposes. The two interferometric elements are driven separately with an independent waveform generation, timing and control circuit.

Ideally, the interferometer antenna pattern will overlay the sidelobes of the host radar main antenna pattern with minimal overlay of the radar main beam. The interferometer may or may not be on all of the time. However, as a minimum, the interferometer will be on while the host radar is in the transmit mode with the objective that the interferometer signal will mask that portion of the host radar signal emitted through the radar sidelobes. In this way, a coherent reference signal is denied to a non-cooperative bistatic receiver.

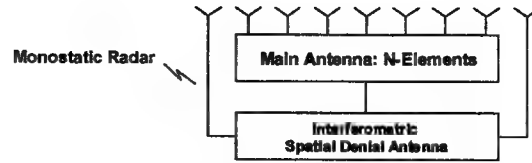


**Figure 1.2:** A pair of interferometric elements driven by independent waveform generation, timing and control provides a means to modulate the sidelobes of the host radar main array.

To increase the effectiveness of this masking, it is also proposed to modulate the interferometer antenna pattern from pulse to pulse such that the pattern is rotated on each pulse. This is illustrated in Figure 1.3. Due to the nature of the interferometer modulation, the proposed method of denying a coherent reference is more effective than masking the sidelobes with a noise signal.

Also, by carefully selecting the interferometer modulation, a desired message signal can be embedded in the sidelobes, thereby allowing data/voice communications operations simultaneously with the surveillance function. Using a multi-channel phased array antenna and orthogonal spatial-temporal waveforms, the message signal can vary with angle. In this manner, separate communications signals can be directed to different receivers located at various angles.

### 1.3 Research Objectives

The objectives of this research effort are summarized below:

- 1) Develop joint spatial-temporal antenna-based signal processing techniques and waveforms that can be applied simultaneously to radar and communications systems without self jamming,
- 2) Design multi-dimensional waveforms for the purposes of denying a coherent reference to a non-cooperative bistatic radar located at an arbitrary angle while simultaneously permitting radar surveillance and multiple embedded communications,
- 3) Design diverse waveforms which will accommodate multi-mission operations such as ground and airborne moving target indication, tracking, automatic target recognition, and foliage and ground penetration,
- 4) Investigate theoretical measures of performance for sensor and communication systems incorporating these new and novel waveforms.

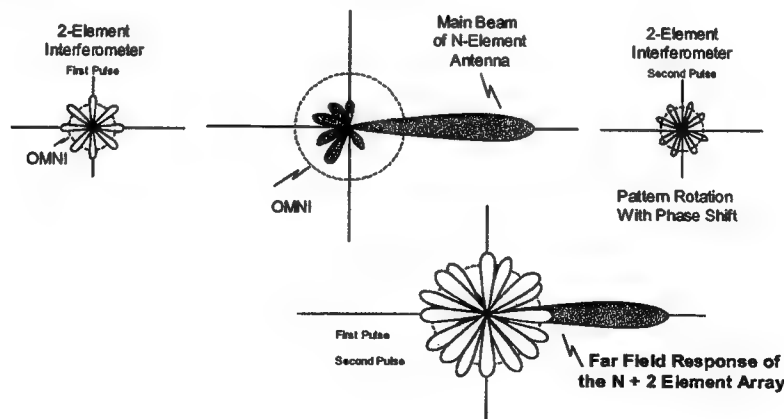


**Figure 1.3:** Pulse-to-pulse phase modulation of the sidelobes denies a coherent reference to non-cooperative receivers. The sidelobe modulation, also, permits embedded communications.

## 1.4 Report Organization

Bistatic radar fundamentals are reviewed in Chapter 2. Various issues associated with the successful operation of a non-cooperative bistatic radar are discussed. Use of the interferometer signal to mask the direct signal of the host radar is then considered. Performance degradation of the non-cooperative bistatic radar is shown to depend upon the delay-Doppler ambiguity functions of the host radar and interferometer waveforms and their cross ambiguity function.

Antenna patterns of the interferometer and host radar are developed in Chapter 3. It is noted that it is possible to achieve spatial orthogonality between the host radar and interferometer by placing a broad null of the interferometer pattern in the direction of the main beam of the host radar. However, it is shown that frequency hopping is required to steer the interferometer pattern while maintaining the broad null. Various waveforms are considered for the signals driving the interferometer. Conditions required by the wave equation are investigated for the quasi-stationary behavior of an antenna when modulated signals are radiated. Response of the interferometer element pair when excited by two different modulated signals is derived. This is specialized to the situation where both elements are excited by the same linear frequency modulated pulse. In addition, the case is considered where one of the interferometer signals is an up chirp while the other is a down chirp.

A frequency-coded waveform, employing Costas sequences, is proposed for the host radar signal in Chapter 4. The concept of the Costas array is introduced and the delay-Doppler ambiguity function of the Costas signal is derived. The ambiguity function is shown to have a thumbtack-like shape (i.e., a single narrow central peak surrounded by a low-level pedestal).

Orthogonal frequency division multiplexing (OFDM) is chosen as the modulation scheme for the interferometer in Chapter 5. After a tutorial discussion of OFDM, the delay-Doppler ambiguity function of the OFDM signal is derived.

Performance of the non-cooperative bistatic radar is considered in Chapter 6 assuming that the host radar and interferometer employ Costas and OFDM signals, respectively. This requires derivation of the delay-Doppler cross ambiguity function between the Costas and OFDM signals. Expressions are obtained for the false alarm and detection probabilities of the non-cooperative bistatic radar.

Finally, a summary of results and suggestions for future work are provided in Chapter 7.

## CHAPTER 2

### NON-COOPERATIVE BISTATIC RADAR CONSIDERATIONS

#### 2.1 Bistatic Radar Fundamentals [1]

A bistatic radar is one in which the transmitter and receiver are physically separated and, therefore, have separate antennas, as shown in Figure 2.1. The north-referenced coordinate system, which is illustrated in Figure

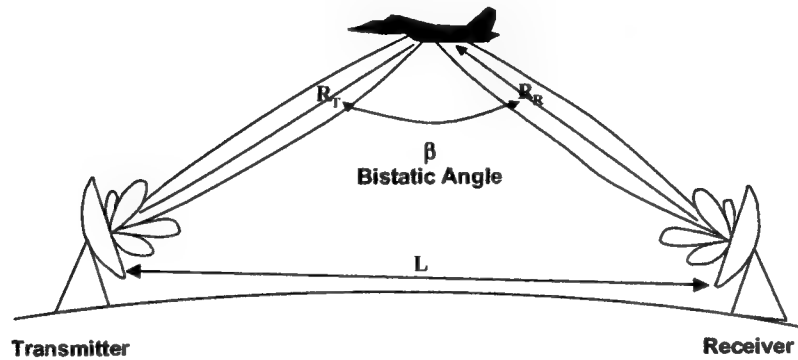


Figure 2.1: A bistatic receiver employs separate antennas for transmitting and receiving.

2.2, is frequently used to describe the bistatic radar geometry. The bistatic baseline is denoted by  $L$  and designates the distance separating the transmitter and receiver.  $R_T$  and  $R_R$  denote the distance from the transmitter to the target and the distance from the target to the receiver, respectively. The bistatic angle,  $\beta$ , is measured at the target and is the angle between the lines whose lengths are denoted by  $R_T$  and  $R_R$ .

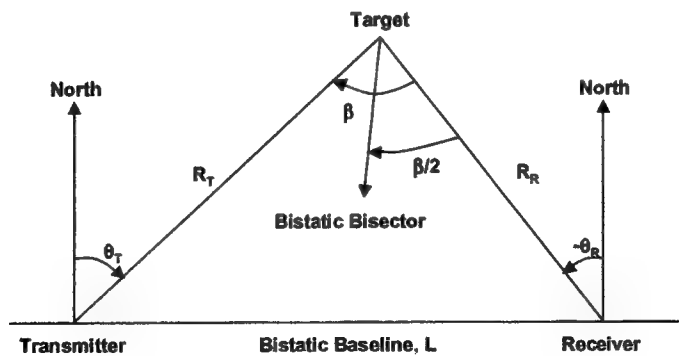


Figure 2.2: Bistatic radar geometry is described using the north-referenced coordinate system.

The direct-path delay between the transmitter and receiver is

$$\tau^{DP} = \frac{L}{c} \quad (2.1)$$

where  $c$  is the speed of light. The total delay related to the detection of a point target is

$$\tau^{TP} = \frac{R_T + R_R}{c} \quad (2.2)$$

The bistatic delay is defined to be the difference between the total delay and the direct-path delay and is given by

$$\tau_B = \tau^{TP} - \tau^{DP} = \frac{R_T + R_R - L}{c} \quad (2.3)$$

Thus, the bistatic delay is a measure of the bistatic range which is defined to be

$$BR = R_T + R_R - L \quad (2.4)$$

The locus of constant bistatic range is an ellipsoid whose foci are located at the transmitter and receiver. The major semi-axis length is given by

$$a = \frac{L + BR}{2} = \frac{R_T + R_R}{2} \quad (2.5)$$

while the minor semi-axis lengths are equal and given by

$$b = \sqrt{a^2 - L^2/4} \quad (2.6)$$

For the special case of a monostatic radar,

$$L = \tau^{DP} = 0 \quad (2.7)$$

and the ellipsoid becomes a sphere of radius  $R_R = R_T$ . The monostatic delay related to a point target is

$$\tau_m = \frac{2R_T}{c} = \frac{2R_R}{c} \quad (2.8)$$

The Doppler frequency observed in the received signal is proportional to the time derivative of the bistatic range. Let the target velocity vector be denoted by  $\vec{v}$ . Assuming a stationary transmitter and receiver,  $(dL/dt) = 0$ . The time derivative of the bistatic range is then given by

$$\frac{d(BR)}{dt} = -2|\vec{v}| \cos \delta \cos(\beta/2) \quad (2.9)$$

where  $\delta$  is the angle between the velocity vector and the bistatic angle bisector, as illustrated in Figure 2.3. Hence, the bistatic Doppler frequency is

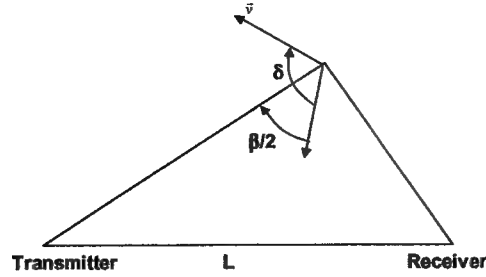


Figure 2.3: The bistatic Doppler frequency depends upon the angle between the velocity vector and the bistatic angle bisector.

$$f_B = -\frac{1}{\lambda_o} \frac{d(BR)}{dt} = \frac{2|\vec{v}|}{\lambda_o} \cos \delta \cos(\beta/2) \quad (2.10)$$

where  $\lambda_o$  is the wavelength of the propagating wave. Observe that  $|\vec{v}| \cos \delta$  is the projection of the velocity vector on the bistatic angle bisector. It represents the velocity component perpendicular to the constant range ellipsoid. Along the bistatic baseline,  $\beta = 180^\circ$  and the target Doppler frequency is always zero independent of the velocity vector orientation.

For a monostatic radar,  $\beta = 0^\circ$ . The Doppler frequency becomes

$$f_m = \frac{2|\vec{v}|}{\lambda_o} \cos \delta \quad (2.11)$$

where  $\delta$  is now the angle between the velocity vector and the radial line between the target and the radar. The monostatic Doppler frequency geometry is shown in Figure 2.4.

The bistatic triangle of Figure 2.2 is readily solved to locate the target position relative to the transmitter and receiver. Three pieces of information are needed to completely and unambiguously specify a triangle, one of which must be the length of a side. Given  $L$ , then any two of  $BR$ ,  $\theta_T$ , and  $\theta_R$  can be used to solve the triangle to locate the target. For example, using  $BR$  and  $\theta_R$ ,

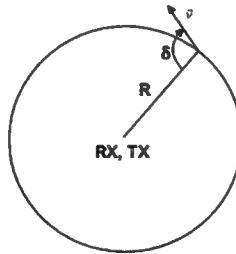


Figure 2.4: The monostatic Doppler frequency depends upon the angle between the velocity vector and the radial line from the target to the radar.

$$R_R = \frac{(BR)^2 + 2L(BR)}{2[BR + L(1 + \sin \theta_R)]} \quad (2.12)$$

In a similar manner, using BR and  $\theta_T$ ,

$$R_T = \frac{(BR)^2 + 2L(BR)}{2[BR + L(1 - \sin \theta_T)]}. \quad (2.13)$$

In addition, from Figure 2.2,

$$\beta = \theta_T - \theta_R. \quad (2.14)$$

Using the law of sines, it follows that

$$\frac{\sin \beta}{L} = \frac{\cos \theta_R}{R_T} = \frac{\cos \theta_T}{R_R}. \quad (2.15)$$

As a result, knowledge of any three of the four parameters  $\theta_T$ ,  $\theta_R$ , L, and BR is sufficient to determine the fourth. Also, it can be shown using the law of sines that

$$R_R = \frac{(BR + L) \cos \theta_T}{\cos \theta_R + \cos \theta_T}. \quad (2.16)$$

and

$$R_T = \frac{(BR + L) \cos \theta_R}{\cos \theta_R + \cos \theta_T}. \quad (2.17)$$

Finally, the distance along the baseline can be expressed as

$$L = \frac{(BR + L) \sin(\theta_T - \theta_R)}{\cos \theta_R + \cos \theta_T}. \quad (2.18)$$

The discussion in this section assumed that the bistatic radar transmitter and receiver were designed to be used together and are synchronized for maximum performance. Synchronization issues for the case of a non-cooperative bistatic radar receiver, where the receiver attempts to "hitchhike" off of an independent source of illumination, is discussed in Section 2.2. This mode of operation is termed "non-cooperative" because the transmitter is not designed to support bistatic radar operation.

## 2.2 Synchronization Issues for a Non-Cooperative Bistatic Radar Receiver [2,3]

In order to maximize the radar coverage and detection sensitivity of a non-cooperative bistatic radar receiver, the receiver must either know or be able to estimate the following transmitter parameters:

- 1) Transmitter location,
- 2) Antenna polarization,
- 3) Carrier frequency,
- 4) Antenna beam pattern and beamwidth,
- 5) Antenna scan characteristics,
- 6) Complex envelope waveform.

Each of these requirements is briefly discussed in this section.



### **2.2.1 Transmitter Location**

As pointed out in Section 2.1, solution of the bistatic triangle requires knowledge of the transmitter position. This can be determined in a variety of ways. Although non-cooperative, the transmitter's location may be known a priori. For instance, the position of airport surveillance radars may be found in various data bases. When not known, the transmitter's location can be estimated using emitter location techniques. Such techniques typically involve multiple receiver sites or a moving platform and are generally good enough so as not to significantly affect target location accuracies.

### **2.2.2 Antenna Polarization**

The antenna polarization may be known a priori in some cases. Otherwise, the polarization can be determined by measuring the direct path signal using antennas matched to various polarizations. When this is not possible, a 45° slant polarized antenna may be used as a compromise by the bistatic radar receiver.

### **2.2.3 Carrier Frequency**

Waveform power can be maximized by tuning the bistatic radar receiver to the known or estimated carrier frequency of the transmitted waveform. Techniques for determining the carrier frequency of an unknown waveform are well known and have been implemented in electronic support measures (ESM) receivers. In fact, frequency estimation can be done with a higher accuracy than is required for good bistatic radar operation. It can, also, be done very rapidly. For example, frequency can be measured on a pulse-to-pulse basis by a technique known as instantaneous frequency measurement (IFM). This becomes essential when hosting off radars that are pulse-to-pulse frequency agile.

### **2.2.4 Antenna Beam Pattern and Beamwidth**

It is desirable to integrate all of the pulses that the mainbeam places on the target. Knowledge of the beamwidth is necessary to set the dwell time or, equivalently, the coherent processing interval (CPI). The transmitted pulse amplitudes are modulated by the scanning of the transmitter beam for long dwells. Reasonable knowledge of the transmitting antenna beam pattern becomes necessary to do a good job of matched filtering. Beamwidth is another parameter that can be measured by ESM systems. This is generally derived by monitoring the envelope of the transmitted pulses over a scan. It appears that an accuracy within 25% is sufficient to maintain good bistatic radar receiver performance.

### **2.2.5 Antenna Scan Characteristics**

In order for the antenna of the bistatic radar receiver to be pointing at the volume of space simultaneously illuminated by the transmitter, it is necessary to know the transmitter scan characteristics. This is referred to as pulse chasing. For mechanically-scanned radars, rotating at a constant angular rate, the scan rate of the transmitter is estimated by tracking the times when the mainbeam flashes past the receiver. Knowledge of the scan time enables estimates to be made of the azimuth angle toward which the transmitter antenna is pointing at any time instant. Generally, it is not possible to synchronize a bistatic radar receiver to the elevation scanning of a transmitter unless a known regular elevation scan pattern is used. To overcome this lack of knowledge, the bistatic radar receiver typically uses a receive aperture with an elevation fan beam which covers all elevations of interest.

### **2.2.6 Complex Envelope Waveform**

The complex envelope of the transmitted waveform, which contains the amplitude and phase modulation of the radar pulse, must be estimated for use in cross correlation with the radar signal. In addition, approximations to the pulsewidth and the timing of pulses, which may or may not be staggered, are needed to successfully perform the operations of Doppler processing, pulse compression, and matched filtering.

As pointed out in Chapter 1, one of the objectives of this effort is to use the interferometer signal to disrupt to the extent possible the synchronization of the non-cooperative bistatic radar receiver with the host radar.

### 2.3. Coherent Reference Denial

In this report it is assumed that the non-cooperative bistatic radar receiver performs detection by utilizing an estimate of the host radar transmitted signal for correlation with the received data. In practice, the estimate should be continuously updated in order to account for pulse-to-pulse amplitude, frequency, and phase variations that may or may not be intentional.

The estimate of the host radar transmitted complex envelope is typically obtained from the direct path signal observed by the bistatic radar receiver. In general, the direct path signal is corrupted by clutter and receiver noise which, in some cases, can be sufficient to cause significant signal processing losses due to poor estimates of the host radar complex envelope. However, for our purposes, it will be assumed that the interferometer signal is mainly responsible for degradation of the complex envelope estimate. In this way, there is no reliance solely on the clutter and receiver noise to prevent the non-cooperative bistatic radar receiver from hosting off of the monostatic radar. Of course, to the extent that the clutter and receiver noise help to mask the transmitted radar waveform in the direct path, the more difficult it will be for the non-cooperative bistatic radar receiver to operate successfully.

With reference to Figure 1.2, let the transmitted host radar and interferometer complex envelopes be denoted by  $s_{RAD}(t)$  and  $s_{IFM}(t)$ , respectively. By definition, the energies of these signals are given by

$$E_{RAD} = \int_0^{T_d} |s_{RAD}(t)|^2 dt \quad (2.19)$$

and

$$E_{IFM} = \int_0^{T_d} |s_{IFM}(t)|^2 dt \quad (2.20)$$

where both signals are assumed to be of the same duration,  $T_d$ . To account explicitly for the signal energies, it is convenient to introduce the unit energy signals  $f_{RAD}(t)$  and  $f_{IFM}(t)$  such that

$$\int_0^{T_d} |f_{RAD}(t)|^2 dt = \int_0^{T_d} |f_{IFM}(t)|^2 dt = 1. \quad (2.21)$$

The complex envelopes can then be expressed as

$$s_{RAD}(t) = \sqrt{E_{RAD}} f_{RAD}(t) \quad (2.22)$$

and

$$s_{IFM}(t) = \sqrt{E_{IFM}} f_{IFM}(t). \quad (2.23)$$

For simplicity, assume that the direct path signal between the monostatic and bistatic radars is used as the coherent reference signal for the correlator in the non-cooperative bistatic radar receiver. With reference to Figure 2.2, the direct path consists of the bistatic baseline which is of length,  $L$ . Let  $G_{MR}^{DP}$  denote the antenna gain of the monostatic radar in the direction of the direct path. Consequently, the power density of the monostatic radar signal at the bistatic radar is

$$W_{RAD}^{DP} = \frac{(E_{RAD}/T_d)G_{MR}^{DP}}{4\pi L^2}. \quad (2.24)$$

Let  $G_{BR}^{DP}$  denote the antenna gain of the bistatic radar in the direction of the direct path. Then the effective aperture area of the bistatic radar antenna in the direction of the direct path is

$$A_{BR}^{DP} = \frac{G_{BR}^{DP} \lambda^2}{4\pi} \quad (2.25)$$

where  $\lambda$  is the signal wavelength. It follows that the monostatic radar signal power intercepted by the bistatic radar is

$$P_{RAD}^{DP} = W_{RAD}^{DP} A_{BR}^{DP} = \frac{E_{RAD} G_{MR}^{DP} G_{BR}^{DP} \lambda^2}{(4\pi)^2 L^2 T_d}. \quad (2.26)$$

Similarly, let  $G_{IFM}^{DP}$  denote the antenna gain of the interferometer in the direction of the direct path. The interferometer signal power intercepted by the bistatic radar is then given by

$$P_{IFM}^{DP} = \frac{E_{IFM} G_{IFM}^{DP} G_{BR}^{DP} \lambda^2}{(4\pi)^2 L^2 T_d}. \quad (2.27)$$

Assume the direct path signal intercepted by the bistatic radar receiver is delayed by an amount,  $\tau^{DP}$ , and Doppler shifted by an amount,  $f^{DP}$ . If  $n^{DP}(t)$  denotes the complex envelope of the receiver noise in the direct path, the complex envelope of the direct path signal may be modeled as

$$s^{DP}(t) = k_{RAD}^{DP} f_{RAD}(t - \tau^{DP}) e^{j2\pi f^{DP}(t - \tau^{DP})} + k_{IFM}^{DP} f_{IFM}(t - \tau^{DP}) e^{j2\pi f^{DP}(t - \tau^{DP})} + n^{DP}(t) \quad (2.28)$$

where  $k_{RAD}^{DP}$  and  $k_{IFM}^{DP}$  are complex constants such that

$$|k_{RAD}^{DP}|^2 = P_{RAD}^{DP} T_d = \frac{E_{RAD} G_{MR}^{DP} G_{BR}^{DP} \lambda^2}{(4\pi)^2 L^2} \quad (2.29)$$

and

$$|k_{IFM}^{DP}|^2 = P_{IFM}^{DP} T_d = \frac{E_{IFM} G_{IFM}^{DP} G_{BR}^{DP} \lambda^2}{(4\pi)^2 L^2}. \quad (2.30)$$

With reference to Figure 2.2, the signal reflected from the target to the non-cooperative bistatic radar receiver travels from the transmitter along the two legs of the triangle whose lengths are  $R_T$  and  $R_R$ . In general, this signal consists of two components, one from the monostatic radar and one from the interferometer. The two legs of the triangle are referred to in this report as the total path. Let  $G_{MR}^{TP}$ ,  $G_{IFM}^{TP}$ ,  $G_{BR}^{TP}$  denote the antenna gains of the monostatic radar, interferometer, and bistatic radar, respectively, in the target direction along the total path. Also, let  $\sigma_T$  be the effective target radar cross section. Since the power density of the monostatic radar signal at the target is

$$W_T^{TP} = \frac{(E_{RAD} / T_d) G_{MR}^{TP}}{4\pi R_T^2}, \quad (2.31)$$

the power density of the monostatic radar signal at the bistatic radar is

$$W_{RAD}^{TP} = \frac{(E_{RAD} / T_d) G_{MR}^{TP}}{4\pi R_T^2} \frac{\sigma_T}{4\pi R_R^2}. \quad (2.32)$$

Hence, the target signal power intercepted by the bistatic radar due to the monostatic radar is

$$P_{RAD}^{TP} = \frac{E_{RAD} G_{MR}^{TP} G_{BR}^{TP} \sigma_T \lambda^2}{(4\pi)^3 R_T^2 R_R^2 T_d}. \quad (2.33)$$

Similarly, the target signal power intercepted by the bistatic radar due to the interferometer is

$$P_{IFM}^{TP} = \frac{E_{IFM} G_{IFM}^{TP} G_{BR}^{TP} \sigma_T \lambda^2}{(4\pi)^3 R_T^2 R_R^2 T_d}. \quad (2.34)$$

Assume the total path signal received by the bistatic radar receiver is delayed by an amount,  $\tau^{TP}$ , and Doppler shifted by an amount,  $f^{TP}$ . If  $n^{TP}(t)$  denotes the complex envelope of the receiver noise in the total path, the complex envelope of the total path signal may be modeled as

$$\begin{aligned} s^{TP}(t) = & k_{RAD}^{TP} f_{RAD}(t - \tau^{TP}) e^{j2\pi f^{TP}(t - \tau^{TP})} \\ & + k_{IFM}^{TP} f_{IFM}(t - \tau^{TP}) e^{j2\pi f^{TP}(t - \tau^{TP})} + n^{TP}(t) \end{aligned} \quad (2.35)$$

where  $k_{RAD}^{TP}$  and  $k_{IFM}^{TP}$  are complex constants such that

$$|k_{RAD}^{TP}|^2 = P_{RAD}^{TP} T_d = \frac{E_{RAD} G_{MR}^{TP} G_{BR}^{TP} \sigma_T \lambda^2}{(4\pi)^3 R_T^2 R_R^2} \quad (2.36)$$

and

$$|k_{IFM}^{TP}|^2 = P_{IFM}^{TP} T_d = \frac{E_{IFM} G_{IFM}^{TP} G_{BR}^{TP} \sigma_T \lambda^2}{(4\pi)^3 R_T^2 R_R^2}. \quad (2.37)$$

The bistatic delay is defined in Equation (2.3) as

$$\tau_B = \tau^{TP} - \tau^{DP}.$$

Similarly, the bistatic Doppler shift is defined to be

$$f_B = f^{TP} - f^{DP}. \quad (2.38)$$

Ideally, the non-cooperative bistatic receiver would like to correlate  $f_{RAD}(t - \tau^{TP}) e^{j2\pi f^{TP}(t - \tau^{TP})}$  with the total path signal,  $s^{TP}(t)$ . To accomplish this, it would modify the direct path signal by a delay,  $\tau_B$ , and a Doppler shift,  $f_B$ . However, in practice,  $\tau_B$  and  $f_B$  are unknown. Hence, the bistatic radar receiver would utilize estimates of  $\tau_B$  and  $f_B$ . Let these be denoted by

$$\hat{\tau}_B = \tau_B - \tau \quad (2.39)$$

and

$$\hat{f}_B = f_B - \nu. \quad (2.40)$$

To detect a possible target, the bistatic radar receiver would then correlate  $s^{DP}(t - \hat{\tau}_B) e^{j2\pi \hat{f}_B(t - \tau^{DP} - \hat{\tau}_B)}$  with  $s^{TP}(t)$ . This yields the test statistic employed for the detection of a target.

By definition, correlation of the complex waveforms  $f_1(t)$  and  $f_2(t)$  is given by

$$y = \int_{-\infty}^{\infty} f_1^*(t) f_2(t) dt \quad (2.41)$$

where the asterisk denotes the operation of complex conjugation. Hence, the test statistic at the output of the correlator in the non-cooperative bistatic radar receiver is

$$l = \int_{-\infty}^{\infty} [s^{DP}(t - \hat{\tau}_B)]^* e^{-j2\pi \hat{f}_B(t - \tau^{DP} - \hat{\tau}_B)} s^{TP}(t) dt. \quad (2.42)$$

Substituting the expressions for  $s^{DP}(t)$  and  $s^{TP}(t)$  given by Equations (2.28) and (2.35) into Equation (2.42), the detection statistic becomes

$$\begin{aligned} l = \int_{-\infty}^{\infty} & [ (k_{RAD}^{DP})^* f_{RAD}^*(t - \tau^{DP} - \hat{\tau}_B) e^{-j2\pi f^{DP}(t - \tau^{DP} - \hat{\tau}_B)} \\ & e^{-j2\pi \hat{f}_B(t - \tau^{DP} - \hat{\tau}_B)} + (k_{IFM}^{DP})^* f_{IFM}^*(t - \tau^{DP} - \hat{\tau}_B) \\ & e^{-j2\pi f^{DP}(t - \tau^{DP} - \hat{\tau}_B)} e^{-j2\pi \hat{f}_B(t - \tau^{DP} - \hat{\tau}_B)} \\ & + (n^{DP}(t - \hat{\tau}_B))^* e^{-j2\pi \hat{f}_B(t - \tau^{DP} - \hat{\tau}_B)} ] \\ & [ k_{RAD}^{TP} f_{RAD}(t - \tau^{TP}) e^{j2\pi f^{TP}(t - \tau^{TP})} \\ & + k_{IFM}^{TP} f_{IFM}(t - \tau^{TP}) e^{j2\pi f^{TP}(t - \tau^{TP})} + n^{TP}(t) ] dt. \end{aligned} \quad (2.43)$$

Carrying out the product in the integrand of  $l$ , it is seen that  $l$  is a summation composed of nine integrals. If the  $i^{\text{th}}$  integral is denoted by  $I_i$ , the detection statistic can be expressed as

$$l = \sum_{i=1}^9 I_i \quad (2.44)$$

where only four of the terms do not involve receiver noise. Focusing on these four terms, it is convenient to define the complex constants

$$\begin{aligned} k_1 &= (k_{RAD}^{DP})^* k_{RAD}^{TP} \\ k_2 &= (k_{RAD}^{DP})^* k_{IFM}^{TP} \\ k_3 &= (k_{IFM}^{DP})^* k_{RAD}^{TP} \\ k_4 &= (k_{IFM}^{DP})^* k_{IFM}^{TP}. \end{aligned} \quad (2.45)$$

Referring to Equations (2.3) and (2.39), note that

$$t - \tau^{DP} - \hat{\tau}_B = t - \tau^{TP} + \tau. \quad (2.46)$$

Also, with reference to Equations (2.38) and (2.40),

$$f^{DP} + \hat{f}_B = f^{TP} - v. \quad (2.47)$$

Making the change of variable,

$$\sigma = t - \tau^{TP} + \tau, \quad (2.48)$$

it can be shown that

$$I_1 = k_1 e^{-j2\pi f^{TP} \tau} \int_{-\infty}^{\infty} f_{RAD}^*(\sigma) f_{RAD}(\sigma - \tau) e^{j2\pi v \sigma} d\sigma. \quad (2.49)$$

By definition, the delay – Doppler ambiguity function of the host radar waveform is

$$\begin{aligned} \chi(\tau, v) &= \frac{1}{E_{RAD}} \int_{-\infty}^{\infty} s_{RAD}^*(\sigma) s_{RAD}(\sigma - \tau) e^{j2\pi v \sigma} d\sigma \\ &= \int_{-\infty}^{\infty} f_{RAD}^*(\sigma) f_{RAD}(\sigma - \tau) e^{j2\pi v \sigma} d\sigma \end{aligned} \quad (2.50)$$

where use was made of Equations (2.22) and (2.23). As a result,  $I_1$  may be expressed as

$$I_1 = k_1 e^{-j2\pi f^{TP} \tau} \chi(\tau, v). \quad (2.51)$$

In a similar manner, it can be shown that  $I_2$  and  $I_3$  are given by

$$I_2 = k_2 e^{-j2\pi f^{TP} \tau} \int_{-\infty}^{\infty} f_{RAD}^*(\sigma) f_{IFM}(\sigma - \tau) e^{j2\pi v \sigma} d\sigma \quad (2.52)$$

and

$$I_3 = k_3 e^{-j2\pi f^{TP} \tau} \int_{-\infty}^{\infty} f_{IFM}^*(\sigma) f_{RAD}(\sigma - \tau) e^{j2\pi v \sigma} d\sigma. \quad (2.53)$$

By definition, the delay – Doppler cross ambiguity function between the interferometer and host radar waveform is

$$\begin{aligned} Z(\tau, v) &= \frac{1}{\sqrt{E_{IFM} E_{RAD}}} \int_{-\infty}^{\infty} s_{IFM}^*(\sigma) s_{RAD}(\sigma - \tau) e^{j2\pi v \sigma} d\sigma \\ &= \int_{-\infty}^{\infty} f_{IFM}^*(\sigma) f_{RAD}(\sigma - \tau) e^{j2\pi v \sigma} d\sigma. \end{aligned} \quad (2.54)$$

Note that

$$Z(-\tau, -v) = \int_{-\infty}^{\infty} f_{IFM}^*(\sigma) f_{RAD}(\sigma + \tau) e^{-j2\pi v \sigma} d\sigma \quad (2.55)$$

and

$$Z^*(-\tau, -v) = \int_{-\infty}^{\infty} f_{IFM}(\sigma) f_{RAD}^*(\sigma + \tau) e^{j2\pi v \sigma} d\sigma. \quad (2.56)$$

With the change of variable,  $\alpha = \sigma + \tau$ ,  $Z^*(-\tau, -v)$  becomes

$$\begin{aligned} Z^*(-\tau, -v) &= \int_{-\infty}^{\infty} f_{RAD}^*(\alpha) f_{IFM}(\alpha - \tau) e^{j2\pi v(\alpha - \tau)} d\alpha \\ &= e^{-j2\pi v\tau} \int_{-\infty}^{\infty} f_{RAD}^*(\alpha) f_{IFM}(\alpha - \tau) e^{j2\pi v\alpha} d\alpha. \end{aligned} \quad (2.57)$$

It follows that  $I_2$  and  $I_3$  can be expressed as

$$I_2 = k_2 e^{-j2\pi(f^{TP} - v)\tau} Z^*(-\tau, -v) \quad (2.58)$$

and

$$I_3 = k_3 e^{-j2\pi f^{TP}\tau} Z(\tau, v). \quad (2.59)$$

Finally, it can be shown that

$$I_4 = k_4 e^{-j2\pi f^{TP}\tau} \int_{-\infty}^{\infty} f_{IFM}^*(\sigma) f_{IFM}(\sigma - \tau) e^{j2\pi v\sigma} d\sigma. \quad (2.60)$$

By definition, the delay - Doppler ambiguity function of the interferometer waveform is

$$\begin{aligned} \Gamma(t, v) &= \frac{1}{E_{IFM}} \int_{-\infty}^{\infty} s_{IFM}^*(\sigma) s_{IFM}(\sigma - \tau) e^{j2\pi v\sigma} d\sigma \\ &= \int_{-\infty}^{\infty} f_{IFM}^*(\sigma) f_{IFM}(\sigma - \tau) e^{j2\pi v\sigma} d\sigma. \end{aligned} \quad (2.61)$$

Consequently,

$$I_4 = k_4 e^{-j2\pi f^{TP}\tau} \Gamma(\tau, v). \quad (2.62)$$

In summary, the detection statistic used by the non-cooperative bistatic radar receiver is

$$\begin{aligned} l &= e^{-j2\pi f^{TP}\tau} [k_1 \chi(\tau, v) + k_2 e^{j2\pi v\tau} Z^*(-\tau, -v) \\ &\quad + k_3 Z(\tau, v) + k_4 \Gamma(\tau, v)] + [\text{terms that involve receiver noise}]. \end{aligned} \quad (2.63)$$

The desired signal component of the detection statistic is

$$l_s = k_1 e^{-j2\pi f^{TP}\tau} \chi(\tau, v). \quad (2.64)$$

The remaining terms represent noise and interference. In general, the desired signal component is corrupted by thermal noise, clutter, multipath and/or other propagation effects. However, it is the intention of this effort to design the interferometer signal such that it effectively masks the direct path signal from the host radar. The expression for the detection statistic in Equation (2.63) clearly shows that the objective of coherent reference denial depends upon the delay-Doppler ambiguity functions of the host radar and interferometer waveforms and their cross ambiguity function.

## CHAPTER 3

### INTERFEROMETER AND HOST RADAR ANTENNA PATTERNS

#### 3.1 Interferometer Antenna Pattern

In addition to coherent reference denial, the interferometer signal is to be used for communications in many different directions. Because the interferometer will serve as a transmitter, its antenna pattern is derived in this section in the context of a radiation pattern. However, the radiation and reception patterns of an antenna are known to be identical.

Consider a point,  $P_o$ , in the far field of the interferometer, as shown in Figure 3.1. The cartesian coordinates of  $P_o$  are given by  $(x_o, y_o, z_o)$  while its spherical coordinates are  $(r_o, \theta_o, \phi_o)$ . These are related by

$$\begin{aligned} x_o &= r_o \sin \theta_o \cos \phi_o \\ y_o &= r_o \sin \theta_o \sin \phi_o \\ z_o &= r_o \cos \theta_o \end{aligned} \quad (3.1)$$

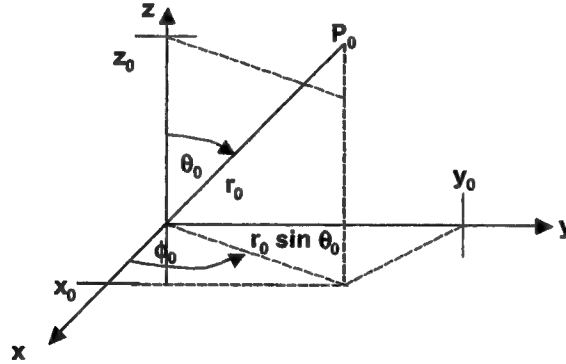


Figure 3.1: Both Cartesian and spherical coordinates are used to characterize a point in the far field of the interferometer.

Assume each antenna in the interferometer pair consists of a dipole antenna of length,  $l$ , as shown in Figure 3.2. Note that each leg is of length,  $l/2$ . Let  $P$  denote an arbitrary point in the far field of the antenna with spherical coordinates  $(r, \theta, \phi)$ . Assuming a sinusoidal excitation at frequency,  $\omega_o$ , and using a far field approximation [4], the electric field at  $P$  is approximately given by the real part of

$$E = \frac{K}{r} F(\theta) e^{-j\beta_o r} e^{j\omega_o t} \quad (3.2)$$

where  $K$  is a constant,

$$\beta_o = \frac{\omega_o}{c} = \frac{2\pi f_o}{c} = \frac{2\pi}{\lambda_o}, \quad (3.3)$$

$\lambda_o$  is the signal wavelength, and



$$F(\theta) = \frac{\cos\left[\frac{\beta_0 l}{2} \cos \theta\right] - \cos\left[\frac{\beta_0 l}{2}\right]}{\sin \theta} = \frac{\cos\left[\frac{\pi l}{\lambda_0} \cos \theta\right] - \cos\left[\frac{\pi l}{\lambda_0}\right]}{\sin \theta}. \quad (3.4)$$

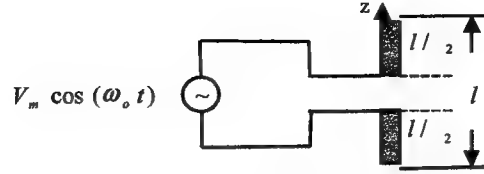


Figure 3.2: Each antenna in the interferometer pair consists of a dipole antenna of length,  $l$ .

Consistent with the circular symmetry of the dipole, the field is seen to be independent of  $\phi$ . The most frequently encountered case is the half-wave dipole for which the total length of the dipole antenna is  $l = \lambda_0 / 2$ . Then

$$F(\theta) = \frac{\cos\left[\frac{\pi}{2} \cos \theta\right]}{\sin \theta}. \quad (3.5)$$

Let the two dipole antennas of the interferometer pair be directed in the  $z$ -direction and placed on the  $x$ -axis at  $x = -d_{IFM} / 2$  and  $x = +d_{IFM} / 2$ , respectively, as shown in Figure 3.3. Thus,  $d_{IFM}$  is the spacing between the interferometer elements. Consider a point, P, in the near field, as illustrated in Figure 3.4. The lengths of lines OP, BP, and AP are denoted by  $r$ ,  $r_1$ , and  $r_2$ , respectively. The angles from the  $z$ -direction to lines OP, BP, and AP are given by  $\theta$ ,  $\theta_1$ , and  $\theta_2$ , respectively. Finally  $\gamma$ ,  $\gamma_1$ , and  $\gamma_2$ , respectfully, denote the angles between the  $x$ -axis and the lines OP, BP, and AP. As point, P, moves into the far field of the antennas, the following approximations become valid:

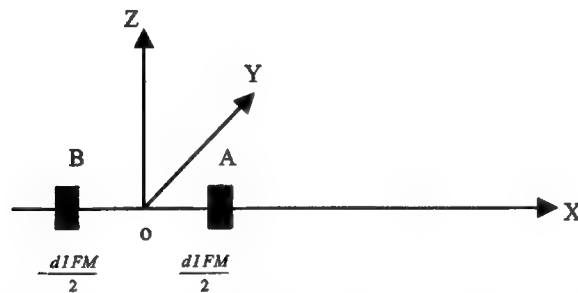


Figure 3.3: The dipole antennas are placed along the  $x$ -axis at A and B and are directed in the  $z$ -direction.

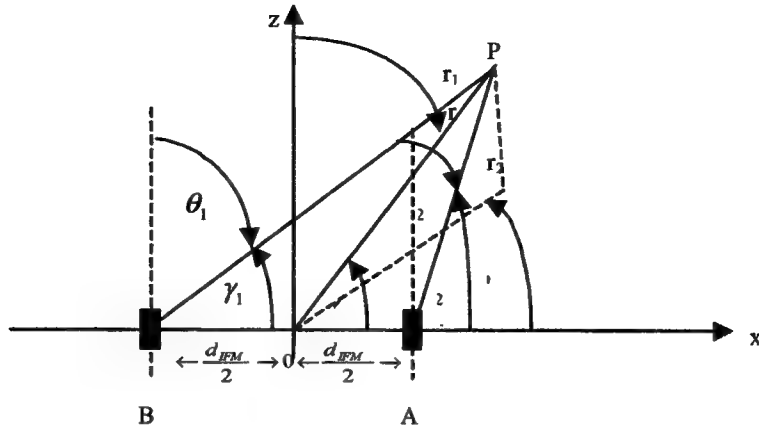


Figure 3.4: When P is in the near field of the interferometer, the geometry is relatively complicated.

$$\begin{aligned}
 r_1 &\approx r_2 \approx r \\
 \theta_1 &\approx \theta_2 \approx \theta \\
 \gamma_1 &\approx \gamma_2 \approx \gamma.
 \end{aligned} \tag{3.6}$$

The far-field geometry is shown in Figure 3.5.

Assuming both antenna elements of the interferometer pair are excited by the same sinusoidal signal at frequency,  $\omega_o$ , the total electric field at point P when P is in the near field is given by the real part of

$$E_{IFM}^{TOT} = \left[ \frac{K}{r_1} F(\theta_1) e^{-j\beta_o r_1} + \frac{K}{r_2} F(\theta_2) e^{-j\beta_o r_2} \right] e^{j\omega_o t}. \tag{3.7}$$

As P moves into the far field of the interferometer,

$$\frac{1}{r_1} \approx \frac{1}{r_2} \approx \frac{1}{r} \tag{3.8}$$

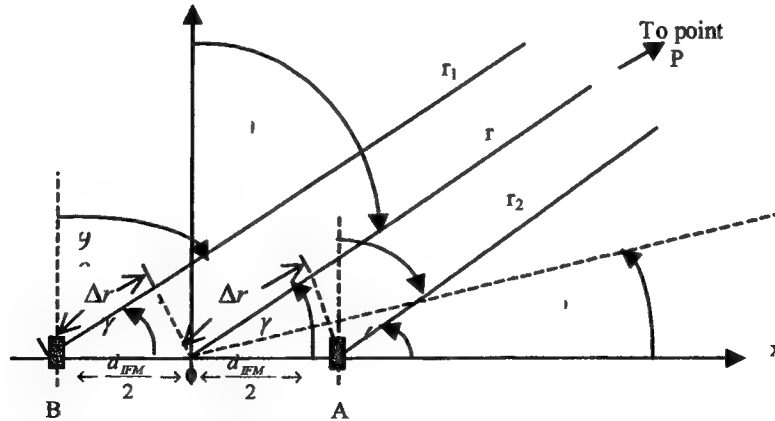


Figure 3.5: The geometry simplifies as P moves to the far field

and

$$F(\theta_1) \approx F(\theta_2) \approx F(\theta). \quad (3.9)$$

However, the phase angles,

$$\beta_o r_1 = 2\pi \left( \frac{r_1}{\lambda_o} \right) \quad (3.10)$$

and

$$\beta_o r_2 = 2\pi \left( \frac{r_2}{\lambda_o} \right), \quad (3.11)$$

are very sensitive to small changes in  $r_1$  and  $r_2$  on the order of a wavelength because of their dependence on the electrical distances  $r_1 / \lambda_o$  and  $r_2 / \lambda_o$ . From Figure 3.5,

$$\begin{aligned} r_1 &\approx r + \Delta r \\ r_2 &\approx r - \Delta r. \end{aligned} \quad (3.12)$$

Using Equations (3.8), (3.9), and (3.12) in Equation (3.7), the total electric field at point, P, becomes

$$\begin{aligned} E_{IFM}^{TOT} &\approx \frac{K}{r} F(\theta) e^{-j\beta_o r} \left[ e^{-j\beta_o (\Delta r)} + e^{j\beta_o (\Delta r)} \right] e^{j\omega_o t} \\ &= \frac{2K}{r} F(\theta) \cos [\beta_o (\Delta r)] e^{-j\beta_o r} e^{j\omega_o t}. \end{aligned} \quad (3.13)$$

From Figure 3.5,

$$\Delta r = \frac{d_{IFM}}{2} \cos \gamma \quad (3.14)$$

where  $\gamma$  is the angle between  $\vec{a}_r$ , the unit vector in the r-direction of spherical coordinates, and  $\vec{a}_x$ , the unit vector in the x-direction of Cartesian coordinates. Hence,

$$\cos \gamma = \vec{a}_r \cdot \vec{a}_x \quad (3.15)$$

where the dot indicates a dot product between the two vectors. Thus,  $\cos \gamma$  is the projection of  $\vec{a}_r$  on  $\vec{a}_x$ . From Equation (3.1), it follows that

$$\cos \gamma = \sin \theta \cos \phi. \quad (3.16)$$

Therefore, utilizing Equations (3.14) and (3.16) in Equation (3.13), the total electric field at point, P, is expressed as

$$E_{IFM}^{TOT} \approx \frac{2K}{r} F(\theta) \cos \left[ \frac{\beta_o}{2} d_{IFM} \sin \theta \cos \phi \right] e^{-j\beta_o r} e^{j\omega_o t}$$

$$= \frac{2K}{r} F(\theta) \cos \left[ \pi \left( \frac{d_{IFM}}{\lambda_o} \right) \sin \theta \cos \phi \right] e^{-j\beta_o r} e^{j\omega_o t} \quad (3.17)$$

The interferometer array factor is defined to be

$$F_{IFM}(\theta, \phi) = \cos \left[ \pi \left( \frac{d_{IFM}}{\lambda_o} \right) \sin \theta \cos \phi \right] \quad (3.18)$$

Hence,

$$E_{IFM}^{TOT} \approx \frac{2K}{r} F(\theta) F_{IFM}(\theta, \phi) e^{-j\beta_o r} e^{j\omega_o t} \quad (3.19)$$

Observe that the resultant field involves the product of the pattern of the individual (identical) antenna elements and the array factor which is a function of the electrical distance,  $d_{IFM} / \lambda_o$ . This is referred to as the principle of pattern multiplication. If antennas other than dipoles are used for the array elements,  $E_{IFM}^{TOT}$  is obtained by merely substituting the appropriate  $F(\theta)$  for the antenna elements.

The above analysis makes use of traditional spherical coordinates in which the azimuth angle,  $\phi$ , is measured from the x-axis. However, in the conventional array literature, the azimuth angle,  $\alpha$ , is measured from the perpendicular to a linear array. When the linear array is placed along the x-axis,  $\alpha$  is measured from the y-axis, as illustrated in Figure 3.6. Note that

$$\cos \phi = \sin \alpha \quad (3.20)$$

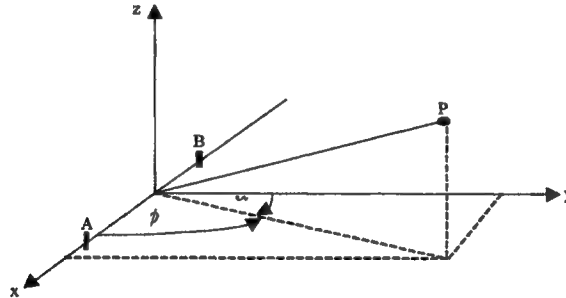


Figure 3.6: When a linear array is placed on the x-axis, the azimuth angle,  $\alpha$ , in the array literature is typically measured from the y-axis.

In terms of  $\alpha$ , the total electric field at point, P is

$$E_{IFM}^{TOT} \approx \frac{2K}{r} F(\theta) F_{IFM}(\theta, \alpha) e^{-j\beta_o r} e^{j\omega_o t} \quad (3.21)$$

where

$$F_{IFM}(\theta, \alpha) = \cos \left[ \pi \left( \frac{d_{IFM}}{\lambda_o} \right) \sin \theta \sin \alpha \right]. \quad (3.22)$$

Radiation patterns are conventionally plotted in decibels where the pattern is normalized such that the maximum value is 0dB. The radiation pattern of the dipole antenna used for the interferometer elements is considered first. In decibels, this is defined to be

$$G(\theta) = 10 \log_{10} \left\{ \left| \frac{F(\theta)}{F(\theta)_{\max}} \right|^2 \right\} \quad (3.23)$$

where  $F(\theta)_{\max}$  denotes the maximum value of  $F(\theta)$  and  $F(\theta)$  is given by Equation (3.4). Detailed plots of  $G(\theta)$  are presented in Figures 3.7, 3.8, and 3.9 for various antenna lengths [5].

The polar plots in Figure 3.7 pertain to situations where  $l \leq \lambda_o$ . It is seen from Figure 3.7 that the radiation pattern for this case includes only one major lobe symmetrically placed around the antenna axis. Note that the beam widths of the main lobes decrease with an increase in the antenna length. Thus, the longer the antenna is, the more directive is the radiated energy.

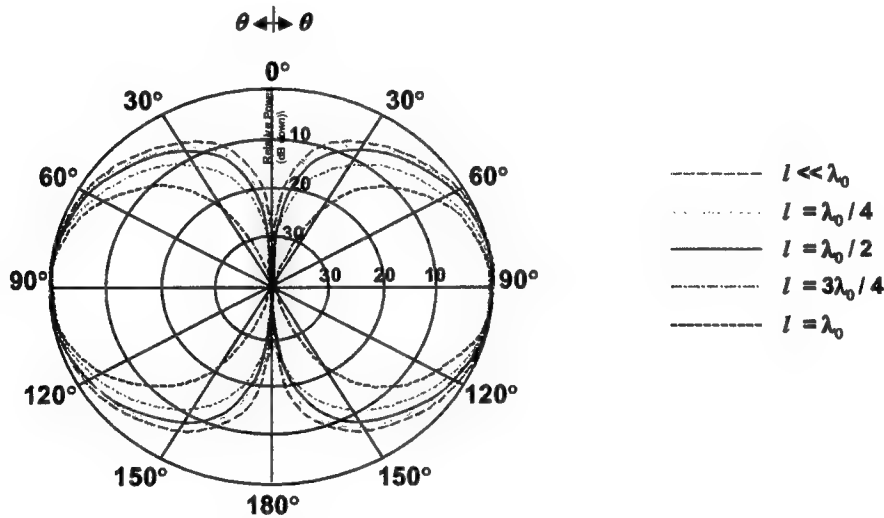
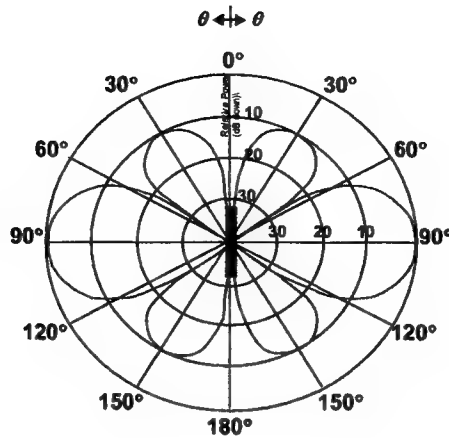


Figure 3.7: Radiation patterns are plotted for the dipole antenna with  $l \leq \lambda_o$ .



**Figure 3.8:** The dipole antenna radiation pattern is plotted for  $l = 1.25\lambda_0$ .

Figure 3.8 shows the dipole element radiation pattern for  $l = 1.25\lambda_0$ . Observe that there are now three major lobes symmetrically placed around the antenna axis. The lobe with maximum gain is centered at  $\theta = 90^\circ$ . The dipole element radiation pattern for  $l = 1.5\lambda_0$  is presented in Figure 3.9. As in Figure 3.8, there are three major lobes symmetrically placed around the antenna axis. However, now there are two lobes of equal maximum intensity located at  $\theta = 40^\circ$  and  $\theta = 140^\circ$ . With a still further increase in the electrical length of the antenna, a larger number of lobes begin to appear in the element radiation pattern. The radiation pattern of the dipole antenna is seen to lose its directional properties for antenna lengths larger than  $\lambda_0$ .

The radiation pattern of the interferometer array factor, given in Equation (3.22), is considered next. As indicated in Figure 1.2, it is first assumed that the interferometer elements are placed on a linear grid about the main radar elements. The configuration is illustrated in Figure 3.10 where the spacing between antenna elements is denoted by  $d$ . Independent of whether the  $N$ -element main radar antenna array contains an odd or even number of elements, note that the spacing between the interferometer element pair is

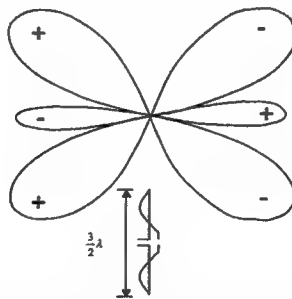


**Figure 3.9:** The dipole antenna radiation pattern is shown for  $l = 1.5\lambda_0$ .

$$d_{IFM} = \left( \frac{N+1}{2} \right) d - \left[ - \left( \frac{N+1}{2} \right) d \right] = (N+1)d. \quad (3.24)$$

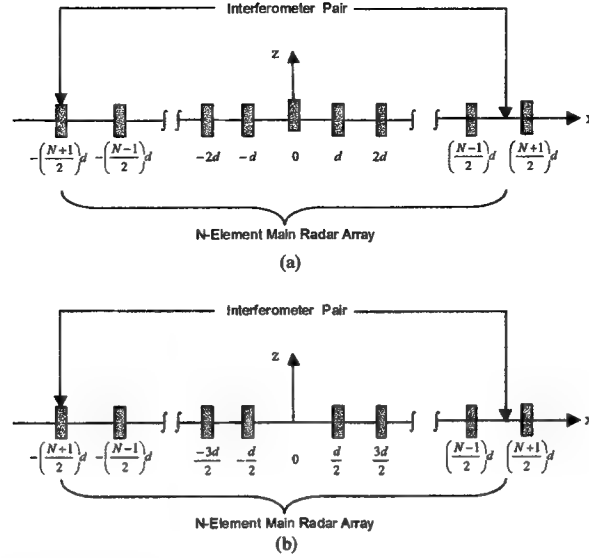


**Figure 3.10:** The antenna configuration consists of a linear grid with equal spacing,  $d$ . The main radar array is composed of  $N$  elements where  $N$  can be either an (a) odd or (b) even integer.

Substitution of Equation (3.24) into Equation (3.22) yields

$$F_{IFM}(\theta, \alpha) = \cos \left[ (N+1)\pi \left( \frac{d}{\lambda_o} \right) \sin \theta \sin \alpha \right]. \quad (3.25)$$

Polar plots of  $|F_{IFM}(\theta, \alpha)|$  are commonly used to gain insight into the radiation pattern of the interferometer array factor. Observe that values of  $F_{IFM}(\theta, \alpha)$  range between  $-1$  and  $+1$ . Hence, the maximum value of  $|F_{IFM}(\theta, \alpha)|$  is unity and occurs when

$$(N+1)\pi \left( \frac{d}{\lambda_o} \right) \sin \theta \sin \alpha = m\pi \quad (3.26)$$

where

$$m = 0, \pm 1, \pm 2, \dots$$

The minimum value of  $|F_{IFM}(\theta, \alpha)|$  is zero and occurs when

$$(N+1)\pi \left( \frac{d}{\lambda_o} \right) \sin \theta \sin \alpha = n \frac{\pi}{2} \quad (3.27)$$

where

$$n = \pm 1, \pm 3, \pm 5, \dots \quad (3.28)$$

The maxima and zeros of  $|F_{IFM}(\theta, \alpha)|$  are seen to be a function of both  $\theta$  and  $\alpha$ . To visualize the azimuthal radiation pattern of the array factor, it is convenient to hold  $\theta$  fixed and vary  $\alpha$ . Alternatively, to visualize the elevation radiation pattern, it is convenient to hold  $\alpha$  fixed and vary  $\theta$ .

The azimuthal radiation pattern is considered first. For this purpose, let  $\theta$  equal the fixed angle,  $\theta_o$ . The maxima are now governed by

$$(N+1)\pi \left( \frac{d}{\lambda_o} \right) \sin \theta_o \sin \alpha = m\pi \quad (3.29)$$

where

$$m = 0, \pm 1, \pm 2, \dots \quad (3.30)$$

Note that

$$\sin \alpha = \frac{m}{(N+1)} \left( \frac{\lambda_o}{d} \right) \frac{1}{\sin \theta_o}. \quad (3.31)$$

Since

$$|\sin \alpha| \leq 1, \quad (3.32)$$

it follows that

$$|m| \leq (N+1) \left( \frac{d}{\lambda_o} \right) |\sin \theta_o|. \quad (3.33)$$

Similarly, with  $\theta = \theta_o$ , the zeros of the array factor occur for

$$(N+1)\pi \left( \frac{d}{\lambda_o} \right) \sin \theta_o \sin \alpha = n \frac{\pi}{2} \quad (3.34)$$

where

$$n = \pm 1, \pm 3, \pm 5, \dots \quad (3.35)$$

Now

$$\sin \alpha = \frac{n}{2(N+1)} \left( \frac{\lambda_o}{d} \right) \frac{1}{\sin \theta_o}. \quad (3.36)$$

Because  $|\sin \alpha|$  cannot exceed unity, it is concluded that

$$|n| \leq 2(N+1) \left( \frac{d}{\lambda_o} \right) |\sin \theta_o|. \quad (3.37)$$

Thus far, the discussion has focused on the values of  $\alpha$  for which  $F_{IFM}(\theta_o, \alpha)$  attains either its maximum or minimum values. The question arises as to whether or not the azimuthal radiation pattern contains minor lobes in



addition to the major lobes. To answer this question, the derivative of  $F_{IFM}(\theta_o, \alpha)$  with respect to  $\alpha$  is considered. With reference to Equation (3.25),

$$\frac{dF_{IFM}(\theta_o, \alpha)}{d\alpha} = -(N+1)\pi \left( \frac{d}{\lambda_o} \right) \sin \theta_o \sin \left[ (N+1)\pi \left( \frac{d}{\lambda_o} \right) \sin \theta_o \sin \alpha \right] \cos \alpha. \quad (3.38)$$

The derivative equals zero when either

$$\sin \left[ (N+1)\pi \left( \frac{d}{\lambda_o} \right) \sin \theta_o \sin \alpha \right] = 0 \quad (3.39)$$

or

$$\cos \alpha = 0. \quad (3.40)$$

Note that Equation (3.39) is satisfied for

$$(N+1)\pi \left( \frac{d}{\lambda_o} \right) \sin \theta_o \sin \alpha = m\pi \quad (3.41)$$

where

$$m = 0, \pm 1, \pm 2, \dots \quad (3.42)$$

This result is identical to that of Equations (3.29) and (3.30) and yields the major lobes of the azimuthal radiation pattern for which

$$F_{IFM}(\theta_o, \alpha) = \pm 1. \quad (3.43)$$

Equation (3.40) is satisfied for

$$\alpha = \pm \frac{\pi}{2}. \quad (3.44)$$

However, it should be remembered that the derivative equal to zero at a point only guarantees that the slope of the function is zero at that point. Consequently, either a major lobe, minor lobe, or inflection point is possible at

$$\alpha = \pm \frac{\pi}{2}.$$

Polar plots for the azimuthal radiation pattern of the interferometer array factor are presented in Figure 3.11, where  $N$  is allowed to range from  $N=2$  to  $N=7$ , and

$$d = \frac{\lambda_o}{2}, \theta_o = \frac{\pi}{2}. \quad (3.45)$$

For this special case,

$$d_{IFM} = (N+1) \frac{\lambda_o}{2} \quad (3.46)$$

and

$$\left| F_{IFM} \left( \frac{\pi}{2}, \alpha \right) \right| = \left| \cos \left[ (N+1) \frac{\pi}{2} \sin \alpha \right] \right|. \quad (3.47)$$

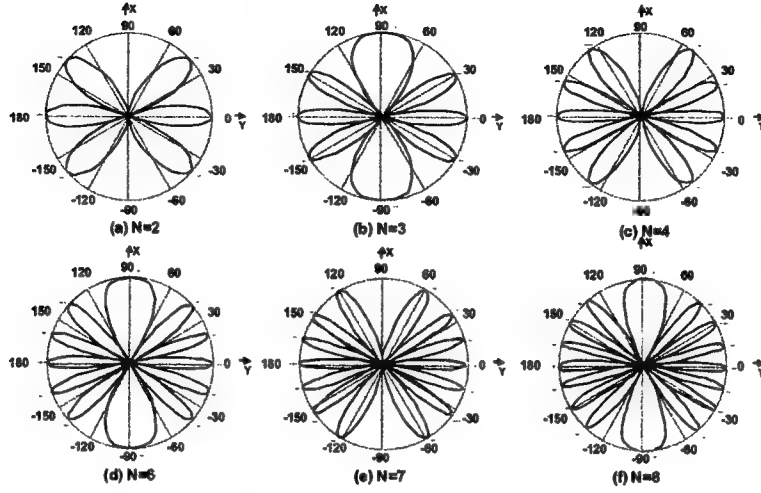


Figure 3.11: The azimuthal radiation pattern of the interferometer array factor is plotted for  $d = \lambda_o / 2$ ,  $\theta_o = \pi / 2$ , and  $d_{IFM}$  equal to (a)  $3\lambda_o / 2$ , (b)  $2\lambda_o$ , (c)  $5\lambda_o / 2$ , (d)  $3\lambda_o$ , (e)  $7\lambda_o / 2$ , and (f)  $4\lambda_o$ .

Because  $\theta_o = \frac{\pi}{2}$ , the plots in Figure 3.11 show the horizontal radiation pattern in the x-y plane at  $z=0$ . With reference to Equation (3.31) and (3.33), the maxima occur for

$$\sin \alpha = \frac{2m}{(N+1)} \quad (3.48)$$

where

$$m = 0, \pm 1, \pm 2, \dots, \pm \text{floor} \left( \frac{N+1}{2} \right) \quad (3.49)$$

and  $\text{floor}(\bullet)$  denotes the largest integer less than or equal to its argument. Similarly, from Equations (3.36) and (3.37), zeros appear when

$$\sin \alpha = \frac{n}{(N+1)} \quad (3.50)$$

where

$$n = \pm 1, \pm 3, \dots, \pm \text{ofloor}(N+1) \quad (3.51)$$

and  $\text{ofloor}(\bullet)$  denotes the largest odd integer less than or equal to its argument. Because

$$F_{IFM} \left( \frac{\pi}{2}, \alpha \right) = \cos \left[ (N+1) \frac{\pi}{2} \sin \alpha \right], \quad (3.52)$$

the radiation pattern assumes either positive or negative real values. In Figure 3.11 the lobes corresponding to positive values of the cosine function are denoted by "+" while those corresponding to negative values of the cosine function are denoted by "-".

In general, the azimuthal radiation pattern of the interferometer array factor can be shown to have the following properties when the conditions of Equation (3.45) hold:

1. For all integer values of  $N$ , either odd or even,
  - a. symmetry exists about both the x- and y- axes,
  - b. the number of major lobes equals  $(2N+2)$ ,
  - c. there are no minor lobes,
  - d. major lobes always occur at  $\alpha = 0^\circ$  and  $180^\circ$
2. When  $N$  is an odd integer,
  - a. the polarity of the major lobes strictly alternate in sign from one lobe to the next,
  - b. major lobes always occur at  $\alpha = \pm 90^\circ$ .
3. When  $N$  is an even integer,
  - a. focusing entirely above or below the x-axis, the polarity of the major lobes strictly alternate in sign from one lobe to the next,
  - b. the first major lobes positioned on either side of the x-axis have the same polarity,
  - c. nulls always occur at  $\alpha = \pm 90^\circ$ .

These properties are clearly demonstrated by the plots in Figure 3.11.

The nulls appearing at  $\alpha = \pm 90^\circ$  when  $N$  is an even integer are of particular interest. As pointed out by the discussion leading up to Equation (3.44), the derivative of the array factor is zero for  $\alpha = \pm 90^\circ$ . Therefore, the nulls at these angles have zero slope. This is consistent with the property that the first major lobes positioned on either side of the x-axis have the same polarity. This is illustrated in Figure 3.12 where a cartesian plot of  $F_{IFM}(\pi/2, \alpha)$ , corresponding to  $N=2$ , is presented with  $\alpha$  varying from  $0^\circ$  to  $180^\circ$ . Observe that the null at  $\alpha = 90^\circ$ , where the polarity of  $F_{IFM}(\pi/2, \alpha)$  is unchanged and the slope is zero, is noticeably broader than the nulls at  $\alpha = 19.5^\circ$  and  $160.5^\circ$ , where the polarity of  $F_{IFM}(\pi/2, \alpha)$  does change. To avoid self-jamming of the radar and communications waveforms, it may be desirable to steer the interferometer pattern such that the main beam of the host radar is centered in this broad null. Steering of the interferometer and placement of the broad null is investigated in Section 3.3.

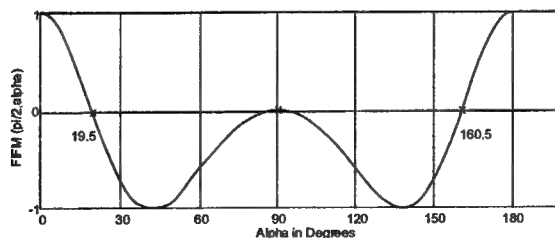


Figure 3.12: The Cartesian plot of  $F_{IFM}(\pi/2, \alpha)$ , corresponding to  $N=2$ , illustrates the broad null that appears at  $\alpha = 90^\circ$ .

Additional insight into the radiation pattern of the interferometer array factor is gained by considering the case for which

$$d = \frac{\lambda_o}{2}, \theta_o = \frac{\pi}{6}. \quad (3.53)$$

Now

$$\left| F_{IFM} \left( \frac{\pi}{6}, \alpha \right) \right| = \left| \cos \left[ (N+1) \frac{\pi}{4} \sin \alpha \right] \right|. \quad (3.54)$$

Polar plots for this case are presented in Figure 3.13 where, as with Figure 3.11, the number of antenna elements in the main radar are allowed to vary from  $N=2$  to  $N=7$ . Because  $\theta_o = \pi/6$ , the plots of Figure 3.13 illustrate the radiation pattern as seen looking into a cone emerging from the origin whose axis is oriented in the  $z$ -direction and whose sides are at an angle of  $30^\circ$  from the  $z$ -axis.

At a specified angle,  $\alpha_o$ , the vertical pattern,  $|F_{IFM}(\theta, \alpha_o)|$  is helpful in understanding the lobing structure of the azimuthal pattern,  $|F_{IFM}(\theta_o, \alpha)|$ . For example, consider  $\alpha_o = \pm 90^\circ$ . As before, let  $d = \lambda_o/2$ . From Equation (3.24), the vertical radiation pattern is given by

$$\left| F_{IFM} \left( \theta, \pm \frac{\pi}{2} \right) \right| = \left| \cos \left[ (N+1) \frac{\pi}{2} \sin \theta \right] \right|. \quad (3.55)$$

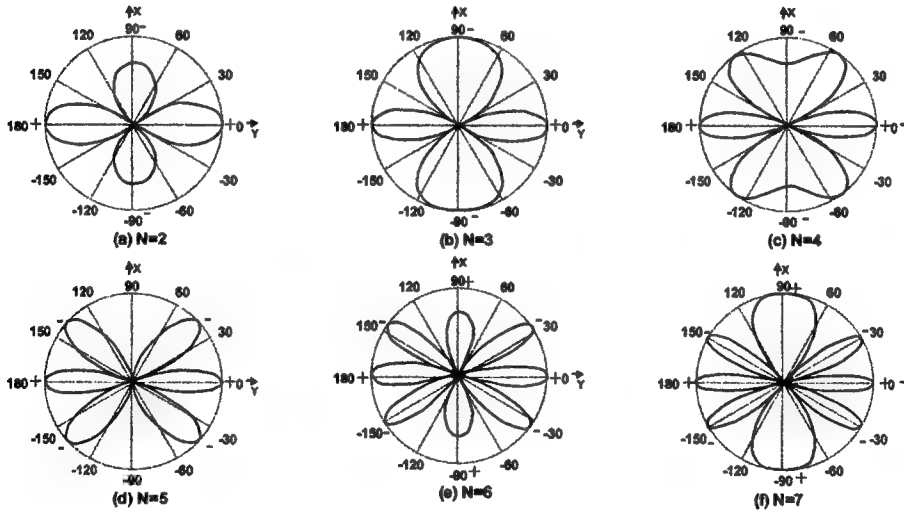


Figure 3.13: The Azimuthal radiation pattern of the interferometer array factor is plotted for

$d = \lambda_o/2$ ,  $\theta_o = \pi/6$ , and  $d_{IFM}$  equal to (a)  $3\lambda_o/2$ , (b)  $2\lambda_o$ , (c)  $5\lambda_o/2$ , (d)  $3\lambda_o$ , (e)  $7\lambda_o/2$ , and (f)  $4\lambda_o$ .

This vertical pattern is plotted in Figure 3.14 as  $N$  varies from  $N = 2$  to  $N = 7$ . First, focus on the patterns at the coordinates  $\theta_o = \pi/2, \alpha_o = \pm\pi/2$ . By comparing the plots in Figure 3.11 with those in Figure 3.14, it is important to note that the vertical pattern experiences a broad null for the very same values of  $N$  that yields a broad null in the horizontal pattern. Next, focus on the patterns at the coordinates  $\theta_o = \pi/6, \alpha_o = \pm\pi/2$ . The major lobes at  $\alpha = \pm\pi/2$  in Figures 3.13 (b) and (f) are seen to coincide with the major lobes at  $\theta = 30^\circ$  in Figures 3.14 (b) and (f) for  $N = 3$  and  $7$ , respectively. Similarly, the nulls at  $\alpha = \pm\pi/2$  in Figure 3.13 (d) are seen to coincide with the null at  $\theta = 30^\circ$  in Figure 3.14 (d) for  $N = 5$ . Finally, the values at  $\alpha = \pm\pi/2$  in Figures 3.13 (a), (c), and (e) are seen to be due to "cuts" through the major lobes located at  $\theta = 41.8^\circ, \theta = 23.6^\circ$  and  $\theta = 34.9^\circ$ , respectively, in Figures 3.14 (a), (c), and (e).

### 3.2 Main Radar Antenna Pattern

As shown in Figure 3.10, the main radar antenna is assumed to be composed of  $N$  dipole antenna elements equispaced by a distance,  $d$ , along the  $x$ -axis. Assuming each of the  $N$  elements is excited by the same sinusoidal source at frequency,  $\omega_o$ , the total electric field at a point  $P$  in the far field with coordinates,  $(r, \theta, \alpha)$ , can be shown to be given by [5]

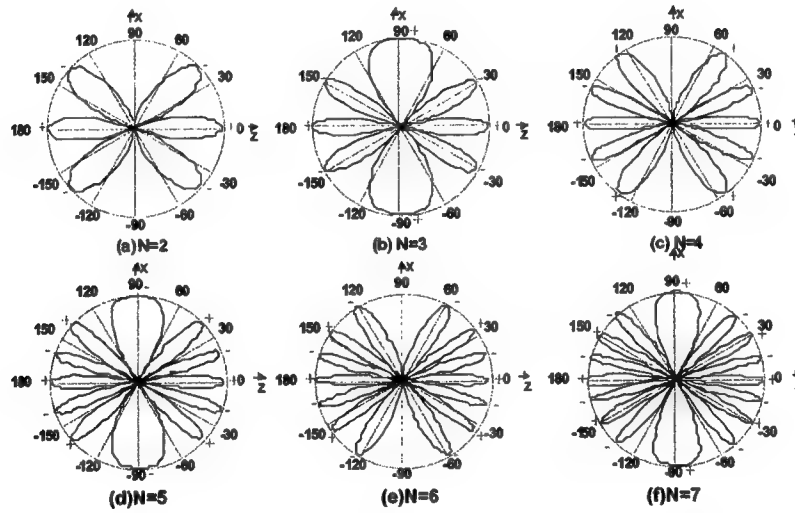


Figure 3.14: The vertical radiation pattern of the interferometer array factor is plotted for  $d = \lambda_o/2$ ,  $\alpha_o = \pm\pi/2$ , and  $d_{IFM}$  equal to (a)  $3\lambda_o/2$ , (b)  $2\lambda_o$ , (c)  $5\lambda_o/2$ , (d)  $3\lambda_o$ , (e)  $7\lambda_o/2$ , and (f)  $4\lambda_o$ .

$$E_{RAD}^{TOT} \approx \frac{NK}{r} F(\theta) F_{RAD}(\theta, \alpha) e^{-j\beta_o r} e^{j\omega_o t} \quad (3.56)$$

where, as in Section 3.1,  $K$  is a constant,  $\beta_o$  is defined in Equation (3.3), and  $F_{RAD}(\theta, \alpha)$  is the main radar array factor with

$$F_{RAD}(\theta, \alpha) = \frac{1}{N} \frac{\sin[N\pi(d/\lambda_o)\sin\theta\sin\alpha]}{\sin[\pi(d/\lambda_o)\sin\theta\sin\alpha]}. \quad (3.57)$$

Observe that the maximum value of  $|F_{RAD}(\theta, \alpha)|$  is unity. Of course, with  $N=2$ , the above array factor should reduce to that for the interferometer. When  $N=2$ ,

$$F_{RAD}(\theta, \alpha) = \frac{1}{2} \frac{\sin[2\pi(\frac{d}{\lambda_o})\sin\theta\sin\alpha]}{\sin[\pi(\frac{d}{\lambda_o})\sin\theta\sin\alpha]}. \quad (3.58)$$

Making use of the trigonometric identity,

$$\sin 2x = 2 \sin x \cos x, \quad (3.59)$$

Equation (3.58) simplifies to

$$F_{RAD}(\theta, \alpha) = \cos[\pi(d/\lambda_o)\sin\theta\sin\alpha]. \quad (3.60)$$

This is identical to Equation (3.22) where  $d_{IFM}$  appears in place of  $d$ .

Of particular interest is the case for which

$$d = \lambda_o / 2. \quad (3.61)$$

Then the main radar array factor becomes

$$F_{RAD}(\theta, \alpha) = \frac{1}{N} \frac{\sin[N(\pi/2)\sin\theta\sin\alpha]}{\sin[(\pi/2)\sin\theta\sin\alpha]}. \quad (3.62)$$

For this choice of  $d$ , it can be shown that the array factor given by Equation (3.62) does not contain any grating lobes. The array factor has a maximum value of unity which occurs for  $\alpha = 0^\circ, 180^\circ$ . The zeros of the array factor occur when its numerator is zero but the denominator is not simultaneously zero. Thus, zeros result when

$$N \frac{\pi}{2} \sin\theta \sin\alpha = n\pi \quad (3.63)$$

where

$$n = \pm 1, \pm 2, \pm 3, \dots \quad (3.64)$$

Since  $\alpha = 0^\circ$  corresponds to a maximum, note that  $n = 0$  is excluded. At a null

$$\sin\alpha = \frac{2n}{N \sin\theta}. \quad (3.65)$$

Because  $|\sin\alpha|$  cannot exceed unity, it follows that

$$|n| \leq \left| \frac{N \sin\theta}{2} \right|. \quad (3.66)$$

Consequently, at a null,  $n$  can be any integer which is restricted to the range.

$$0 < |n| \leq \left| \frac{N \sin \theta}{2} \right|. \quad (3.67)$$

The sidelobes of the main radar array factor are now investigated. Assume  $N$  is large enough such that the denominator of Equation (3.62) varies slowly relative to fluctuations in the numerator. The sidelobe peaks then correspond to maxima of the numerator. These result when

$$N \frac{\pi}{2} \sin \theta \sin \alpha = \frac{m\pi}{2} \quad (3.68)$$

where  $m$  is an odd integer. Equivalently, sidelobe peaks occur when

$$\sin \alpha = \frac{m}{N \sin \theta} \quad (3.69)$$

where  $m$  is an odd integer. Note that  $m = \pm 1$  in Equation (3.69) yields

$$\alpha = \sin^{-1} \left[ \pm \frac{1}{N \sin \theta} \right]. \quad (3.70)$$

However, according to Equation (3.65), the first nulls on either side of the main beam at  $\alpha = 0^\circ$  occur for

$$\alpha = \sin^{-1} \left[ \pm \frac{2}{N \sin \theta} \right]. \quad (3.71)$$

Since

$$\left| \sin^{-1} \left[ \pm \frac{1}{N \sin \theta} \right] \right| < \left| \sin^{-1} \left[ \pm \frac{2}{N \sin \theta} \right] \right|, \quad (3.72)$$

the sidelobe peaks corresponding to  $m = \pm 1$  fall within the main beam centered at  $\alpha = 0^\circ$ . Hence,  $m = \pm 1$  are excluded from the allowable values of  $m$ . Because  $|\sin \alpha|$  cannot exceed unity, note from Equation (3.69) that

$$|m| \leq |N \sin \theta|. \quad (3.73)$$

In summary, it is concluded that the sidelobe peaks occur for integer values of  $m$  such that Equation (3.69) is satisfied where

$$1 < |m| \leq |N \sin \theta|. \quad (3.74)$$

The width of the main beam at  $\alpha = 0^\circ$  is of interest. Let the beamwidth be measured between the first nulls on either side of the main beam. Denote the angles of these nulls by  $\alpha_{1^{st} \text{ null}}$ . From Equation (3.65),

$$\sin(\alpha_{1^{st} \text{ null}}) = \pm \frac{2}{N \sin \theta}. \quad (3.75)$$

For  $N$  sufficiently large relative to  $\sin \theta$ ,

$$|\alpha_{1^{st} \text{ null}}| \ll 1. \quad (3.76)$$

Then

$$\sin(\alpha_{1^{st}-null}) \approx \alpha_{1^{st}-null}. \quad (3.77)$$

It follows that

$$\alpha_{1^{st}-null} \approx \pm \frac{2}{N \sin \theta}. \quad (3.78)$$

The beamwidth is then given by

$$BW_{1^{st}-nulls} = 2|\alpha_{1^{st}-null}| \approx \frac{4}{N|\sin \theta|}. \quad (3.79)$$

In some cases, the beamwidth is measured between the 3-dB points of the main beam. Let the angles at which the 3-dB points occur be denoted by  $\alpha_{3-dB}$ . By definition, these are the angles for which the magnitude of the array factor is equal to  $1/\sqrt{2} = 0.707$ . It follows that

$$\left| \frac{1}{N} \frac{\sin[N \frac{\pi}{2} \sin \theta \sin(\alpha_{3-dB})]}{\sin[\frac{\pi}{2} \sin \theta \sin(\alpha_{3-dB})]} \right| = 0.707. \quad (3.80)$$

For suitable choices of  $\theta$  and  $N$

$$|\alpha_{3-dB}| \ll |\sin \theta| \leq 1. \quad (3.81)$$

Then

$$\sin(\alpha_{3-dB}) \approx \alpha_{3-dB} \quad (3.82)$$

and

$$\sin\left[\frac{\pi}{2} \sin \theta \sin(\alpha_{3-dB})\right] \approx \alpha_{3-dB} \frac{\pi}{2} \sin \theta. \quad (3.83)$$

With these approximations, Equation (3.80) simplifies to

$$\sin\left[\alpha_{3-dB} \frac{N\pi}{2} \sin \theta\right] \approx 0.707 \alpha_{3-dB} \frac{N\pi}{2} \sin \theta. \quad (3.84)$$

This is a transcendental equation which can be solved either graphically or numerically. The horizontal radiation pattern is obtained when  $\theta = \pi/2$ . Equation (3.84) becomes

$$\sin\left[\alpha_{3-dB} \frac{N\pi}{2}\right] \approx 0.707 \alpha_{3-dB} \frac{N\pi}{2}. \quad (3.85)$$

The solution to this equation is

$$\alpha_{3-dB} = \pm \frac{0.886}{N}, \quad (3.86)$$

as can be verified through substitution. It follows that



$$BW_{3-dB} = 2|\alpha_{3-dB}| \approx \frac{1.772}{N} \quad (3.87)$$

for the main beam of the horizontal radiation pattern.

The following properties of the main radar array factor hold as  $N$  increases:

1. The main lobe narrows,
2. The number of sidelobes increase,
3. The peak magnitudes of the sidelobes decrease.

By way of example, the horizontal radiation pattern is plotted in Figure 3.15 for

$$d = \frac{\lambda_o}{2}, \theta = \frac{\pi}{2}, N = 6.$$

Analytically, this is given by

$$\left| F_{RAD} \left( \frac{\pi}{2}, \alpha \right) \right| = \left| \frac{1}{6} \frac{\sin[3\pi \sin \alpha]}{\sin[\frac{\pi}{2} \sin \alpha]} \right|. \quad (3.88)$$

The first nulls on either side of the main beam at  $\alpha = 0^\circ$  occur for

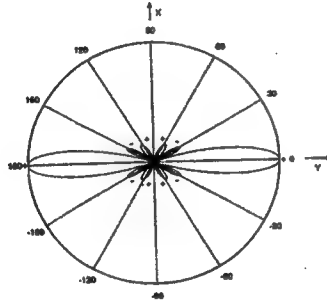


Figure 3.15: The azimuthal radiation pattern of the main radar array factor is plotted for  $d = \frac{\lambda_o}{2}$ ,  $\theta = \frac{\pi}{2}$ , and  $N=6$ .

$$\alpha_{1^{st}-null} = \pm 19.5^\circ. \quad (3.89)$$

Consequently,

$$BW_{1^{st}-nulls} = 39^\circ. \quad (3.90)$$

The approximate expression for this beamwidth, as given by Equation (3.79), yields

$$BW_{1^{st}-nulls} \approx \frac{4}{N} = \frac{4}{6} = \frac{2}{3} \text{ radians} = 38.2^\circ. \quad (3.91)$$

These two results are seen to be in close agreement. In addition, the approximate expression in Equation (3.87) for the beamwidth, as measured between the 3-dB points, yields

$$BW_{3-dB} \approx \frac{1.772}{N} = \frac{1.772}{6} = 0.295 \text{ radians} = 16.9^\circ. \quad (3.92)$$

Consequently,

$$\alpha_{3-dB} \approx 0.1475 \text{ radians}. \quad (3.93)$$

Substitution of this value in Equation (3.88) results in

$$\left| F_{RAD} \left( \frac{\pi}{2}, 0.1475 \right) \right| = 0.716 \quad (3.94)$$

which is reasonably close to the correct value of 0.707.

As mentioned in Section 3.1, it may be desirable to steer the interferometer pattern such that the broad null of the interferometer is centered on the main beam of the radar. With reference to Figures 3.11 (e) and 3.15, observe that the broad null of the interferometer is positioned at  $\alpha = 90^\circ$  while the main beam of the radar is at  $\alpha = 0^\circ$ . Issues involved with steering the interferometer and positioning the broad null are discussed in Section 3.3.

### 3.3 Steering the Interferometer Along With Positioning the Broad Null

As shown in Figure 3.11, a broad null appears in the horizontal radiation pattern of the interferometer array factor when  $d = \lambda_o / 2$ ,  $\theta_o = \pi / 2$ , and  $N$  is an even integer. To minimize interference in target returns received by the main radar, which could consist of both the interferometer and radar signals, it is desirable that the broad null of the interferometer be centered on the main beam of the radar. In addition, a steering capability should be incorporated into the interferometer so that separate communications signals can be directed to different receivers located at various angles. These considerations are treated in this section.

#### 3.3.1 Steering the Interferometer

The interferometer pair can be steered by inserting an appropriate phase shift into each channel. In particular, with reference to Figure 3.4, let the phase shift associated with the element at position B be  $\psi_1$  and the phase shift associated with the element at position A be  $\psi_2$  where

$$\psi_2 = \psi_1 - \Delta\psi. \quad (3.95)$$

The total electric field at point, P, is given by the real part of

$$E_{IFM}^{TOT} = \left[ \frac{K}{r_1} F(\theta_1) e^{-j\beta_o r_1} e^{j\psi_1} + \frac{K}{r_2} F(\theta_2) e^{-j\beta_o r_2} e^{j\psi_2} \right] e^{j\omega_o t} \quad (3.96)$$

where  $\omega_o$  is the frequency of the sinusoidal excitation. Let P be in the far field such that the approximations of Equations (3.6), (3.8), (3.9), and (3.12) are valid. It follows that

$$E_{IFM}^{TOT} \approx \frac{K}{r} F(\theta) e^{-j\beta_o r} e^{j\psi_1} \left[ e^{-j\beta_o(\Delta r)} + e^{j\beta_o(\Delta r)} e^{-j(\Delta\psi)} \right] e^{j\omega_o t} \quad (3.97)$$

However, the bracket in Equation (3.97) can be expressed as

$$e^{-j\left(\frac{\Delta\psi}{2}\right)} \left[ e^{-j\beta_o(\Delta r)} e^{j\left(\frac{\Delta\psi}{2}\right)} + e^{j\beta_o(\Delta r)} e^{-j\left(\frac{\Delta\psi}{2}\right)} \right] = 2 \cos \left[ \beta_o(\Delta r) - \frac{\Delta\psi}{2} \right] e^{-j\left(\frac{\Delta\psi}{2}\right)}. \quad (3.98)$$

From Equations (3.14), (3.16), and (3.20)

$$\Delta r = \frac{d_{IFM}}{2} \sin \theta \sin \alpha. \quad (3.99)$$

Also, making use of Equations (3.3) and (3.24), Equation (3.97) becomes

$$E_{IFM}^{TOT} \approx \frac{2K}{r} F(\theta) F_{IFM}(\theta, \alpha, \Delta\psi) e^{-j\beta_o r} e^{j(\omega_o t + \psi_1 - \frac{\Delta\psi}{2})} \quad (3.100)$$

where the interferometer array factor is now given by

$$F_{IFM}(\theta, \alpha, \Delta\psi) = \cos \left[ (N+1)\pi \left( \frac{d}{\lambda_o} \right) \sin \theta \sin \alpha - \frac{\Delta\psi}{2} \right]. \quad (3.101)$$

It is seen that the array factor is independent of  $\psi_1$ . Only the phase difference between the phase shifts applied to the two interferometer elements plays a role in steering the array factor.

The maximum value of  $|F_{IFM}(\theta, \alpha, \Delta\psi)|$  is unity and occurs when

$$(N+1)\pi \left( \frac{d}{\lambda_o} \right) \sin \theta \sin \alpha - \frac{\Delta\psi}{2} = m\pi \quad (3.102)$$

where

$$m = 0, \pm 1, \pm 2, \dots$$

The minimum value of  $|F_{IFM}(\theta, \alpha, \Delta\psi)|$  is zero and occurs when

$$(N+1)\pi \left( \frac{d}{\lambda_o} \right) \sin \theta \sin \alpha - \frac{\Delta\psi}{2} = n\frac{\pi}{2} \quad (3.103)$$

where

$$n = \pm 1, \pm 3, \pm 5, \dots \quad (3.104)$$

The maxima and zeros of  $|F_{IFM}(\theta, \alpha, \Delta\psi)|$  are seen to be a function of the phase difference,  $\Delta\psi$ . Hence, the interferometer array factor can be steered through an appropriate choice for  $\Delta\psi$ .

It is convenient to measure  $\Delta\psi$  in units of  $\pi$  radians. Consequently, let

$$\Delta\psi = k\pi \quad (3.105)$$

where  $k$  is an appropriately chosen constant. To consider the azimuthal radiation pattern, let  $\theta$  equal the fixed angle,  $\theta_o$ . The maxima are now governed by

$$\sin \alpha = \frac{m + \frac{k}{2}}{(N+1) \frac{d}{\lambda_o} \sin \theta_o} \quad (3.106)$$

where  $m$  is an integer such that

$$\left| m + \frac{k}{2} \right| \leq (N+1) \left( \frac{d}{\lambda_o} \right) |\sin \theta_o|. \quad (3.107)$$

Similarly, the locations of the nulls are determined from

$$\sin \alpha = \frac{\frac{1}{2}(n+k)}{(N+1) \left( \frac{d}{\lambda_o} \right) \sin \theta_o} \quad (3.108)$$

where  $n$  is an odd integer such that

$$\left| \frac{1}{2}(n+k) \right| \leq (N+1) \left( \frac{d}{\lambda_o} \right) |\sin \theta_o|. \quad (3.109)$$

As was done in Section 3.1, it can be shown that minor lobes cannot exist except at  $\alpha = \pm\pi/2$  where either a major lobe, minor lobe, or inflection point is possible.

To gain insight into the consequences of steering the interferometer array, let

$$d = \frac{\lambda_o}{2}, \theta_o = \frac{\pi}{2}. \quad (3.110)$$

The array factor is now given by

$$F_{IFM} \left( \frac{\pi}{2}, \alpha, k\pi \right) = \cos \left[ \left( \frac{N+1}{2} \sin \alpha - \frac{k}{2} \right) \pi \right]. \quad (3.111)$$

Equations (3.106) and (3.107), governing the maxima, simplify to

$$\sin \alpha = \frac{2m+k}{N+1} \quad (3.112)$$

where  $m$  is an integer such that

$$\left| m + \frac{k}{2} \right| \leq \frac{N+1}{2} \quad (3.113)$$

while Equations (3.108) and (3.109), governing the nulls, reduce to

$$\sin \alpha = \frac{n+k}{N+1} \quad (3.114)$$

where  $n$  is an odd integer such that

$$|n + k| \leq N + 1. \quad (3.115)$$

For the unsteered interferometer, it is seen from Figure 3.11 that a major lobe occurs at  $\alpha = 0^\circ$  for all integer values of  $N$ . Consider steering this lobe to  $\alpha = 10^\circ$  when  $N = 2$  and  $N = 7$ . For the unsteered array, the major lobe at  $\alpha = 0^\circ$  results when  $m = 0$ . Hence, let  $m = 0$  and  $\alpha = 10^\circ$  in Equation (3.112). Solution for  $k$  yields

$$k = 0.522 \quad (3.116)$$

when  $N = 2$  and

$$k = 1.392 \quad (3.117)$$

when  $N = 7$ . Polar plots of  $|F_{IFM}(\frac{\pi}{2}, \alpha, k\pi)|$  are presented in Figure 3.16 for these two cases.

Comparisons of Figure 3.11(a) with Figure 3.16 (a) and Figure 3.11 (f) with Figure 3.16 (b) reveal that the major lobe at  $\alpha = 0^\circ$  has, in fact, been steered to  $\alpha = 10^\circ$ . Note that symmetry about the y-axis no longer exists in the steered arrays although symmetry about the x-axis is maintained. For the case in which  $N = 2$ , the broad null at  $\alpha = 90^\circ$  in Figure 3.11 (a) has disappeared and the two major lobes at  $\alpha = 41.8^\circ$  and  $\alpha = 138.2^\circ$  have merged together into a single broad lobe centered at  $\alpha = 90^\circ$  in Figure 3.16 (a). Also, at  $\alpha = -90^\circ$ , note that there is now a minor lobe in the steered array whereas there is a null in Figure 3.11(a). For the case in which  $N = 7$ , the major lobe at  $\alpha = 90^\circ$  in Figure 3.11 (f) has disappeared and the two major lobes at  $\alpha = 48.6^\circ$  and  $\alpha = 131.4^\circ$  have merged together into a single broad lobe centered at  $\alpha = 90^\circ$  in Figure 3.16 (b). Also, at  $\alpha = -90^\circ$ , the major lobe in Figure 3.11 (f) has, in effect, split into two major lobes at  $\alpha = -55.7^\circ$  and  $\alpha = -124.3^\circ$  as well as introduced a minor lobe of opposite polarity. We see that severe distortion can occur in the array factor radiation pattern when the interferometer is steered.

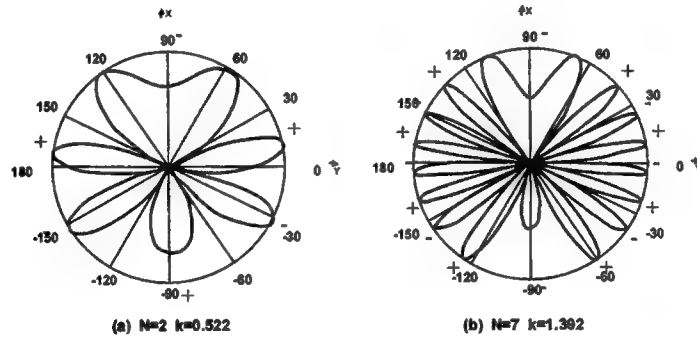


**Figure 3.16:** The azimuthal radiation pattern of the interferometer array factor is plotted when the major lobe at  $\alpha = 0^\circ$  in Figure 3.11 is steered to  $\alpha = 10^\circ$  for  $d = \lambda_0 / 2$ ,  $\theta_0 = \pi / 2$ , and  $d_{IFM}$  equal to (a)  $3\lambda_0 / 2$  and (b)  $4\lambda_0$

### 3.3.2 Positioning the Broad Null by Steering the Interferometer

A major objective for steering the interferometer is to center its broad null on the main beam of the radar. As pointed out in Section 3.2, the main beam of the radar is located at  $\alpha = 0^\circ$ . This is illustrated in Figure 3.15.

Consequently, using the results of Section 3.3.1, we attempt to locate a broad null at  $\alpha = 0^\circ$  by steering the interferometer.

We first consider the case for  $N = 2$ ,  $d = \lambda_o / 2$ , and  $\theta_o = \pi / 2$ . As seen in Figure 3.11 (a), a broad null occurs at  $\alpha = -90^\circ$ . This resulted for  $n = -3$ , in Equation (3.50). Hence, let  $n = -3$ ,  $\alpha = 0^\circ$  and  $N = 2$  in Equation (3.114) in order to rotate the broad null at  $\alpha = -90^\circ$  to  $\alpha = 0^\circ$ . Solution for  $k$  yields

$$k = 3. \quad (3.118)$$

A polar plot of  $\left| F_{IFM} \left( \frac{\pi}{2}, \alpha, 3\pi \right) \right|$ , as obtained using Equation (3.111), is shown in Figure 3.17 (a). As expected, there is a null at  $\alpha = 0^\circ$ . However, it is not a broad null! This is confirmed by noting that the polarities of the major lobes at  $\alpha = \pm 19.5^\circ$  are of opposite signs. Interestingly, the major lobes in Figure 3.17 (a) are positioned at the null in Figure 3.11 (a) and the nulls in Figure 3.17 (a) are positioned at the major lobes in Figure 3.11 (a).

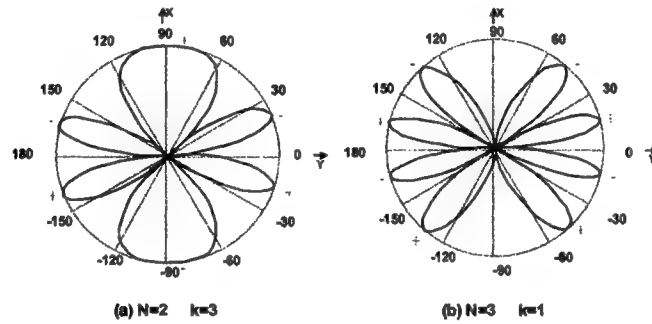


**Figure 3.17:** The azimuthal radiation pattern of the interferometer array factor is plotted when nulls in Figure 3.11 are steered to  $\alpha = 0^\circ$  for  $d = \lambda_o / 2$ ,  $\theta_o = \pi / 2$  and  $d_{IFM}$  equal to (a)  $3\lambda_o / 2$  and (b)  $2\lambda_o$ .

Having failed with  $N$  even, an attempt is now made to locate a broad null at  $\alpha = 0^\circ$  for  $N$  odd. Consider  $N = 3$ ,  $d = \lambda_o / 2$ , and  $\theta_o = \pi / 2$ . As seen in Figure 3.11 (b), a narrow null occurs at  $\alpha = -14.5^\circ$  when  $n = -1$  in Equation (3.50). Hence, let  $n = -1$ ,  $\alpha = 0^\circ$  and  $N = 3$  in Equation (3.114) in order to rotate the null at  $\alpha = -14.5^\circ$  to  $\alpha = 0^\circ$ . Solution for  $k$  yields

$$k = 1. \quad (3.119)$$

A polar plot of  $\left| F_{IFM} \left( \pi / 2, \alpha, \pi \right) \right|$ , as obtained using Equation (3.111), is shown in Figure 3.17 (b). As expected, there is a null at  $\alpha = 0^\circ$ . However, because of the alternation in polarity of the major lobes located at  $\alpha = \pm 14.5^\circ$ , the null at  $\alpha = 0^\circ$  is not a broad null! Interestingly enough, there are now broad nulls at  $\alpha = \pm 90^\circ$ . As was the situation with  $N = 2$ , the major lobes in Figure 3.17 (b) are positioned at the nulls in Figure 3.11 (b) and the nulls in Figure 3.17 (b) are positioned at the major lobes in Figure 3.11 (b).

Although it was possible to steer nulls to  $\alpha = 0^\circ$  for  $N=2$  and  $N=3$ , these were not broad nulls. This raises the question, "Is it possible to place a broad null at  $\alpha = 0^\circ$ ?" From Equation (3.114) the nulls of

$$F_{IFM}\left(\frac{\pi}{2}, \alpha, k\pi\right)$$

occur when

$$\sin \alpha = \frac{n+k}{N+1} \quad (3.114)$$

where  $n$  is an odd integer. The solution for  $k$  with  $\alpha = 0^\circ$  is

$$k = -n. \quad (3.120)$$

Thus,  $k$  is an odd integer. Note that

$$\cos\left[x + \frac{k\pi}{2}\right] = \pm \sin x \quad (3.121)$$

for  $k$  an odd integer. It follows that the array factor in Equation (3.111) becomes

$$F_{IFM}\left(\frac{\pi}{2}, \alpha, k\pi\right) = \pm \sin\left[\frac{(N+1)\pi}{2} \sin \alpha\right] \quad (3.122)$$

when a null is steered to  $\alpha = 0^\circ$ . To have a broad null at  $\alpha = 0^\circ$ , it is necessary that the major lobes located on either side of  $\alpha = 0^\circ$  have the same polarity. However, this is not possible because

$$F_{IFM}\left(\frac{\pi}{2}, \alpha, k\pi\right) = -F_{IFM}\left(\frac{\pi}{2}, -\alpha, k\pi\right). \quad (3.123)$$

It is concluded that it is not possible to steer a broad null to  $\alpha = 0^\circ$ . In addition, the fact that the unsteered interferometer has an array factor given by

$$F_{IFM}\left(\frac{\pi}{2}, \alpha, 0\right) = \cos\left[\left(\frac{N+1}{2}\right)\pi \sin \alpha\right] \quad (3.124)$$

while the interferometer steered to have a null at  $\alpha = 0^\circ$  has an array factor given by equation (3.122) explains why the maxima of one occur at the nulls of the other.

### 3.3.3 Placement of Interferometer Along the y-Axis

To obtain a broad null at  $\alpha = 0^\circ$ , it is necessary to place the interferometer on the y-axis while the linear array of the main radar remains along the x-axis. As before, let the two dipole antennas of the interferometer pair be directed in the z-direction. However, as shown in Figure 3.18, the elements are now placed on the y-axis at  $y = -d_{IFM}/2$  and  $y = +d_{IFM}/2$ , respectively. The corresponding geometry for evaluation of the electric field at point P, is illustrated in Figure 3.19.

The analysis proceeds exactly in the same manner as in Section 3.1 where the interferometer was placed along the x-axis. The only difference is that, in place of  $\gamma$ , the angle,  $\delta$ , is involved where  $\delta$  is the angle between  $\vec{a}_r$  and  $\vec{a}_y$ , the unit vector in the y-direction. Consequently,  $\cos \delta$  is the projection of

$\vec{a}_r$  on  $\vec{a}_y$  and is given by

$$\cos \delta = \vec{a}_r \cdot \vec{a}_y = \sin \theta \sin \phi = \sin \theta \cos \alpha. \quad (3.125)$$

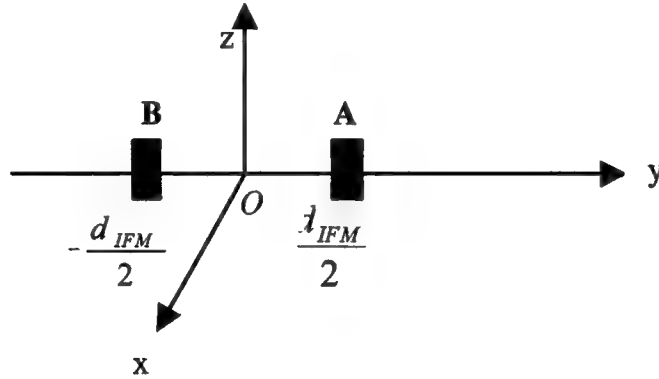


Figure 3.18: The dipole antennas are placed along the y-axis at A and B and are directed in the z-direction.

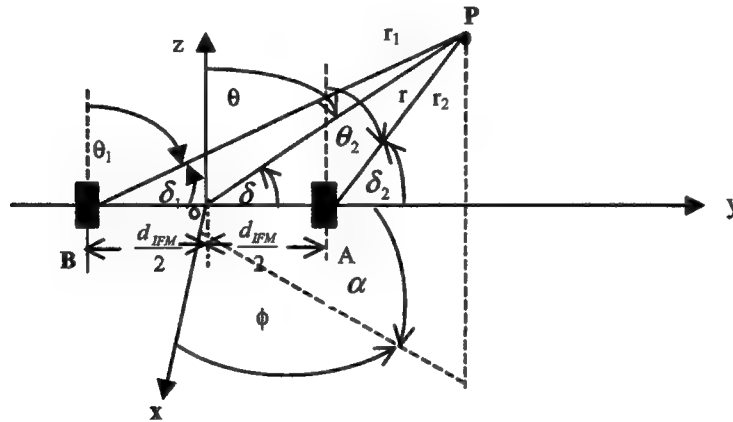


Figure 3.19: The geometry is shown for evaluation of the electric field at point, P.

Corresponding to Equation (3.14), we have

$$\Delta r = \frac{d_{IFM}}{2} \cos \delta = \frac{d_{IFM}}{2} \sin \theta \cos \alpha. \quad (3.126)$$



In the far field it follows that the total electric field at point, P, is given by

$$E_{IFM}^{TOT} \approx \frac{2K}{r} F(\theta) F_{IFM}(\theta, \alpha) e^{-j\beta_o r} e^{j\omega_o t} \quad (3.127)$$

where the interferometer array factor is given by

$$F_{IFM}(\theta, \alpha) = \cos\left[\pi \left(\frac{d_{IFM}}{\lambda_o}\right) \sin \theta \cos \alpha\right]. \quad (3.128)$$

This is identical to the expression for the array factor given in Equation (3.22) except that  $\sin \alpha$  has been replaced by  $\cos \alpha$ .

Because the interferometer elements no longer straddle the main radar elements on the x-axis, the spacing between the interferometer elements is no longer given by Equation (3.24). Instead it is convenient to measure the interferometer spacing in units of half wavelength. Therefore, the interferometer spacing is defined to be

$$d_{IFM} = k_s \frac{\lambda_o}{2} \quad (3.129)$$

where  $k_s$  is a constant. When  $d$ , the spacing between the main radar antenna elements, is a half wavelength,  $k_s$  is analogous to  $(N+1)$  of Equation (3.24). Substitution of Equation (3.129) in Equation (3.128) yields

$$F_{IFM}(\theta, \alpha) = \cos\left[\frac{k_s \pi}{2} \sin \theta \cos \alpha\right]. \quad (3.130)$$

The maxima of  $|F_{IFM}(\theta, \alpha)|$  occur for

$$\cos \alpha = \frac{2m}{k_s \sin \theta} \quad (3.131)$$

where  $m$  is an integer such that

$$|m| \leq \frac{k_s \sin \theta}{2}. \quad (3.132)$$

Similarly, the nulls of  $|F_{IFM}(\theta, \alpha)|$  are governed by

$$\cos \alpha = \frac{n}{k_s \sin \theta} \quad (3.133)$$

where  $n$  is an odd integer such that

$$|n| \leq k_s \sin \theta. \quad (3.134)$$

Polar plots of the azimuthal radiation pattern of the interferometer array factor, where the elements are on the y-axis, are presented in Figure 3.20 for  $\theta = \pi/2$  and  $k_s = 3, 5$ , and  $7$ . Note that these values of  $k_s$  correspond to  $d_{IFM} = 3\lambda_o/2, 5\lambda_o/2$  and  $7\lambda_o/2$ , respectively. As expected, because  $k_s$  is an odd integer for each of the plots, a broad null is seen to exist at  $\alpha = 0^\circ$  in each case. Comparison of Figures 3.11 (a), (c), and (e) with Figures 3.20 (a), (b), and (c), respectively, reveals that the horizontal radiation pattern of the interferometer positioned on the y-axis is identical to that of the interferometer positioned on the x-axis except that one is rotated  $90^\circ$  with respect to the other.

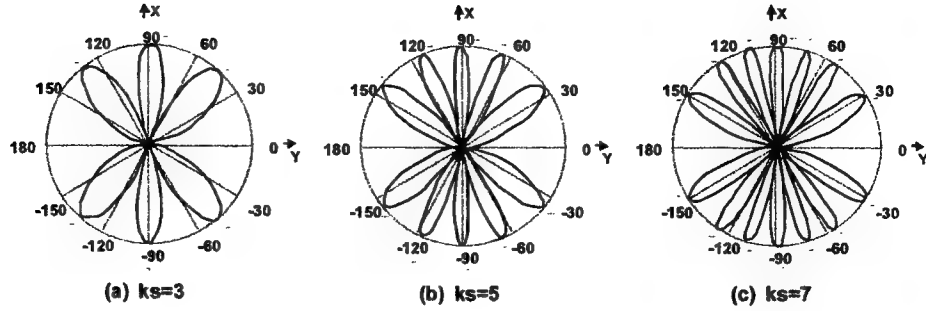


**Figure 3.20:** The azimuthal radiation pattern of the interferometer array factor, where the elements are on the y-axis, is plotted for  $\theta = \pi/2$  and  $d_{IFM}$  equal to (a)  $3\lambda_o/2$ , (b)  $5\lambda_o/2$  and (c)  $7\lambda_o/2$ .

### 3.3.4 Evaluation of Broad Null at $\alpha = 0^\circ$

In Section 3.3.2 the interferometer was steered to produce a null at  $\alpha = 0^\circ$ , as shown in Figure 3.17 (a). However, this was not a broad null. In Section 3.3.3, a broad null was located at  $\alpha = 0^\circ$  by positioning the interferometer elements on the y-axis, as shown in Figure 3.20 (a). In both cases the spacing between the interferometer elements is

$$d_{IFM} = \frac{3\lambda_o}{2}. \quad (3.135)$$

It is of interest to compare the width of the steered null in Figure 3.17 (a) to that of the broad null in Figure 3.20 (a).

From Equation (3.122) the horizontal radiation pattern plotted in Figure 3.17 (a) is given by

$$\left| F_{IFM}\left(\frac{\pi}{2}, \alpha, 3\pi\right) \right| = \left| \sin\left[\frac{3\pi}{2} \sin \alpha\right] \right| \quad (3.136)$$

whereas the horizontal radiation pattern plotted in Figure 3.20 (a), as obtained from Equation (3.130), is

$$\left| F_{IFM}\left(\frac{\pi}{2}, \alpha\right) \right| = \left| \cos\left[\frac{3\pi}{2} \cos \alpha\right] \right|. \quad (3.137)$$

Converting to dB, Equations (3.136) and (3.137) become

$$20 \log_{10} \left\{ \left| F_{IFM}\left(\frac{\pi}{2}, \alpha, 3\pi\right) \right| \right\} = 20 \log_{10} \left\{ \left| \sin\left[\frac{3\pi}{2} \sin \alpha\right] \right| \right\} \quad (3.138)$$

and

$$20 \log_{10} \left\{ \left| F_{IFM}\left(\frac{\pi}{2}, \alpha\right) \right| \right\} = 20 \log_{10} \left\{ \left| \cos\left[\frac{3\pi}{2} \cos \alpha\right] \right| \right\}. \quad (3.139)$$

Evaluations of Equations (3.138) and (3.139) about the nulls at  $\alpha = 0^\circ$  are tabulated in Table 3.1. With reference to the table, note that the width of the steered null, when measured between the  $-30$  dB points, is approximately  $0.8^\circ$  while that of the broad null is in excess of  $12^\circ$ . Hence, at the  $-30$  dB points, the broad null is more than 15 times wider than the steered null. At the  $-20$  dB points, the width of the steered null is approximately  $2.5^\circ$  while that of the broad null is in excess of  $22^\circ$ . Thus, at the  $-20$  dB points, the broad null is more than 8.8 times wider than the

steered null. It is concluded that the broad null is considerably more effective than the steered null in establishing spatial orthogonality between the interferometer and radar signals.

For the purpose of a later discussion, the broad nulls of Figure 3.20 (b) and (c) are also examined. The horizontal radiation pattern plotted in Figure 3.20 (b) is

$$\left| F_{IFM} \left( \frac{\pi}{2}, \alpha \right) \right| = \left| \cos \left[ \frac{5\pi}{2} \cos \alpha \right] \right| \quad (3.140)$$

while that plotted in Figure 3.20 (c) is

$$\left| F_{IFM} \left( \frac{\pi}{2}, \alpha \right) \right| = \left| \cos \left[ \frac{7\pi}{2} \cos \alpha \right] \right|. \quad (3.141)$$

Converting to dB, as in Equations (3.138) and (3.139), the results are tabulated in Table 3.2. For the broad null in Figure 3.20 (b) the width is approximately  $10^\circ$  when measured between the  $-30$  dB points and is approximately  $18^\circ$  when measured between the  $-20$  dB points. For the broad null in Figure 3.20 (c) the width is in excess of  $8^\circ$  when measured between the  $-30$  dB points and is in excess of  $14^\circ$  when measured between the  $-20$  dB points. In general, the width of the broad null is narrowed as  $d_{IFM}$  increases by selecting larger values of  $k_s$ .

Table 3.1

Comparison of Steered Null to Broad Null at  $\alpha = 0^\circ$  for  $d_{IFM} = \frac{3\lambda_0}{2}$

Steered Null ( $N=2$ ) Figure 3.17 (a)		Broad Null ( $k_s = 3$ ) Figure 3.20 (a)	
$\alpha$ (Degrees)	$\left  F_{IFM} \left( \frac{\pi}{2}, \alpha, 3\pi \right) \right $ (dB)	$\alpha$ (Degrees)	$\left  F_{IFM} \left( \frac{\pi}{2}, \alpha \right) \right $ (dB)
0	$-\infty$	0	$-\infty$
$\pm 0.1$	-41.7	$\pm 1$	-62.9
$\pm 0.2$	-35.7	$\pm 2$	-50.8
$\pm 0.3$	-32.2	$\pm 3$	-43.8
$\pm 0.4$	-29.7	$\pm 4$	-38.8
$\pm 0.5$	-27.7	$\pm 5$	-34.9
$\pm 0.6$	-26.1	$\pm 6$	-31.7
$\pm 0.7$	-24.8	$\pm 7$	-29.0
$\pm 0.8$	-23.6	$\pm 8$	-26.7
$\pm 0.9$	-22.6	$\pm 9$	-24.7
$\pm 1.0$	-21.7	$\pm 10$	-22.9
$\pm 1.1$	-20.9	$\pm 11$	-21.3
$\pm 1.2$	-20.1	$\pm 12$	-19.8

Table 3.2		
Evaluation of Broad Null at $\alpha = 0^\circ$ for $d_{IFM} = \frac{5\lambda_0}{2}$ and $\frac{7\lambda_0}{2}$		
$\alpha$  (Degrees)	Broad Null ( $k_s = 5$ ) Figure 3.20 (b) $\left  F_{IFM}\left(\frac{\pi}{2}, \alpha\right) \right $ (dB)	Broad Null ( $k_s = 7$ ) Figure 3.20 (c) $\left  F_{IFM}\left(\frac{\pi}{2}, \alpha\right) \right $ (dB)
0	$-\infty$	$-\infty$
$\pm 1$	-58.5	-55.5
$\pm 2$	-46.4	-43.4
$\pm 3$	-39.4	-36.4
$\pm 4$	-34.3	-31.4
$\pm 5$	-30.5	-27.6
$\pm 6$	-27.3	-24.4
$\pm 7$	-24.6	-21.7
$\pm 8$	-22.3	-19.4
$\pm 9$	-20.3	-17.4
$\pm 10$	-18.4	-15.5
$\pm 11$	-16.8	-14.0
$\pm 12$	-15.4	-12.5

The behavior of the vertical pattern at the broad null is, also, of interest. Letting  $\alpha = 0^\circ$  in Equation (3.130), the expression for the interferometer array factor becomes

$$F_{IFM}(\theta, 0) = \cos \left[ \frac{k_s \pi}{2} \sin \theta \right]. \quad (3.142)$$

This yields the vertical pattern at  $\alpha = 0^\circ$ . These are plotted in Figure 3.21 for  $k_s = 3, 5$ , and  $7$ . In all three cases, observe that broad nulls exist at  $\theta = \pm 90^\circ$ . In fact, examination of Equation (3.142) reveals that broad nulls at  $\theta = \pm 90^\circ$  always occur when  $k_s$  is an odd integer. Therefore, assuming that the main radar antenna elements are positioned on the x-axis while the interferometer elements are placed along the y-axis, broad nulls occur broadside to the main radar antenna in both the horizontal and vertical planes whenever  $k_s$  is an odd integer. Also, note that the vertical patterns in Figures 3.21 (a), (b), and (c), where the interferometer elements are along the y-axis and  $\alpha = 0$ , are identical to those in Figures 3.14 (a), (c), and (e), where the interferometer elements are along the x-axis and  $\alpha = \pm \pi / 2$ .

Converting the magnitude of Equation (3.39) to dB results in

$$20 \log_{10} \{F_{IFM}(\theta, 0)\} = 20 \log_{10} \left\{ \cos \left[ \frac{k_s \pi}{2} \sin \theta \right] \right\}. \quad (3.143)$$

Values for Equation (3.143) about  $\theta = 90^\circ$  are tabulated in Table 3.3 for  $k_s = 3, 5$  and  $7$ . By comparing the entries in Table 3.3 with the corresponding entries in Tables 3.1 and 3.2, it is concluded that the broad nulls in the horizontal and vertical planes have identical behaviors.

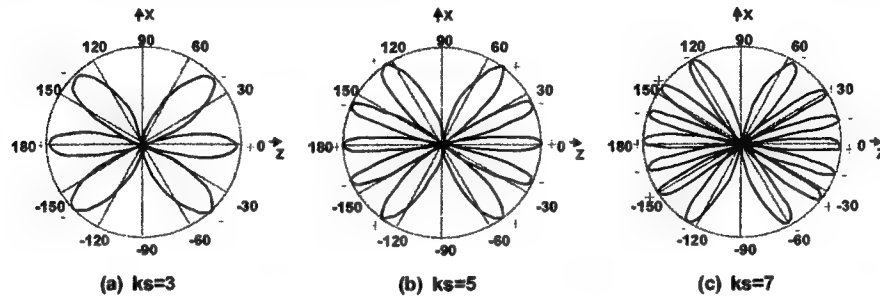


**Figure 3.21:** The vertical radiation pattern of the interferometer array factor, where the elements are on the y-axis, is plotted for  $\alpha = 0$  and  $d_{IFM}$  equal to (a)  $3\lambda_0/2$ , (b)  $5\lambda_0/2$  and (c)  $7\lambda_0/2$ .

Table 3.3			
Evaluation of Broad Null at $\theta = 90^\circ$ for $d_{IFM} = \frac{3\lambda_0}{2}$ , $\frac{5\lambda_0}{2}$ and $\frac{7\lambda_0}{2}$			
$\alpha$	Broad Null ( $k_s = 3$ ) Figure 3.21 (a)	Broad Null ( $k_s = 3$ ) Figure 3.21 (b)	Broad Null ( $k_s = 3$ ) Figure 3.21 (c)
$\theta$ (Degrees)	$ F_{IFM}(\theta, 0) $ (dB)	$ F_{IFM}(\theta, 0) $ (dB)	$ F_{IFM}(\theta, 0) $ (dB)
90	$-\infty$	$-\infty$	$-\infty$
90 $\pm$ 1	-62.9	-58.5	-55.5
90 $\pm$ 2	-50.8	-46.4	-43.4
90 $\pm$ 3	-43.8	-39.4	-36.4
90 $\pm$ 4	-38.8	-34.3	-31.4
90 $\pm$ 5	-34.9	-30.5	-27.6
90 $\pm$ 6	-31.7	-27.3	-24.4
90 $\pm$ 7	-29.0	-24.6	-21.7
90 $\pm$ 8	-26.7	-22.3	-19.4
90 $\pm$ 9	-24.7	-20.3	-17.4
90 $\pm$ 10	-22.9	-18.4	-15.5
90 $\pm$ 11	-21.3	-16.8	-14.0
90 $\pm$ 12	-19.8	-15.4	-12.5

### 3.3.5 Comparison of the Interferometer and Radar Field Strengths Broadside to the Radar

In this section the electric field at a point in the far field due to the interferometer is compared to the electric field at the same point due to the radar. Attention is focused on those points in the main beam of the radar which also fall within the broad null of the interferometer. For this comparison, identical excitations are assumed for the interferometer and radar array.

With reference to Equation (3.21), the total electric field due to the interferometer is

$$E_{IFM}^{TOT} \approx \frac{2K}{r} F(\theta) F_{IFM}(\theta, \alpha) e^{-j\beta_0 r} e^{j\omega_0 t} \quad (3.21)$$

where the array factor is given by Equation (3.130). Similarly, from Equation (3.56), the total electric field due to the radar is

$$E_{RAD}^{TOT} \approx \frac{NK}{r} F(\theta) F_{RAD}(\theta, \alpha) e^{-j\beta_0 r} e^{j\omega_0 t} \quad (3.56)$$

where the array factor is given by Equation (3.57). It follows that the ratio of the field magnitudes is

$$\frac{|E_{IFM}^{TOT}|}{|E_{RAD}^{TOT}|} = \frac{2 |F_{IFM}(\theta, \alpha)|}{N |F_{RAD}(\theta, \alpha)|} \quad (3.144)$$

Conversion of the ratio to dB results in

$$20 \log_{10} \left\{ \frac{|E_{IFM}^{TOT}|}{|E_{RAD}^{TOT}|} \right\} = 20 \log_{10} \{F_{IFM}(\theta, \alpha)\} - 20 \log_{10} \{F_{RAD}(\theta, \alpha)\} - 20 \log_{10} \left\{ \frac{N}{2} \right\} \quad (3.145)$$

Let the point at which the fields are measured be in the x-y plane where the elevation angle is  $\theta = \pi/2$ . Assume the main radar has the azimuthal radiation pattern shown in Fig 3.15 for which  $N=6$  and  $d=\lambda/2$ . Equation (3.145) then becomes

$$20 \log_{10} \left\{ \frac{|E_{IFM}^{TOT}|}{|E_{RAD}^{TOT}|} \right\} = 20 \log_{10} \left\{ \cos \left[ \frac{k_s \pi}{2} \cos \alpha \right] \right\} \quad (3.146)$$

$$-20 \log_{10} \left\{ \frac{1}{6} \frac{\sin[3\pi \sin \alpha]}{\sin[\frac{\pi}{2} \sin \alpha]} \right\} - 9.5 \text{ (dB)}.$$

Note that the first term on the right side of Equation (3.146), corresponding to the interferometer array factor, is tabulated in Tables 3.1 and 3.2 for  $k_s = 3, 5$ , and  $7$ . These are values of  $k_s$  for which a broad null appears at  $\alpha = 0$ . Values for the second term, corresponding to the radar array factor, are tabulated in Table 3.4. From Equation (3.92), the 3-dB bandwidth of the main beam was shown to be approximately  $16.9^\circ$ . This agrees closely with the values given in Table 3.4 for  $\alpha = \pm 8^\circ$  and  $\alpha = \pm 9^\circ$ . Utilizing Tables 3.1, 3.2, and 3.4, results are tabulated in Table 3.5 for interferometer spacings corresponding to  $k_s = 3, 5$ , and  $7$ .

Recall that a variety of interferometer element spacings are possible because the interferometer elements are placed along the y-axis while the main radar elements are positioned along the x-axis. Consequently, the main beam of the radar can be made as narrow as desired to accommodate the width of the broad null of the interferometer. Alternatively, the broad null of the interferometer can be made as wide as needed to accommodate the beamwidth of the radar main beam. The half-power points of the radar coincide with the 3-dB points of its main beam. For this example, the 3-dB points are approximately equal to  $\pm 8.5^\circ$ . From Table 3.5 it is seen that the interferometer field magnitude is at least 31.0, 26.6, and 23.7 dB less than the radar field magnitude, respectively, for the cases corresponding to  $k_s = 3, 5$ , and  $7$ . Recall that these results were obtained assuming identical excitations for the radar and interferometer. Since the interferometer excitation is likely to be considerably smaller than the radar excitation, placement of the broad null of the interferometer at the center of the main beam of the radar is likely to be an effective technique for preventing the interferometer signal from interfering with the desired radar target returns.

Table 3.4	
Evaluation of Radar Main Beam	
$\alpha$	Main Beam (N=6) Figure 3.15
(Degrees)	$\left  F_{RAD} \left( \frac{\pi}{2}, \alpha \right) \right $ (dB)
0	0
$\pm 1$	-0.4
$\pm 2$	-0.18
$\pm 3$	-0.34
$\pm 4$	-0.59
$\pm 5$	-1.01
$\pm 6$	-1.39
$\pm 7$	-1.94
$\pm 8$	-2.58
$\pm 9$	-3.2
$\pm 10$	-4.2
$\pm 11$	-5.2
$\pm 12$	-6.4

Table 3.5

Ratio of Interferometer to Radar Electric Field Magnitudes in the Main Beam of the Radar for  $d_{IFM} = \frac{3\lambda_0}{2}, \frac{5\lambda_0}{2}$  and  $\frac{7\lambda_0}{2}$

$\alpha$ (Degrees)	$k_s = 3$ $\left  \frac{E_{IFM}^{TOT}}{E_{RAD}^{TOT}} \right $ (dB)	$k_s = 5$ $\left  \frac{E_{IFM}^{TOT}}{E_{RAD}^{TOT}} \right $ (dB)	$k_s = 7$ $\left  \frac{E_{IFM}^{TOT}}{E_{RAD}^{TOT}} \right $ (dB)
0	$-\infty$	$-\infty$	$-\infty$
$\pm 1$	-72.4	-68.0	-65.0
$\pm 2$	-60.1	-55.7	-52.7
$\pm 3$	-53.0	-48.6	-45.6
$\pm 4$	-47.7	-43.2	-40.3
$\pm 5$	-43.4	-39.0	-36.1
$\pm 6$	-39.8	-35.4	-32.5
$\pm 7$	-36.6	-32.2	-29.3
$\pm 8$	-33.6	-29.2	-26.3
$\pm 9$	-31.0	-26.6	-23.7
$\pm 10$	-28.2	-23.7	-20.8
$\pm 11$	-25.6	-21.1	-18.3
$\pm 12$	-22.9	-18.5	-15.6

### 3.4 Use of Frequency Modulated Signals to Steer the Interferometer

When the interferometer elements are on the y-axis, the interferometer array factor is

$$F_{IFM}(\theta, \alpha) = \cos \left[ \pi \left( \frac{d_{IFM}}{\lambda_0} \right) \sin \theta \cos \alpha \right]. \quad (3.128)$$

Recalling that

$$\beta_0 = \frac{2\pi f_0}{c} = \frac{2\pi}{\lambda_0}, \quad (3.3)$$

the array factor can, also, be expressed as



$$F_{IFM}(\theta, \alpha) = \cos \left[ \frac{\beta_0}{2} d_{IFM} \sin \theta \cos \alpha \right]. \quad (3.147)$$

The relation in Equation (3.3) can be interpreted as having arisen from the wave equation.

In the far field the propagating wave can be approximated as a spherical wave whose description depends only upon the radial distance,  $r$ , and sinusoidal frequency of excitation,  $f_0$ . Assuming spherical symmetry, the wave equation is given by [6]

$$\frac{\partial^2 [rs(r, t)]}{\partial r^2} = \frac{1}{c^2} \frac{\partial^2 [rs(r, t)]}{\partial t^2} \quad (3.148)$$

where  $c$  is the wave propagation velocity. One solution to this equation is of the form

$$s(r, t) = \frac{K}{r} e^{-j\beta_0 r} e^{j2\pi f_0 t}. \quad (3.149)$$

This can be verified by direct substitution of Equation (3.149) into Equation (3.148). Note that

$$\frac{\partial^2 [rs(r, t)]}{\partial r^2} = -\beta_0^2 K e^{-j\beta_0 r} e^{j2\pi f_0 t} \quad (3.150)$$

while

$$\frac{1}{c^2} \frac{\partial^2 [rs(r, t)]}{\partial t^2} = -\left(\frac{2\pi f_0}{c}\right)^2 K e^{-j\beta_0 r} e^{j2\pi f_0 t}. \quad (3.151)$$

Equality between Equations (3.150) and (3.151) exists provided

$$\beta_0 = \frac{2\pi f_0}{c}. \quad (3.3)$$

Since

$$c = \lambda_0 f_0, \quad (3.152)$$

$\beta_0$  can, also, be written as

$$\beta_0 = \frac{2\pi}{\lambda_0}. \quad (3.3)$$

Examination of Equation (3.144) suggests that the array factor can be varied by changing  $\beta_0$  which is a function of the sinusoidal frequency of excitation. Therefore, it should be possible to make the array factor vary in time by exciting the interferometer with a frequency modulated signal. This observation is examined in Section 3.4.1.

### 3.4.1 Quasi-Stationary Considerations

Assume the interferometer is excited by the frequency modulated signal

$$s_{\text{IFM}}(t) = s(t) = V_m \cos [2\pi f_o t + \phi(t)] . \quad (3.153)$$

By definition, the instantaneous frequency of  $s(t)$  is

$$\begin{aligned} f(t) &= \frac{1}{2\pi} \frac{d}{dt} [2\pi f_o t + \phi(t)] \\ &= f_o + \frac{1}{2\pi} \frac{d\phi(t)}{dt} . \end{aligned} \quad (3.154)$$

For convenience, let

$$\phi(t) = 2\pi g(t) . \quad (3.155)$$

The instantaneous frequency then becomes

$$f(t) = f_o + \frac{dg(t)}{dt} . \quad (3.156)$$

Analogous to Equations (3.149) and (3.3), the conjecture arises that the propagating wave in the far field can be characterized by

$$s(r,t) = \frac{K}{r} e^{-j\beta(t)r} e^{j2\pi[f_o t + g(t)]} \quad (3.157)$$

where

$$\beta(t) = \frac{2\pi f(t)}{c} . \quad (3.158)$$

This conjecture can be resolved by, once again, utilizing the wave equation.

Let Equation (3.157) be substituted into Equation (3.148). Observe that

$$\frac{\partial^2 [rs(r,t)]}{\partial r^2} = -\beta^2(t) K e^{-j\beta(t)r} e^{j2\pi[f_o t + g(t)]} \quad (3.159)$$

while

$$\begin{aligned} \frac{1}{c^2} \frac{\partial^2 [rs(r,t)]}{\partial t^2} &= \left\{ -\frac{1}{c^2} \left[ -r \frac{d\beta(t)}{dt} + 2\pi f(t) \right]^2 + \frac{j}{c^2} \left[ -r \frac{d^2 \beta(t)}{dt^2} + 2\pi \frac{d^2 g(t)}{dt^2} \right] \right\} \\ &\quad K e^{-j\beta(t)r} e^{j2\pi[f_o t + g(t)]} . \end{aligned} \quad (3.160)$$

Equating Equations (3.159) and (3.160) and canceling common terms yields

$$\beta^2(t) = \frac{1}{c^2} \left[ -r \frac{d\beta(t)}{dt} + 2\pi f(t) \right]^2 + \frac{j}{c^2} \left[ r \frac{d^2 \beta(t)}{dt^2} - 2\pi \frac{d^2 g(t)}{dt^2} \right]. \quad (3.161)$$

Now assume that the modulation,  $g(t)$ , varies slowly relative to the carrier frequency,  $f_o$ , such that

$$\left| \frac{dg(t)}{dt} \right| \ll f_o. \quad (3.162)$$

Making use of Equation (3.158), observe that

$$r \frac{d\beta(t)}{dt} = 2\pi \frac{r}{c} \frac{d^2 g(t)}{dt^2} \quad (3.163)$$

and

$$r \frac{d^2 \beta(t)}{dt^2} = 2\pi \frac{r}{c} \frac{d^3 g(t)}{dt^3}. \quad (3.164)$$

On the other hand,

$$2\pi f(t) = 2\pi \left[ f_o + \frac{dg(t)}{dt} \right] \approx 2\pi f_o. \quad (3.165)$$

It is likely that

$$t_r = \frac{r}{c} \ll f_o \quad (3.166)$$

where  $t_r$  denotes the time required by the propagating wave to traverse the distance,  $r$ . Finally, assuming

$$\left| \frac{d^2 g(t)}{dt^2} \right| \ll f_o^2, \quad (3.167)$$

it is concluded that Equation (3.161) is approximately given by

$$\beta^2(t) \approx \left( \frac{2\pi f(t)}{c} \right)^2. \quad (3.168)$$

Therefore, Equation (3.158) is approximately valid and the propagating wave can be approximately modeled by Equation (3.157).

We say that the interferometer behaves in a quasi-stationary manner when Equations (3.149) and (3.3), which are strictly valid only for a sinusoidal constant frequency excitation, can, to a very good approximation, be generalized to Equations (3.157) and (3.158) for frequency modulated excitations. However, as pointed out by Equation (3.162), the modulation must vary slowly relative to the carrier frequency. It follows that the array factor, given by Equation (3.147), can be generalized to

$$F_{IFM}(\theta, \alpha, t) = \cos \left[ \frac{\beta(t)}{2} d_{IFM} \sin \theta \cos \alpha \right] \quad (3.169)$$

for frequency modulated excitations in this class. Introducing the time variant wavelength, defined by

$$\lambda(t) = \frac{c}{f(t)}, \quad (3.170)$$

the array factor can also be expressed as

$$F_{IFM}(\theta, \alpha, t) = \cos \left[ \pi \left( \frac{d_{IFM}}{\lambda(t)} \right) \sin \theta \cos \alpha \right]. \quad (3.171)$$

The time-variant array factor is investigated in the following sections for selected modulations.

### 3.4.2 The Time-Variant Array Factor for a Chirp Signal Applied to the Interferometer Elements

In this section the same chirp signal is applied to the two interferometer elements. In Section 3.4.3 an up chirp is applied to one element while a down chirp is applied to the other. Both cases are handled by the general analysis given below.

With reference to Figure 3.18, let the signals applied to the interferometer Elements at A and B be given by

$$s_A(t) = \begin{cases} V_m \cos[2\pi(f_o t + g_1(t) + g_2(t))] & -\frac{T}{2} \leq t \leq \frac{T}{2} \\ 0 & , \text{ otherwise} \end{cases} \quad (3.172)$$

and

$$s_B(t) = \begin{cases} V_m \cos[2\pi(f_o t - g_1(t) + g_2(t))] & , \quad -\frac{T}{2} \leq t \leq \frac{T}{2} \\ 0 & , \text{ otherwise} \end{cases} \quad (3.173)$$

where  $g_1(t)$  and  $g_2(t)$  are suitably chosen phase modulations such that the quasi-stationary assumptions of Section 3.4.1 are valid. In terms of complex signals  $s_A(t)$  and  $s_B(t)$  can be expressed as

$$s_A(t) = \begin{cases} \text{Re} \{ V_m e^{j2\pi f_o t} e^{j2\pi g_1(t)} e^{j2\pi g_2(t)} \} & , \quad -\frac{T}{2} \leq t \leq \frac{T}{2} \\ 0 & , \text{ otherwise} \end{cases} \quad (3.174)$$

and

$$s_B(t) = \begin{cases} \operatorname{Re} \{ V_m e^{j2\pi f_o t} e^{-j2\pi g_1(t)} e^{j2\pi g_2(t)} \} & , \quad -\frac{T}{2} \leq t \leq \frac{T}{2} \\ 0 & , \quad \text{otherwise} \end{cases} \quad (3.175)$$

By definition, the instantaneous frequency of  $s_A(t)$  and  $s_B(t)$ , respectively, is

$$f_A(t) = f_o + \frac{dg_1(t)}{dt} + \frac{dg_2(t)}{dt} \quad (3.176)$$

and

$$f_B(t) = f_o - \frac{dg_1(t)}{dt} + \frac{dg_2(t)}{dt} \quad (3.177)$$

Using the notation of Figure 3.19, and assuming quasi-stationary behavior, the total electric field at point, P, is given by  $R_e \{ E_{IFM}^{TOT} \}$  where

$$\beta_A(t) = \frac{2\pi f_A(t)}{c}, \beta_B(t) = \frac{2\pi f_B(t)}{c} \quad (3.178)$$

and

$$E_{IFM}^{TOT} = \frac{K}{r_1} F(\theta_1) e^{-j\beta_B(t)r_1} e^{j2\pi f_o t} e^{-j2\pi g_1(t)} e^{j2\pi g_2(t)} + \frac{K}{r_2} F(\theta_2) e^{-j\beta_A(t)r_2} e^{j2\pi f_o t} e^{j2\pi g_1(t)} e^{j2\pi g_2(t)} \quad (3.179)$$

With P in the far field the analysis proceeds in the same manner as in Section 3.1. Then

$$\beta_A(t)r_2 \approx \frac{2\pi}{c} \left[ f_o + \frac{dg_1(t)}{dt} + \frac{dg_2(t)}{dt} \right] (r - \Delta r) \quad (3.180)$$

while

$$\beta_B(t)r_1 \approx \frac{2\pi}{c} \left[ f_o - \frac{dg_1(t)}{dt} + \frac{dg_2(t)}{dt} \right] (r + \Delta r) \quad (3.181)$$

where  $\Delta r$  is given by Equation (3.126). In the far field, therefore, Equation (3.179) becomes

$$\begin{aligned} E_{IFM}^{TOT} &\approx \frac{K}{r} F(\theta) \left\{ e^{-j\frac{2\pi}{c} \left[ (f_o + \frac{dg_2(t)}{dt}) \Delta r - \frac{dg_1(t)}{dt} r \right]} e^{-j2\pi g_1(t)} + e^{j\frac{2\pi}{c} \left[ (f_o + \frac{dg_2(t)}{dt}) \Delta r - \frac{dg_1(t)}{dt} r \right]} e^{j2\pi g_1(t)} \right\} \\ &\quad e^{-j\frac{2\pi}{c} \left[ (f_o + \frac{dg_2(t)}{dt}) r - \frac{dg_1(t)}{dt} \Delta r \right]} e^{j2\pi g_2(t)} e^{j2\pi f_o t} \\ &= \frac{2K}{r} F(\theta) F_{IFM}(\theta, \alpha, t) e^{-j\frac{2\pi}{c} \left[ (f_o + \frac{dg_2(t)}{dt}) r - \frac{dg_1(t)}{dt} \Delta r \right]} e^{j2\pi g_2(t)} e^{j2\pi f_o t} \end{aligned} \quad (3.182)$$

where the interferometer array factor is given by

$$F_{IFM}(\theta, \alpha, t) = \cos \left\{ \frac{2\pi}{c} \left[ \left( f_o + \frac{dg_2(t)}{dt} \right) \Delta r - \frac{dg_1(t)}{dt} r \right] + 2\pi g_1(t) \right\}. \quad (3.183)$$

Finally, from Equations (3.176) and (3.177), note that

$$f_o + \frac{dg_2(t)}{dt} = \frac{f_A(t) + f_B(t)}{2} \quad (3.184)$$

while

$$\frac{dg_1(t)}{dt} = \frac{f_A(t) - f_B(t)}{2}. \quad (3.185)$$

As a result, Equations (3.182) and (3.183) can, also, be expressed as

$$E_{IFM}^{TOT} \approx \frac{2K}{r} F(\theta) F_{IFM}(\theta, \alpha, t) \quad (3.186)$$

$$e^{-j\frac{\pi}{c}[(f_A(t) + f_B(t))r - (f_A(t) - f_B(t))\Delta r]} e^{j2\pi g_2(t)} e^{j2\pi f_o t}$$

and

$$F_{IFM}(\theta, \alpha, t) = \cos \left\{ \frac{\pi}{c} [(f_A(t) + f_B(t))\Delta r - (f_A(t) - f_B(t))r] + 2\pi g_1(t) \right\}. \quad (3.187)$$

Having completed the above analysis, we now consider the case for which the same chirp signal is applied to the two interferometer elements. Let

$$g_1(t) = 0 \quad (3.188)$$

and

$$g_2(t) = \mu \frac{t^2}{2}. \quad (3.189)$$

Then, with reference to Equations (3.172) and (3.173), it follows that

$$s_A(t) = s_B(t) = \begin{cases} V_m \cos[2\pi(f_o t + \mu \frac{t^2}{2})], & -\frac{T}{2} \leq t \leq \frac{T}{2} \\ 0, & \text{otherwise} \end{cases} \quad (3.190)$$

The corresponding instantaneous frequency is

$$f_A(t) = f_B(t) = f_o + \mu t = f(t). \quad (3.191)$$

Observe that

$$f_A(t) + f_B(t) = 2(f_o + \mu t) \quad (3.192)$$

while

$$f_A(t) - f_B(t) = 0. \quad (3.193)$$

Consequently, when the same chirp signal is applied to the two interferometer elements, the expression in Equation (3.187) for the interferometer array factor becomes

$$F_{IFM}(\theta, \alpha, t) = \cos \left[ \frac{2\pi}{c} (f_o + \mu t) \Delta r \right] = \cos \left[ \frac{2\pi}{c} f(t) \Delta r \right]. \quad (3.194)$$

Making use of Equations (3.158) and (3.126), the array factor can, also, be expressed as

$$F_{IFM}(\theta, \alpha, t) = \cos \left[ \frac{\beta(t)}{2} d_{IFM} \sin \theta \cos \alpha \right]. \quad (3.195)$$

Observe that this is consistent with Equation (3.169).

As was done in Equation (3.129), it is convenient to measure the spacing of the interferometer elements in units of half wavelength. Then

$$\begin{aligned} \frac{\beta(t)}{2} d_{IFM} &= \frac{\beta(t)}{2} k_s \frac{\lambda o}{2} = \frac{2\pi f(t)}{2c} k_s \frac{\lambda o}{2} = \frac{k_s \pi \lambda o}{2c} [f_o + \Delta f(t)] \\ &= \frac{k_s \pi}{2} \left[ 1 + \frac{\Delta f(t)}{f_o} \right] \end{aligned} \quad (3.196)$$

where  $\Delta f(t)$  is the instantaneous frequency deviation given by

$$\Delta f(t) = f(t) - f_o = \mu t. \quad (3.197)$$

In addition, it is convenient to define

$$\Delta k_s(t) = \frac{k_s \Delta f(t)}{f_o} \quad (3.198)$$

which can be interpreted as the instantaneous deviation from  $k_s$ . Note that

$$\frac{\Delta f(t)}{f_o} = \frac{\Delta k_s(t)}{k_s}. \quad (3.199)$$

Hence, Equation (3.196) can, also, be written as

$$\frac{\beta(t)}{2} d_{IFM} = \frac{k_s \pi}{2} \left[ 1 + \frac{\Delta k_s(t)}{k_s} \right]. \quad (3.200)$$

It follows that alternative expressions for the interferometer array factor are

$$F_{IFM}(\theta, \alpha, t) = \cos \left\{ \frac{k_s \pi}{2} \left[ 1 + \frac{\Delta f(t)}{f_o} \right] \sin \theta \cos \alpha \right\} \quad (3.201)$$

$$= \cos \left\{ \frac{k_s \pi}{2} \left[ 1 + \frac{\Delta k_s(t)}{k_s} \right] \sin \theta \cos \alpha \right\}.$$

By way of example, consider the case for which

$$\theta = \frac{\pi}{2} \text{ and } k_s = 21. \quad (3.202)$$

At time,  $t_1$ , assume

$$\Delta f(t_1) = \Delta k_s(t_1) = 0. \quad (3.203)$$

The array factor is now given by

$$F_{IFM} \left( \frac{\pi}{2}, \alpha, t_1 \right) = \cos \left[ \frac{21\pi}{2} \cos \alpha \right]. \quad (3.204)$$

The magnitude of the array factor is plotted in Figure 3.22(a). As explained in Section 3.3, a broad null appears at  $\alpha = 0^\circ$  since  $k_s$  is an odd integer.

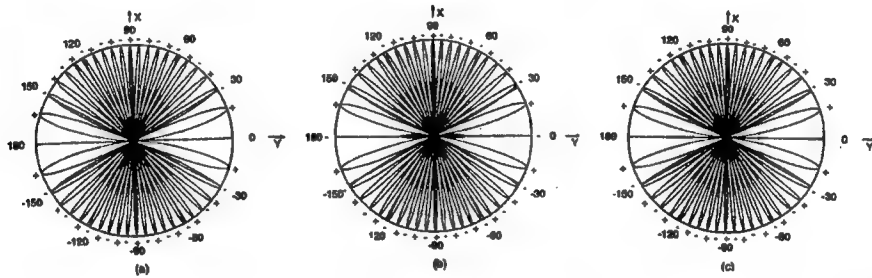


**Figure 3.22:** The azimuthal radiation pattern of the interferometer array factor, where the elements are on the y-axis, is plotted for  $\theta = \pi/2$ ,  $d_{IFM} = 21\lambda_o/2$ , and  $(\Delta f(t)/f_o)$  equal to (a) 0, (b) 0.01, and (c) 0.001.

Now assume a 1% change in the carrier frequency at time,  $t_2$ , such that

$$\frac{\Delta f(t_2)}{f_o} = \frac{\Delta k_s(t_2)}{k_s} = 0.01. \quad (3.205)$$

The corresponding array factor is

$$F_{IFM} \left( \frac{\pi}{2}, \alpha, t_2 \right) = \cos \left[ \frac{21.21\pi}{2} \cos \alpha \right]. \quad (3.206)$$

Its magnitude is plotted in Figure 3.22(b). Instead of the broad null at  $\alpha = 0^\circ$ , there is now a minor lobe peak whose magnitude is 0.324. This is only 9.8 dB down from the major lobe peak value of unity and raises concern that significant energy could be radiated in the direction of the radar main beam. Even so, as is seen from Table 3.6, there is very little steering of the major lobe positions.



For very small percentage changes in the carrier frequency it is possible to derive an approximate relation for the minor lobe peak at  $\alpha = 0^\circ$ . With  $\theta = \pi/2$ , Equation (3.201) becomes

$$F_{IFM}\left(\frac{\pi}{2}, \alpha, t\right) = \cos\left\{\frac{k_s \pi}{2} \left[1 + \frac{\Delta k_s(t)}{k_s}\right] \cos \alpha\right\}. \quad (3.207)$$

Assume that  $k_s$  is an odd integer such that a broad null appears at  $\alpha = 0^\circ$  when  $\Delta k_s(t) = 0$ . At  $\alpha = 0^\circ$

$$\left|F_{IFM}\left(\frac{\pi}{2}, 0, t\right)\right| = \left|\cos\left[\frac{k_s \pi}{2} + \Delta k_s(t) \frac{\pi}{2}\right]\right| = \left|\sin\left(\Delta k_s(t) \frac{\pi}{2}\right)\right|. \quad (3.208)$$

When

$$\left|\Delta k_s(t) \frac{\pi}{2}\right| \ll 1, \quad (3.209)$$

it follows that

$$\left|F_{IFM}\left(\frac{\pi}{2}, 0, t\right)\right| \approx \left|\Delta k_s(t) \frac{\pi}{2}\right|. \quad (3.210)$$

For our example, in which  $k_s = 21$  and there is a 1% change in the carrier frequency, Equation (3.205) yields

$$\Delta k_s(t_2) = 0.01 k_s = 0.21.$$

Using Equation (3.210), the magnitude of the minor lobe peak at  $\alpha = 0^\circ$  is approximately given by

$$\left|\Delta k_s(t) \frac{\pi}{2}\right| = 0.21 \frac{\pi}{2} = 0.33. \quad (3.211)$$

Table 3.6											
Comparison of Major Lobe Positions in First Quadrant for a 1% Change in Carrier Frequency											
$\frac{\Delta f(t)}{f_0}$	Major Lobe Positions										
	$\alpha$										
	(Degrees)										
0	17.8	31	40.4	48.2	55.2	61.6	67.6	73.4	79	84.5	90
0.01	19.4	31.9	41	48.7	55.5	61.9	67.8	73.6	79.1	84.6	90

This value is very close to the peak value of 0.324 observed in Figure 3.22 (b).

At some time instant,  $t_3$ , suppose it is desired that the minor lobe peak at  $\alpha = 0^\circ$  be 30dB down from the major lobe peak of unity. From Equation (3.210) it would be required that

$$20 \log_{10} |\Delta k_s(t_3) \frac{\pi}{2}| = -30 \text{dB} . \quad (3.212)$$

Solution of this equation results in

$$\Delta k_s(t_3) = 0.02 .$$

As before, let  $k_s = 21$ . Then Equation (3.199) gives

$$\frac{\Delta f(t_3)}{f_o} = \frac{\Delta k_s(t_3)}{k_s} = \frac{0.02}{21} \approx 0.001 . \quad (3.213)$$

This corresponds to a 0.1% change of the carrier frequency. The corresponding array factor is

$$F_{IFM} \left( \frac{\pi}{2}, \alpha, t_3 \right) = \cos \left[ \frac{21.021\pi}{2} \cos \alpha \right] . \quad (3.213)$$

Its magnitude is plotted in Figure 3.22 (c). At  $\alpha = 0^\circ$ , the value of the interferometer pattern is

$$\left| F_{IFM} \left( \frac{\pi}{2}, 0, t_3 \right) \right| = 0.03298 \quad (3.214)$$

which is 29.6 dB down from the major lobe peak value of unity. Consequently, a 0.1% change, or less, of the carrier frequency does a very good job of approximating the broad null at  $\alpha = 0^\circ$ . However, as is shown in Table 3.7, there is negligible steering of the major lobe positions.

If the broad null at  $\alpha = 0^\circ$  is to be maintained, it is concluded that a linear frequency modulated pulse, or chirp signal, is not effective for steering the interferometer. In the next section we investigate the interferometer response when an up chirp is applied to one of its elements while a down chirp is applied to the other element.

Table 3.7											
Comparison of Major Lobe Positions in First Quadrant for a 0.1% Change in Carrier Frequency											
$\frac{\Delta f(t)}{f_o}$	Major Lobe Positions										
	$\alpha$										
	(Degrees)										
0	17.8	31	40.4	48.2	55.2	61.6	67.6	73.4	79	84.5	90
0.001	17.9	31.1	40.4	48.2	55.2	61.6	67.6	73.4	79	84.5	90

### 3.4.3 The Time-Variant Array Factor for Two Different Chirp Signals Applied to the Interferometer Elements

With reference to Equations (3.172) and (3.173), let

$$g_1(t) = \mu \frac{t^2}{2} \quad (3.215)$$

and

$$g_2(t) = 0. \quad (3.216)$$

Therefore, the signals applied to the interferometer elements at A and B are

$$s_A(t) = \begin{cases} V_m \cos[2\pi(f_o t + \mu \frac{t^2}{2})], & -\frac{T}{2} \leq t \leq \frac{T}{2} \\ 0 & , \text{ otherwise} \end{cases} \quad (3.217)$$

$$s_B(t) = \begin{cases} V_m \cos[2\pi(f_o t - \mu \frac{t^2}{2})], & -\frac{T}{2} \leq t \leq \frac{T}{2} \\ 0 & , \text{ otherwise} \end{cases} \quad (3.218)$$

The corresponding instantaneous frequencies are

$$f_A(t) = f_o + \mu t \quad (3.219)$$

and

$$f_B(t) = f_o - \mu t. \quad (3.220)$$

Note that

$$f_A(t) + f_B(t) = 2f_o \quad (3.221)$$

while

$$f_A(t) - f_B(t) = 2\mu t.$$

Thus, with an up chirp applied to one of the interferometer elements and a down chirp applied to the other, the interferometer array factor of Equation (3.187) becomes

$$F_{IFM}(\theta, \alpha, t, r) = \cos \left\{ \frac{2\pi}{c} [f_o \Delta r - \mu t r] + 2\pi \mu \frac{t^2}{2} \right\}. \quad (3.222)$$

Observe that the array factor now depends upon  $r$  as well as  $\theta$ ,  $\alpha$ , and  $t$ . The dependence upon  $\theta$  and  $\alpha$  is made obvious by utilizing Equation (3.126) which yields

$$F_{IFM}(\theta, \alpha, t, r) = \cos \left\{ \frac{2\pi}{c} \left[ \frac{f_o d_{IFM}}{2} \sin \theta \cos \alpha - \mu t r \right] + 2\pi \mu \frac{t^2}{2} \right\}. \quad (3.223)$$

It is of interest to evaluate the array factor at a fixed point in space for which the coordinates are  $\theta_o, \alpha_o$ , and  $r_o$ . Making use of Equation (3.129), note that

$$\frac{2\pi}{c} \frac{f_o d_{IFM}}{2} \sin \theta_o \cos \alpha_o = \frac{k_s \pi}{c} \frac{f_o \lambda_o}{2} \sin \theta_o \cos \alpha_o = \frac{k_s \pi}{2} \sin \theta_o \cos \alpha_o = \phi_{AF} \quad (3.224)$$

where  $\phi_{AF}$  is a constant. From Equations (3.219) and (3.220) the maximum frequency deviation of the up and down chirp signals is

$$f_D = f_A \left( \frac{T}{2} \right) - f_A \left( -\frac{T}{2} \right) = f_B \left( -\frac{T}{2} \right) - f_B \left( \frac{T}{2} \right) = f_o + \frac{\mu T}{2} - f_o + \frac{\mu T}{2} = \mu T. \quad (3.225)$$

Hence,

$$\mu = \frac{f_D}{T}. \quad (3.226)$$

It follows that

$$\frac{2\pi}{c} \mu r_o = \frac{2\pi}{c} \frac{f_D}{T} r_o = 2\pi f_{AF}. \quad (3.227)$$

Consequently, at the point in space for which the coordinates are  $\theta_o, \alpha_o$ , and  $r_o$ , the interferometer array factor can be written as

$$F_{IFM}(\theta_o, \alpha_o, t, r_o) = \cos \left[ 2\pi f_{AF} t - 2\pi \mu \frac{t^2}{2} - \phi_{AF} \right] \quad (3.228)$$

where  $f_{AF}$  and  $\phi_{AF}$  are array factor constants dependent upon position. Thus, at any point in the far field, the array factor is a linear frequency modulated pulse whose carrier frequency and phase are determined by position.

From Equation (3.182) the total complex electric field at a point in the far field is given by

$$E_{IFM}^{TOT} \approx \frac{2K}{r} F(\theta) F_{IFM}(\theta, \alpha, t, r) e^{-j \frac{2\pi}{c} [f_o r - \mu t \Delta r]} e^{j 2\pi f_o t}. \quad (3.229)$$

Therefore, the total real electric field is

$$\begin{aligned} \text{Re} \{ E_{IFM}^{TOT} \} &\approx \frac{2K}{r} F(\theta) F_{IFM}(\theta, \alpha, t, r) \\ &\cos \left\{ 2\pi \left[ \left( f_o + \frac{\mu \Delta r}{c} \right) t - \frac{f_o r}{c} \right] \right\}. \end{aligned} \quad (3.230)$$

As before, consider a point whose coordinates are  $\theta_o, \alpha_o$ , and  $r_o$ . Following the previous development, note that

$$\begin{aligned}
\frac{\mu \Delta r}{c} &= \frac{1}{c} \frac{f_D}{T} \frac{d_{IFM}}{2} \sin \theta_o \cos \alpha_o \\
&= \frac{1}{\lambda_o f_o} \frac{f_D}{T} \frac{k_s \lambda_o}{4} \sin \theta_o \cos \alpha_o \\
&= \frac{k_s}{4} \frac{f_D}{f_o} \frac{1}{T} \sin \theta_o \cos \alpha_o = f_{CA}
\end{aligned} \tag{3.231}$$

is a carrier offset frequency. In addition, define the carrier phase to be

$$\phi_{CA} = 2\pi \frac{f_o r_o}{c} \tag{3.232}$$

The total real electric field at the point whose coordinates are  $\theta_o, \alpha_o$ , and  $r_o$  is then given by

$$\begin{aligned}
\text{Re}\{E_{IFM}^{TOT}\} &\approx \frac{2K}{r_o} F(\theta_o) F_{IFM}(\theta_o, \alpha_o, t, r_o) \\
&\cos[2\pi(f_o + f_{CA})t - \phi_{CA}]
\end{aligned} \tag{3.233}$$

where  $f_{CA}$  and  $\phi_{CA}$  are carrier constants dependent upon position.

The substitution of Equation (3.228) into Equation (3.233) results in

$$\begin{aligned}
\text{Re}\{E_{IFM}^{TOT}\} &\approx \frac{2K}{r_o} F(\theta_o) \cos\left[2\pi f_{AF} t - 2\pi \mu \frac{t^2}{2} - \phi_{AF}\right] \\
&\cos[2\pi(f_o + f_{CA})t - \phi_{CA}].
\end{aligned} \tag{3.234}$$

This is recognized as a double side band suppressed carrier amplitude modulated signal where the amplitude modulation is a linear frequency modulated waveform whose instantaneous frequency decreases during the chirp. It is interesting to note that the carrier is a constant frequency sinusoid even though an up chirp and down chirp were applied at the interferometer elements. At  $t = 0$  the electric field is given by

$$\text{Re}\{E_{IFM}^{TOT}\}|_{t=0} \approx \frac{2K}{r_o} F(\theta_o) \cos(-\phi_{AF}) \cos(-\phi_{CA}). \tag{3.235}$$

This can be a small value at various points in the far field. A typical sketch of the electric field is shown in Figure 3.23, assuming  $f_{AF}$  to be much smaller than  $(f_o + f_{CA})$ .

Although  $f_{AF}$ ,  $\phi_{AF}$ ,  $f_{CA}$  and  $\phi_{CA}$  change with position, the basic waveform for the electric field is unchanged. Consequently, steering the interferometer with up and down chirps applied to the interferometer elements has little meaning even though the array factor is a function of both time and the observation point in the far field. In addition, the waveform sketched in Figure 3.23, is not a good choice for masking the direct path signal from the main radar.

It is shown in Section 3.4.4 that a frequency-hopped waveform is capable of maintaining the broad null while steering the interferometer and degrading performance of the non-cooperative bistatic radar.

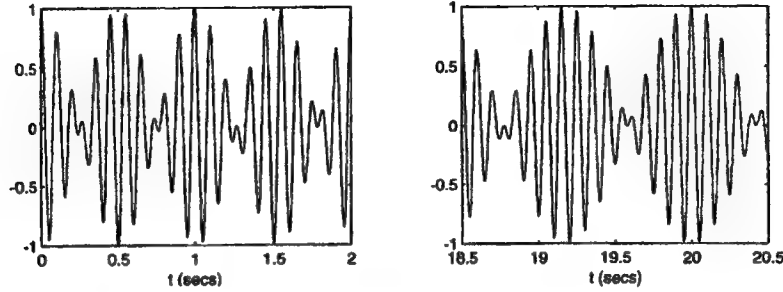


**Figure 3.23:** When up and down chirps are applied to the two interferometer elements, the electric field at a fixed point in the far field is a suppressed carrier amplitude modulated signal whose modulation is a linear frequency modulated waveform, as sketched in the figure.

#### 3.4.4 The Time-Variant Array Factor for a Frequency-Hopped Signal Applied to the Interferometer Elements

It is intended that the interferometer signal be used to 1) mask over many directions the direct path signal of the main radar and 2) communicate separate information to various receivers located at different angles. In addition, the interferometer signal should not interfere with the mission of the main radar. In order to maintain spatial orthogonality between the interferometer and main radar, it is desirable that the broad null at  $\alpha = 0^\circ$  be preserved while the interferometer is steered in different directions. These objectives can be met, as shown in this section, by using a frequency-hopped signal to drive the two elements of the interferometer.

Let both elements of the interferometer, assumed to be positioned on the y-axis, be driven by

$$s_{IFM}(t) = \sum_{i=0}^{\infty} v_i(t - iT_s) \quad (3.236)$$

where

$$v_i(t) = \begin{cases} V_m \cos[2\pi(f_o + f_{oi})t], & 0 \leq t \leq T_s \\ 0, & \text{otherwise} \end{cases} \quad (3.237)$$

Consequently, during the  $i^{\text{th}}$  interval, given by

$$iT_s \leq t \leq (i+1)T_s, \quad (3.238)$$

the interferometer signal is a constant frequency sinusoid with frequency,  $(f_o + f_{oi})$ .

Following the quasi-stationary development in Section 3.4.2, the interferometer array factor can be expressed as

$$F_{IFM}(\theta, \alpha, t) = \cos\left[\frac{\beta(t)}{2} d_{IFM} \sin \theta \cos \alpha\right] \quad (3.195)$$

where

$$\beta(t) = \frac{2\pi f(t)}{c}. \quad (3.158)$$

During the  $i^{\text{th}}$  interval

$$\beta(t) = \frac{2\pi(f_o + f_{oi})}{c}, \quad iT_s \leq t \leq (i+1)T_s. \quad (3.239)$$

As in Section 3.3.3, let the spacing between the interferometer elements be

$$d_{IFM} = k_s \frac{\lambda_o}{2}. \quad (3.129)$$

Then

$$\frac{\beta(t)d_{IFM}}{2} = \frac{k_s \pi \lambda_o}{2c} [f_o + f_{oi}] = \frac{k_s \pi}{2} \left[ 1 + \frac{f_{oi}}{f_o} \right] \quad (3.240)$$

where use was made of the fact that

$$c = \lambda_o f_o. \quad (3.152)$$

Now define

$$\Delta k_i = \frac{k_s f_{oi}}{f_o}. \quad (3.241)$$

Note that

$$\frac{f_{oi}}{f_o} = \frac{\Delta k_i}{k_s}. \quad (3.242)$$

Hence, Equation (3.240) can be written as

$$\frac{\beta(t)d_{IFM}}{2} = \frac{k_s \pi}{2} \left[ 1 + \frac{\Delta k_i}{k_s} \right] = (k_s + \Delta k_i) \frac{\pi}{2}. \quad (3.243)$$

Substitution of Equation (3.243) into Equation (3.195) yields

$$F_{IFM}(\theta, \alpha, t) = \cos \left[ (k_s + \Delta k_i) \frac{\pi}{2} \sin \theta \cos \alpha \right]. \quad (3.244)$$

When  $\theta = \pi/2$ , the horizontal radiation pattern becomes

$$F_{IFM}\left(\frac{\pi}{2}, \alpha, t\right) = \cos \left[ (k_s + \Delta k_i) \frac{\pi}{2} \cos \alpha \right]. \quad (3.245)$$

A broad null exists at  $\alpha = 0^\circ$  provided  $(k_s + \Delta k_i)$  is an odd integer. To maintain a broad null at  $f_o$  (i.e., when  $\Delta k_i = 0$ ), let  $k_s$ , also, be an odd integer. The broad null is then preserved by requiring that  $\Delta k_i$  be plus or minus an even integer. For specified values of  $\Delta k_i, k_s$  and  $f_o, f_{oi}$  is determined from Equation (3.242) according to

$$f_{oi} = \frac{\Delta k_i}{k_s} f_o. \quad (3.246)$$

In this way, a broad null always exists at  $\alpha = 0^\circ$  even though the frequency changes from one interval to the next.

The interferometer pattern of Equation (3.245) can be steered in various directions through the appropriate choice of  $\Delta k_i$  and, therefore,  $f_{oi}$ . In general, when  $(k_s + \Delta k_i)$  is an odd integer, there are  $(k_s + \Delta k_i - 1)$  major lobes completely contained in the upper half of the interferometer pattern centered at  $\alpha = 0^\circ$ ,  $(k_s + \Delta k_i - 1)$  major lobes completely contained in the lower half of the interferometer pattern centered at  $\alpha = \pm 180^\circ$ , and two major lobes centered at  $\alpha = \pm 90^\circ$ . Thus, the number of major lobes changes with a change in  $\Delta k_i$ . This can be utilized to direct the interferometer signal towards a specified direction during the  $i^{\text{th}}$  interval.

To illustrate the steering of the interferometer by means of a frequency-hopped signal, while maintaining the broad null at  $\alpha = 0^\circ$ , radiation patterns are presented in Figure 3.24 for  $k_s = 21$  and  $\Delta k_i = 0$  and  $\pm 2$ . Note that this involves the smallest allowable values for  $|\Delta k_i|$ . Of course, greater differences between the patterns will result for larger values of  $|\Delta k_i|$ .

As expected, a broad null exists at  $\alpha = 0^\circ$  for all three cases presented in Figure 3.24. Observe that there are 18, 20, and 22 major lobes, respectively, in the upper half of the patterns shown in Figure 3.24 (a), (b), and (c). Also, each pattern contains two major lobes centered at  $\alpha = \pm 90^\circ$ .

Positions of the major lobes, indicated by x's, and nulls, indicated by o's, are shown in Figure 3.25 for the three patterns plotted in Figure 3.24. The polarities of the major lobes are indicated by + and - signs placed over the x's.

Comparison of the major lobe positions in Figure 3.24 (a) with those in Figure 3.24 (b) reveals that the major lobes in the two figures are separated by a minimum of  $1^\circ$  for  $20^\circ \leq \alpha \leq 80^\circ$ . A similar conclusion arises when the major lobe positions in Figure 3.24 (b) are compared with those in Figure 3.24 (c). Making the same comparisons with regard to the nulls, it is seen that they are, also, separated by a minimum of  $1^\circ$  for  $20^\circ \leq \alpha \leq 80^\circ$ . Consequently, significant separations exist even though  $(k_s + \Delta k_i)$  differs by the minimum allowable value.



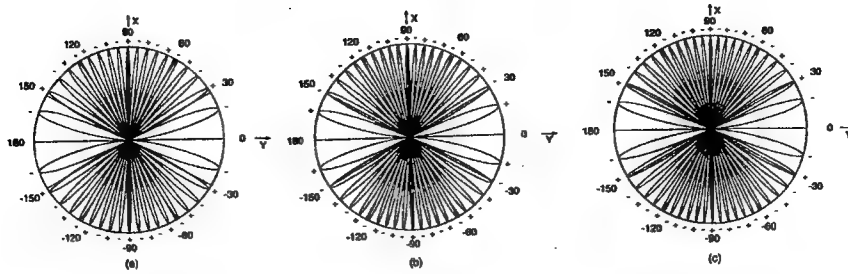


Figure 3.24: The azimuthal radiation pattern of the interferometer array factor is plotted for a frequency-hopped excitation with  $\theta = \pi/2$ ,  $k_s = 21$ , and  $\Delta k_i$  equal to (a) -2, (b) 0, and (c) +2.

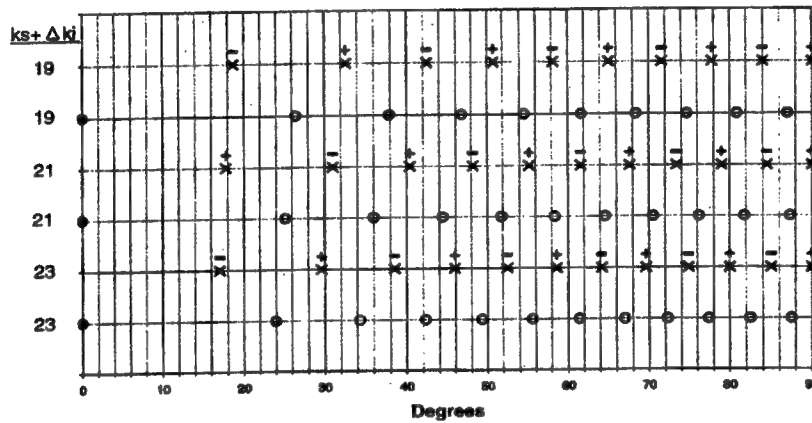


Figure 3.25: Positions of the major lobes, indicated by x's, and nulls, indicated by o's, are shown for the three patterns plotted in Figure 3.24.

However, even though the difference in  $(k_s + \Delta k_i)$  is twice as large when comparing the pattern of Figure 3.24 (a) with that of Figure 3.24 (c), observe for  $54^\circ \leq \alpha \leq 66^\circ$  that some separations between major lobe positions and null positions are less than  $1^\circ$ . Consequently, making the difference in  $(k_s + \Delta k_i)$  larger does not guarantee large separations relative to neighboring major lobe and/or neighboring null positions. It should be noted that some of the closely spaced major lobes, when comparing Figure 3.24 (a) to 3.24 (c), are of opposite polarity. The reversal in sign could help to thwart the non-cooperative radar in its attempt to obtain a high quality reference from the direct path signal.

Nevertheless, this example indicates that it should be possible to select suitable values for  $k_s$  and  $\Delta k_i$  such that the interferometer is steered in desired directions while maintaining the broad null at  $\alpha = 0^\circ$ .

## CHAPTER 4

### A RADAR WAVEFORM EMPLOYING FREQUENCY DIVERSITY

#### 4.1 Frequency-Hopped Waveforms [7], [8]

Frequency-hopped waveforms are a subclass of frequency-coded signals. In particular, consider the radar pulse waveform of duration  $NT$  which consists of  $N$  contiguous different frequency bursts, each of duration  $T$ . Assume the hopping frequencies are appropriately selected from a set of  $N$  frequencies equally spaced according to  $(f_c + f_n)$  where

$$f_n = \frac{n}{T} ; n = 0, 1, \dots, (N-1) . \quad (4.1)$$

The spacing is given by

$$\Delta f = (f_c + f_{n+1}) - (f_c + f_n) = \frac{n+1}{T} - \frac{n}{T} = \frac{1}{T} ; n = 0, 1, \dots, (N-1) . \quad (4.2)$$

A linear stepped-frequency pulse results when the frequencies are chosen consecutively such that the  $n^{\text{th}}$  frequency burst has the frequency  $(f_c + f_n)$ , where  $f_n$  is given by Equation (4.1). On the other hand, the frequencies can, also, be scrambled. For this purpose, consider an arbitrary ordering of the  $N$  integers contained between 0 and  $(N-1)$ . Note that there are  $N!$  such orderings. Let a particular sequence of ordered integers be represented by the set

$$\{\theta_n\} = \{\theta_0, \theta_1, \theta_2, \dots, \theta_{N-1}\} . \quad (4.3)$$

Now let the subscript,  $n$ , indicate the ordering of the frequency bursts contained within the radar pulse. The frequency of the  $n^{\text{th}}$  burst is then chosen to be

$$f_c + f_n = f_c + \frac{\theta_n}{T} ; n = 0, 1, \dots, (N-1) . \quad (4.4)$$

The resulting waveform is referred to as a scrambled-frequency pulse. Because  $\{\theta_n\}$  contains each integer between 0 and  $(N-1)$  only once, the frequencies of the  $N$  bursts within the radar pulse are each different.

Analytically, the frequency-hopped pulse can be expressed as

$$s(t) = \sum_{n=0}^{N-1} s_n(t - nT) \quad (4.5)$$

where

$$s_n(t) = \begin{cases} A \cos[2\pi(f_c + f_n)t] , & 0 \leq t \leq T \\ 0 & \text{otherwise} \end{cases} . \quad (4.6)$$

The envelope of this waveform is illustrated in Figure 4.1 for both a linear stepped-frequency pulse and a scrambled-frequency pulse. When the frequencies are chosen consecutively, the linear stepped-frequency pulse is a discrete approximation to the linear frequency modulated pulse or chirp waveform. The bandwidth of the frequency-hopped pulse is  $N\Delta f$ , where  $\Delta f$  is given by Equation (4.2), and is assumed to be much less than the carrier frequency,  $f_c$ .

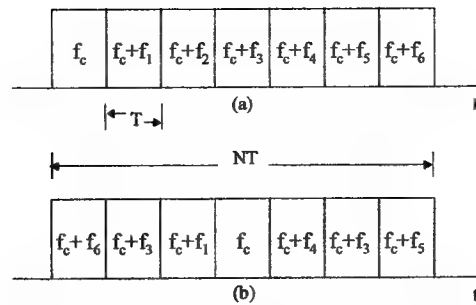


**Figure 4.1:** The frequencies of a frequency-hopped pulse may be either (a) consecutive or (b) scrambled.

Many factors favor the use of frequency-hopped waveforms for the pulsed radar signal. These are briefly discussed below:

- 1) By appropriate ordering of the frequencies, it is possible to eliminate the range-Doppler ambiguity of the linear frequency modulated or chirp waveform. It is shown in the following sections that a thumbtack approximation to the ambiguity function is possible.
- 2) For a specified value of  $N$  there are multiple orderings of the frequencies that result in a thumbtack shaped ambiguity function. Coherent reference denial is enhanced by changing the frequency scrambling from one radar pulse to the next. This prevents the non-cooperative bistatic radar from relying on the integration of a single radar waveform estimate over the coherent processing interval. In addition, the non-cooperative radar is forced to repeatedly estimate a new radar waveform from each pulse received in the direct path.
- 3) Another benefit from modifying the frequency ordering from one radar pulse to the next is that the main radar is likely to be less susceptible to interfering FM signals and repeater jammers.
- 4) When the radar pulse consists of  $N$  frequency bursts, the receiver can be channelized with  $N$  channels where each channel is tuned to a unique frequency and has a bandwidth equal to  $\Delta f$ . This bandwidth is  $1/N$  times the total signal processing bandwidth. Therefore, extremely high time-bandwidth products can be achieved utilizing receiver components that have instantaneous narrow-band characteristics.
- 5) Channelization allows the capability for selective limiting. In a conventional FM receiver using a single limiter, strong CW interference anywhere in the total signal bandwidth is likely to capture the FM receiver. As a result, the target return signals are suppressed and unlikely to be detected with a preset threshold crossing. In a channelized system, CW interference suppresses target returns in only one of the channels. Hence, the target signal power is reduced only by a factor of  $[(N-1)/N]^2$ . If  $N$  is greater than 10, CW interference can be 20 to 30 dB above the per-channel target signal power without preventing target detection in a fixed-threshold system.
- 6) Modern technology, employing phase-locked voltage controlled oscillators and digital frequency synthesizers, allows for the generation of sophisticated stepped frequency waveforms. In fact, specialized stepped-frequency systems have been developed that achieve up to 10 GHz of bandwidth and very large time-bandwidth products.

#### 4.2 The Permutation Matrix [7]

Frequency-hopped waveforms are conveniently represented by an  $N \times N$  matrix, denoted by  $A$ , for which the  $N$  rows correspond to the  $N$  frequencies and the  $N$  columns correspond to the  $N$  time intervals during which a burst occurs. The entry in the  $i^{\text{th}}$  row and  $j^{\text{th}}$  column, designated by  $a_{ij}$ , is set equal to unity if and only if frequency,  $f_c + f_i$ , is transmitted in the time interval  $t_j$  where  $i, j = 0, 1, \dots, (N-1)$ . Otherwise,  $a_{ij}$  is set equal to zero. The matrix,  $A$ , is known as the permutation matrix. Because the elements of  $A$  take one of two possible values,  $A$  is, also, called a binary matrix.

The binary matrix for a quantized linear FM signal is shown in Figure 4.2. For this case,  $N=7$ . A dot in the  $ij^{\text{th}}$  block indicates  $a_{ij}=1$  whereas a blank indicates  $a_{ij}=0$ . Note that there is only one dot per column and per row. This is consistent with the requirement at any given time slot that only one frequency is transmitted and each frequency is transmitted only once.

$f_c+f_6$							*
$f_c+f_5$						*	
$f_c+f_4$					*		
$f_c+f_3$				*			
$f_c+f_2$			*				
$f_c+f_1$		*					
$f_c$	*						
$f/t$	$t_0$	$t_1$	$t_2$	$t_3$	$t_4$	$t_5$	$t_6$

**Figure 4.2:** Permutation matrix for a stepped frequency linear FM waveform has nonzero entries only along one of the diagonals.

An  $N \times N$  matrix contains a total of  $Q=N^2$  matrix elements. Thus, when the elements are binary, the number of different matrices possible is  $2^Q$ . However, of these only  $N!$  matrices can be obtained by permuting the  $N$  integers contained between 0 and  $(N-1)$ . It is for this reason that  $A$  is referred to as a permutation matrix. Some of these are better than others for designing the signal pattern of a radar waveform.

When a frequency-hopped signal is reflected from a target and received by an observer, it is shifted in time depending upon the range to the target and in frequency depending upon the radial velocity of the target. The amounts of these shifts are determined by comparing shifts in both time and frequency of a replica of the transmitted waveform with the actual received signal and noting for which combination of time and frequency shifts the coincidence is greatest. This may be thought of as counting the number of coincidences between 1's in the permutation matrix  $A$  with 1's in a shifted version of  $A$  for which all entries have been shifted  $r$  units to the right ( $r$  is negative if there is a shift to the left) and  $s$  units upward ( $s$  is negative if there is a shift downward). Let the shifted permutation matrix be denoted by  $A(r,s)$ .

The number of such coincidences,  $C(r,s)$ , is the unnormalized autocorrelation between  $A$  and  $A(r,s)$ .  $C(r,s)$  clearly satisfies the following conditions:

$$C(0,0) = N \quad (4.7)$$

$$0 \leq C(r,s) < N ; \quad r \neq 0 \text{ and } s \neq 0 \quad (4.8)$$

In addition, because time and frequency are restricted to the intervals  $t_0 \leq t \leq t_{(N-1)}$  and  $f_c \leq f \leq f_c + f_{(N-1)}$ , it follows that

$$C(r,s) = 0 ; \quad |r| \geq N \text{ and/or } |s| \geq N \quad (4.9)$$

The two-dimensional autocorrelation function,  $C(r,s)$ , is called the ambiguity function and can be thought of as the total coincidence between the actual returning signal and the transmitted signal shifted by  $r$  units in time and  $s$  units in frequency. It is useful to think of the permutation matrix,  $A$ , as a two-dimensional template of  $N^2$  cells which is opaque at the  $(N^2-N)$  cells where  $a_{ij}=0$  and transparent at the  $N$  cells where  $a_{ij}=1$ . The total signal energy emerging through the  $N$  transparent windows is summed to give the value of  $C(r,s)$  when the template is shifted  $r$  units on the time axis and  $s$  units on the frequency axis.

For example, with regard to the permutation matrix shown in Figure 4.2,  $C(0,0) = 7$ ,  $C(1,1) = 6$ ,  $C(2,2) = 5$ ,  $C(3,3) = 4$ ,  $C(4,4) = 3$ ,  $C(5,5) = 2$ ,  $C(6,6) = 1$  and  $C(r,s) = 0$  for all other choices of  $r$  and  $s$ . This yields the well known diagonal ridge associated with the linear stepped FM signal. In the real world the returning signal is always noisy. For large values of  $N$  and a very noisy environment, this signal pattern would be likely to produce spurious targets in addition to the ambiguities caused by the ridge.

For radar applications it is desirable to have an ambiguity function that approaches the ideal thumbtack. In this context a good frequency hopping pattern should result in small values for  $C(r,s)$  when  $(r,s) \neq (0,0)$ . Such patterns have been proposed by John Costas [9] and are discussed in the next section.

### 4.3 Costas Arrays [9], [10]

John P. Costas attempted to find those  $N \times N$  permutation matrices for which

$$\max_{(r,s) \neq (0,0)} C(r,s) = 1 \quad . \quad (4.10)$$

Such matrices are known as Costas arrays. In addition to radar, the frequency hop patterns associated with Costas arrays may be useful in other applications, such as spread spectrum communication systems, where the objective may be to achieve either jamming resistance, low probability of intercept, or frequency diversity for a selectively fading channel.

The problem of constructing Costas arrays can be described as: Place  $N$  1's in an otherwise null  $N$  by  $N$  matrix such that each row contains a single 1 as does each column. Make the placement such that for all possible  $(r,s)$  shift combinations of the resulting permutation matrix relative to itself, at most one pair of 1's will coincide.

Let  $M(N)$  denote the number of Costas arrays that can be generated from the  $N!$  ( $N \times N$ ) matrices obtained by permuting the  $N$  integers contained between 0 and  $N-1$ . The density of Costas arrays is defined to be  $M(N)/N!$ . These values are tabulated in Table 4.1 for  $3 \leq N \leq 12$ . Although the number of Costas arrays increases with  $N$ , the density decreases significantly. Thus, a random search by means of a computer program can be rather lengthy.

An example of a Costas array for  $N=7$  is shown in Figure 4.3. This array corresponds to the particular sequence of ordered integers given by

$$\{\theta_n\} = \{3, 6, 0, 5, 4, 1, 2\} \quad . \quad (4.11)$$

The corresponding ambiguity matrix is shown in Figure 4.4 where the time shift,  $r$ , and the frequency shift,  $s$ , both extend over the integers in the range from  $-6$  to  $+6$ . A block of the ambiguity matrix is left blank when  $C(r,s)=0$ . Note that  $C(0,0)=7$  and that the nonzero values of  $C(r,s)$  are equal to unity.

TABLE 4.1  
NUMBER AND DENSITY OF COSTAS ARRAYS

N	3	4	5	6	7	8	9	10	11	12
M(N)	4	12	40	116	200	444	760	2,160	4,368	7,852
M(N)/N!	0.67	0.5	0.33	0.16	0.04	0.011	$2 \times 10^{-3}$	$6 \times 10^{-4}$	$1 \times 10^{-4}$	$1.6 \times 10^{-5}$

$f_c + f_6$		*					
$f_c + f_5$				*			
$f_c + f_4$					*		
$f_c + f_3$	*						
$f_c + f_2$							*
$f_c + f_1$						*	
$f_c$			*				
$f/t$	$t_0$	$t_1$	$t_2$	$t_3$	$t_4$	$t_5$	$t_6$

Figure 4.3: The permutation matrix shown is one of 200 possible Costas arrays for  $N=7$ .

The ambiguity matrix is readily constructed from the difference triangle associated with the sequence,  $\{\theta_n\}$ . By definition, the element in the  $i^{\text{th}}$  row and  $j^{\text{th}}$  column of the difference triangle is determined by

$$d_{i,j} = \theta_{(i+j-1)} - \theta_{(j-1)} \quad (4.12)$$

where  $(i+j) \leq N$ .

For example, consider the sequence in Equation (4.11) which generates the Costas array in Figure 4.3. The difference triangle is formed by successively considering  $i=1,2,3,4,5,6$  and, for each  $i$ , letting  $j$  assume all values such that  $(i+j) \leq 7$ . Hence, for  $i=1$  and  $j=1,2,3,4,5,6$ , we obtain

6						1							
5			1					1					
4		1			1				1				
3				1	1	1		1					
2		1		1	1					1	1		
1	1				1	1		1		1	1		
0							7						
-1			1	1		1		1	1				1
-2			1	1					1	1		1	
-3						1		1	1	1			
-4					1				1			1	
-5						1					1		
-6								1					
s/r	-6	-5	-4	-3	-2	-1	0	1	2	3	4	5	6

Figure 4.4: The ambiguity matrix is shown for the Costas array of Figure 4.3.

$$\begin{aligned}
d_{1,1} &= \theta_1 - \theta_0 = 6 - 3 = 3 \\
d_{1,2} &= \theta_2 - \theta_1 = 0 - 6 = -6 \\
d_{1,3} &= \theta_3 - \theta_2 = 5 - 0 = 5 \\
d_{1,4} &= \theta_4 - \theta_3 = 4 - 5 = -1 \\
d_{1,5} &= \theta_5 - \theta_4 = 1 - 4 = -3 \\
d_{1,6} &= \theta_6 - \theta_5 = 2 - 1 = 1
\end{aligned} \tag{4.13}$$

Similarly, for  $i=2$  and  $j=1,2,3,4,5$ , there results

$$\begin{aligned}
d_{2,1} &= \theta_2 - \theta_0 = 0 - 3 = -3 \\
d_{2,2} &= \theta_3 - \theta_1 = 5 - 6 = -1 \\
d_{2,3} &= \theta_4 - \theta_2 = 4 - 0 = 4 \\
d_{2,4} &= \theta_5 - \theta_3 = 1 - 5 = -4 \\
d_{2,5} &= \theta_6 - \theta_4 = 2 - 4 = -2
\end{aligned} \tag{4.14}$$

The complete difference triangle is shown in Figure 4.5.

It can be shown that  $\{\theta_n\}$  yields a Costas array if and only if the difference triangle formed from  $\{\theta_n\}$  has no repeated terms in any row. The ambiguity matrix is constructed by recognizing that  $d_{i,j}=k$  indicates that a 1 is to be placed in the block of the ambiguity matrix corresponding to  $r=i$  and  $s=k$ . For example,  $d_{4,2} = -5$  implies that a 1 belongs in the matrix corresponding to  $r=4$  and  $s=-5$ . The matrix is completed by recognizing that

$$C(r, s) = C(-r, -s) \tag{4.15}$$

The number of entries in the difference triangle is  $(N-1)N/2$ . Utilizing Equation (4.15), it follows that there are  $(N-1)N$  1's in the ambiguity matrix.

$$\{\theta_n\} = \{3, 6, 0, 5, 4, 1, 2\}$$

$i \backslash j$	1	2	3	4	5	6
1	3	-6	5	-1	-3	1
2	-3	-1	4	-4	-2	
3	2	-2	1	-3		
4	1	-5	2			
5	-2	-4				
6	-1					

Figure 4.5: This difference triangle can be used to construct the ambiguity matrix presented in Figure 4.4.

The ambiguity matrix provides a first-order approximation to the actual ambiguity function because it does not account for fractional shifts. A detailed evaluation of the actual ambiguity function for the frequency-hopped signal is likely to reveal many more minor peaks and a few peaks whose values are larger than unity.

The frequency-hopped signal generated from a Costas array is referred to as a Costas signal. A three-dimensional view of the ambiguity function for the Costas signal generated from the Costas array of Figure 4.3 is shown in Figure 4.6. The cut along the time shift axis for zero frequency shift is shown in Figure 4.7. Observe that the peak value of the ambiguity function has been normalized to unity.

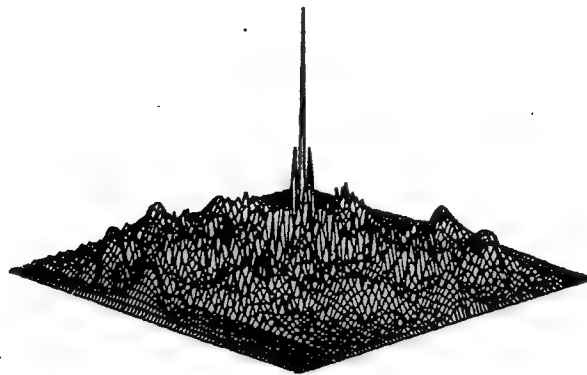


**Figure 4.6:** The ambiguity function of the Costas signal generated from the Costas array of Figure 4.3 approximates the shape of a thumbtack.

The plot in Figure 4.6 shows a few peaks reaching a value of  $0.29 \approx 2/7$ . However, most peaks reach the expected level of  $0.143 = 1/7$ . The ambiguity matrix does not predict any minor peaks along the time shift axis for zero frequency shift. Nevertheless, many minor peaks, most of which are less than or equal to 0.1, are revealed in Figure 4.7.

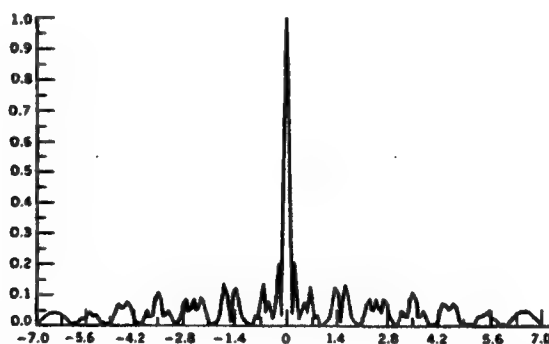


**Figure 4.7:** The ambiguity matrix does not predict the minor peaks along the time shift axis for zero frequency shift.

In summary, the Costas array generates a Costas signal whose ambiguity function approaches the shape of the ideal thumbtack. The ratio between the main lobe and the pedestal is approximately  $N$ . However, the pedestal is not smooth. The ambiguity function has a few peaks higher than predicted by the ambiguity matrix and many dips occur at various locations within the pedestal. The pedestal stretches from the origin as far as  $\pm NT$  in time shift and, essentially, as far as  $\pm N/T$  in frequency shift. The number of major sidelobe peaks predicted from the ambiguity matrix is equal to  $(N-1)N$ . There are approximately three times as many blanks than 1's in the ambiguity matrix.



#### 4.4 Ambiguity Function of the Costas Signal [9]

Without loss of generality, frequency-hopped waveforms can be analyzed in terms of baseband signals by considering their complex envelopes. The complex envelope of the frequency-hopped signal, described by Equations (4.5) and (4.6) and normalized to have unit energy, is given by

$$f_{\text{RAD}}(t) = \frac{1}{A\sqrt{NT}} \sum_{n=0}^{N-1} p_n(t-nT) \quad (4.16)$$

where

$$p_n(t) = \begin{cases} A e^{j2\pi f_n t}, & 0 \leq t \leq T \\ 0, & \text{otherwise} \end{cases} \quad (4.17)$$

By definition, the energy of  $f_{\text{RAD}}(t)$  is

$$\begin{aligned} \int_0^{NT} |f_{\text{RAD}}(t)|^2 dt &= \int_0^{NT} f_{\text{RAD}}(t) f_{\text{RAD}}^*(t) dt \\ &= \frac{1}{A^2 NT} \int_0^{NT} \sum_{n=0}^{N-1} p_n(t-nT) \sum_{m=0}^{N-1} p_m^*(t-mT) dt \\ &= \frac{1}{A^2 NT} \int_0^{NT} \left\{ \sum_{n=0}^{N-1} |p_n(t-nT)|^2 \right\} dt \\ &\quad + \frac{1}{A^2 NT} \int_0^{NT} \left\{ \sum_{n=0}^{N-1} \sum_{m=0, m \neq n}^{N-1} p_n(t-nT) p_m^*(t-mT) \right\} dt \end{aligned} \quad (4.18)$$

Note that

$$|p_n(t-nT)|^2 = \begin{cases} A^2, & nT \leq t \leq (n+1)T \\ 0, & \text{otherwise} \end{cases} \quad (4.19)$$

Also, because the frequency bursts do not overlap when  $n \neq m$ ,

$$p_n(t-nT) p_m^*(t-mT) = 0, \quad n \neq m. \quad (4.20)$$

It follows that

$$\int_0^{NT} |f_{\text{RAD}}(t)|^2 dt = 1. \quad (4.21)$$

Therefore,  $f_{\text{RAD}}(t)$  has been normalized to have unit energy.

The delay-Doppler ambiguity function was defined in Equation (2.50) to be

$$\chi(\tau, \nu) = \int_0^{NT} f_{\text{RAD}}^*(\sigma) f_{\text{RAD}}(\sigma - \tau) e^{j2\pi \nu \sigma} d\sigma \quad (2.50)$$

where the infinite limits of integration were truncated because of the finite extent of  $f_{RAD}(t)$ . The normalized ambiguity function is known to have the following properties:

$$|\chi(\tau, v)| \leq 1 = |\chi(0, 0)|, \quad (4.22)$$

$$|\chi(-\tau, -v)| = |\chi(\tau, v)|, \quad (4.23)$$

$$\int_{-\infty}^{\infty} \int_{-\infty}^{\infty} |\chi(\tau, v)|^2 d\tau dv = 1. \quad (4.24)$$

Because of the odd symmetry, indicated by Equation (4.23), it is necessary to consider only nonnegative values of  $\tau$  and  $v$ .

Substitution of Equation (4.16) into the expression for the ambiguity function results in

$$\chi(\tau, v) = \frac{1}{A^2 NT} \int_{-\infty}^{\infty} \sum_{n=0}^{N-1} \sum_{m=0}^{N-1} p_n^*(\sigma - nT) p_m(\sigma - \tau - mT) e^{j2\pi v \sigma} d\sigma. \quad (4.25)$$

Separating the terms in the double summation into those for which  $n=m$  and those for which  $n \neq m$ , we obtain

$$\begin{aligned} \chi(\tau, v) &= \frac{1}{A^2 NT} \int_{-\infty}^{\infty} \sum_{n=0}^{N-1} p_n^*(\sigma - nT) p_n(\sigma - \tau - nT) e^{j2\pi v \sigma} d\sigma \\ &+ \frac{1}{A^2 NT} \int_{-\infty}^{\infty} \sum_{n=0}^{N-1} \sum_{\substack{m=0 \\ n \neq m}}^{N-1} p_n^*(\sigma - nT) p_m(\sigma - \tau - mT) e^{j2\pi v \sigma} d\sigma. \end{aligned} \quad (4.26)$$

Attention is first focused on those terms in Equation (4.26) for which  $n=m$ . Make the change of variables

$$\rho = \sigma - nT. \quad (4.27)$$

The terms for which  $n=m$  then become

$$\begin{aligned} &\frac{1}{A^2 NT} \sum_{n=0}^{N-1} e^{j2\pi v nT} \int_{-\infty}^{\infty} p_n^*(\rho) p_n(\rho - \tau) e^{j2\pi v \rho} d\rho \\ &= \frac{1}{A^2 N} \sum_{n=0}^{N-1} \phi_{nn}(\tau, v) e^{j2\pi v nT} \end{aligned} \quad (4.28)$$

where the autocorrelation function of  $p_n(t)$  was defined to be

$$\phi_{nn}(\tau, \nu) = \frac{1}{T} \int_{-\infty}^{\infty} p_n^*(\rho) p_n(\rho - \tau) e^{j2\pi\nu\rho} d\rho \quad (4.29)$$

Now focus on those terms for which  $n \neq m$ . As before, make use of the change of variables in Equation (4.27). Those terms for which  $n \neq m$  then become

$$\begin{aligned} & \frac{1}{A^2 NT} \sum_{n=0}^{N-1} \sum_{\substack{m=0 \\ n \neq m}}^{N-1} e^{j2\pi\nu nT} \int_{-\infty}^{\infty} p_n^*(\rho) p_m[\rho - \tau - (m - n)T] e^{j2\pi\nu\rho} d\rho \\ &= \frac{1}{A^2 N} \sum_{n=0}^{N-1} \sum_{\substack{m=0 \\ n \neq m}}^{N-1} \phi_{nm}[\tau + (m - n)T, \nu] e^{j2\pi\nu nT} \end{aligned} \quad (4.30)$$

where the cross-correlation function between  $p_n(t)$  and  $p_m(t)$  was defined to be

$$\phi_{nm}(\tau, \nu) = \frac{1}{T} \int_{-\infty}^{\infty} p_n^*(\rho) p_m(\rho - \tau) e^{j2\pi\nu\rho} d\rho \quad (4.31)$$

Combining the results obtained for  $n=m$  and  $n \neq m$ , the ambiguity function of Equation (4.26) is expressed as

$$\chi(\tau, \nu) = \frac{1}{A^2 N} \sum_{n=0}^{N-1} \left\{ \phi_{nn}(\tau, \nu) + \sum_{\substack{m=0 \\ n \neq m}}^{N-1} \phi_{nm}[\tau + (m - n)T, \nu] \right\} e^{j2\pi\nu nT} \quad (4.32)$$

The magnitude of the ambiguity function represents the magnitude of the coherent processor response to a pulse train arriving with delay,  $\tau$ , and Doppler shift,  $\nu$ . (This assumes that the Doppler shift is approximately unchanged over the different frequency hops within the pulse.) As pointed out in Section 4.3, Costas developed his approach of frequency-hopped waveforms in an attempt to shape the ambiguity function in the form of a thumbtack. The success of this approach depends upon the characteristics of  $\phi_{nn}(\tau, \nu)$  and  $\phi_{nm}(\tau, \nu)$ .

An analytical expression is now obtained for  $\phi_{nn}(\tau, \nu)$ . The case for which  $0 \leq \tau \leq T$  is considered first. Note that  $p_n^*(\rho)$  is zero outside the interval  $[0, T]$  while  $p_n(\rho - \tau)$  is zero outside the interval  $[\tau, \tau + T]$ . Since  $\tau > 0$ , their product is zero outside the interval  $[\tau, T]$ . Substitution of Equation (4.17) into Equation (4.29) then yields, for  $0 \leq \tau \leq T$ , that

$$\begin{aligned}\phi_{nn}(\tau, v) &= \frac{A^2}{T} \int_{\tau}^T e^{-j2\pi f_n \rho} e^{j2\pi f_n (\rho - \tau)} e^{j2\pi v \rho} d\rho \\ &= A^2 \frac{T - \tau}{T} \frac{\sin[\pi v(T - \tau)]}{\pi v(T - \tau)} e^{j[\pi v(T + \tau) - 2\pi f_n \tau]}\end{aligned}\quad (4.33)$$

Similarly, for  $-T \leq \tau \leq 0$ , the product of  $p_n^*(\rho)$  and  $p_n(\rho - \tau)$  is zero outside the interval  $[0, \tau + T]$ . For this case Equation (4.29) becomes

$$\begin{aligned}\phi_{nn}(\tau, v) &= \frac{A^2}{T} \int_0^{\tau+T} e^{-j2\pi f_n \rho} e^{j2\pi f_n (\rho - \tau)} e^{j2\pi v \rho} d\rho \\ &= A^2 \frac{T + \tau}{T} \frac{\sin[\pi v(T + \tau)]}{\pi v(T + \tau)} e^{j[\pi v(T + \tau) - 2\pi f_n \tau]}\end{aligned}\quad (4.34)$$

Finally, since  $p_n(t)$  is zero outside the interval  $[0, T]$ ,  $p_n^*(\rho)$  and  $p_n(\rho - \tau)$  do not overlap for  $|\tau| \geq T$ . It follows that  $\phi_{nn}(\tau, v)$  is zero for  $|\tau| \geq T$ . Combining the above results, the autocorrelation function of  $p_n(t)$  is given by

$$\phi_{nn}(\tau, v) = \begin{cases} A^2 \frac{(T - |\tau|)}{T} \frac{\sin[\pi v(T - |\tau|)]}{\pi v(T - |\tau|)} e^{j[\pi v(T + \tau) - 2\pi f_n \tau]} & , \quad |\tau| \leq T \\ 0 & , \quad |\tau| \geq T \end{cases} \quad (4.35)$$

The cross-correlation function between  $p_n(t)$  and  $p_m(t)$  is derived in a similar manner. For  $0 \leq \tau \leq T$  substitution of Equation (4.17) into Equation (4.31) results in

$$\begin{aligned}\phi_{nm}(\tau, v) &= \frac{A^2}{T} \int_{\tau}^T e^{-j2\pi f_n \rho} e^{j2\pi f_m (\rho - \tau)} e^{j2\pi v \rho} d\rho \\ &= A^2 \frac{T - \tau}{T} \frac{\sin[\pi \alpha_{nm}(T - \tau)]}{\pi \alpha_{nm}(T - \tau)} e^{-j[\pi \alpha_{nm}(T + \tau) + 2\pi f_m \tau]}\end{aligned}\quad (4.36)$$

where

$$\alpha_{nm} = f_n - f_m - v \quad (4.37)$$

Also, for  $-T \leq \tau \leq 0$ , we obtain

$$\begin{aligned}\phi_{nm}(\tau, v) &= \frac{A^2}{T} \int_0^{\tau+T} e^{-j2\pi f_n \rho} e^{j2\pi f_m (\rho - \tau)} e^{j2\pi v \rho} d\rho \\ &= A^2 \frac{T + \tau}{T} \frac{\sin[\pi \alpha_{nm}(T + \tau)]}{\pi \alpha_{nm}(T + \tau)} e^{-j[\pi \alpha_{nm}(T + \tau) + 2\pi f_m \tau]}\end{aligned}\quad (4.38)$$

Finally, since both  $p_n(t)$  and  $p_m(t)$  are zero outside the interval  $[0, T]$ ,  $p_n^*(\rho)$  and  $p_m(\rho - \tau)$  do not overlap for  $|\tau| > T$ . It follows that  $\phi_{nm}(\tau, v)$  is zero for  $|\tau| > T$ . Combining the above results, the cross-correlation function between  $p_n(t)$  and  $p_m(t)$  is given by

$$\phi_{nm}(\tau, v) = \begin{cases} A^2 \frac{(T - |\tau|)}{T} \frac{\sin[\pi \alpha_{nm}(T - |\tau|)]}{\pi \alpha_{nm}(T - |\tau|)} e^{-j[\pi \alpha_{nm}(T + \tau) + 2\pi f_m \tau]} & , \quad |\tau| \leq T \\ 0 & , \quad |\tau| \geq T \end{cases} \quad (4.39)$$

As required, note that  $\phi_{nm}(\tau, v)$  reduces to  $\phi_{mm}(\tau, v)$  for  $n=m$ .

With reference to Equation (4.32), it is now shown that the central peak of the ambiguity function is associated with the summation involving  $\phi_{nm}(\tau, v)$  while the sidelobe responses in the pedestal of the ambiguity function are, in the main, associated with the summation involving  $\phi_{nm}[\tau + (m-n)T, v]$ .

First, consider the  $\tau = 0$  axis. Along this axis the ambiguity function is given by

$$\chi(0, v) = \frac{1}{A^2 N} \sum_{n=0}^{N-1} \left\{ \phi_{nn}(0, v) + \sum_{\substack{m=0 \\ n \neq m}}^{N-1} \phi_{nm}[(m-n)T, v] \right\} e^{j2\pi v n T} \quad (4.40)$$

For  $n \neq m$ , where  $n$  and  $m$  are integers, observe that

$$|(m-n)T| \geq T \quad (4.41)$$

From Equation (4.39), it is concluded that

$$\phi_{nm}[(m-n)T, v] = 0, \quad n \neq m \quad (4.42)$$

Consequently, Equation (4.40) simplifies to

$$\chi(0, v) = \frac{1}{A^2 N} \sum_{n=0}^{N-1} \phi_{nn}(0, v) e^{j2\pi v n T} \quad (4.43)$$

However, from Equation (4.35),

$$\phi_{nn}(0, v) = A^2 \frac{\sin(\pi v T)}{\pi v T} e^{j\pi v T} \quad (4.44)$$

It follows that

$$\begin{aligned} \chi(0, v) &= \frac{\sin(\pi v T)}{\pi v NT} e^{j\pi v T} \sum_{n=0}^{N-1} e^{j2\pi v n T} \\ &= e^{j\pi v NT} \frac{\sin(\pi v NT)}{\pi v NT} \end{aligned} \quad (4.45)$$

where use was made of the result that

$$\begin{aligned} \sum_{n=0}^{N-1} e^{j2\pi v n T} &= \frac{e^{j2\pi v NT} - 1}{e^{j2\pi v T} - 1} \\ &= \frac{e^{j\pi v NT}}{e^{j\pi v T}} \frac{\sin(\pi v NT)}{\sin(\pi v T)} \end{aligned} \quad (4.46)$$

Observe that

$$\chi(0,0) = 1 \quad (4.47)$$

and that the first zeros of  $\chi(0,v)$  occur for

$$v = \pm \frac{1}{NT} \quad (4.48)$$

As a result, the Doppler resolution of the N-pulse frequency-hopped signal is identical to that of a CW pulse of duration NT.

Costas [9] introduces the normalized frequency variable

$$y = vT \quad (4.49)$$

Since the frequency channel spacing is  $1/T$ , as determined by Equation (4.2),  $y$  is a measure of frequency in units of frequency-hop spacing. The ambiguity function along the  $\tau = 0$  axis can now be expressed as

$$\chi(0,y) = e^{j\pi Ny} \frac{\sin(\pi Ny)}{\pi Ny} \quad (4.50)$$

for which the first zeros are given by

$$y = \pm \frac{1}{N} \quad (4.51)$$

The ambiguity function along the  $v=0$  axis is considered next. From Equation (4.32)

$$\chi(\tau,0) = \frac{1}{A^2 N} \sum_{n=0}^{N-1} \left\{ \phi_{nn}(\tau,0) + \sum_{\substack{m=0 \\ n \neq m}}^{N-1} \phi_{nm}[\tau + (m-n)T, 0] \right\} \quad (4.52)$$

The summation involving the cross-correlation terms can no longer be ignored. However, we first concentrate on the contribution by the autocorrelation terms alone. For this purpose, define

$$\chi'(\tau,0) = \frac{1}{A^2 N} \sum_{n=0}^{N-1} \phi_{nn}(\tau,0) \quad (4.53)$$

From Equation (4.35)

$$\phi_{nn}(\tau,0) = \begin{cases} A^2 \frac{(T-|\tau|)}{T} e^{-j2\pi f_n \tau} & |\tau| \leq T \\ 0 & |\tau| \geq T \end{cases} \quad (4.54)$$

With reference to Equation (4.4), it follows that

$$\chi'(\tau,0) = \frac{(T-|\tau|)}{NT} \sum_{n=0}^{N-1} e^{-j2\pi \frac{\theta_n \tau}{T}}, |\tau| \leq T \quad (4.55)$$

Because the sequence of integers in the set,  $\{\theta_n\}$ , consists of all integers between 0 and  $(N-1)$  and each integer appears only once, the ordering of terms in the summation of Equation (4.55) is inconsequential. Therefore, the summation can be written as

$$\begin{aligned} \sum_{n=0}^{N-1} e^{-j2\pi \frac{\theta_n \tau}{T}} &= \sum_{n=0}^{N-1} e^{-j2\pi \frac{n \tau}{T}} \\ &= \frac{e^{-j2\pi \frac{N \tau}{T}} - 1}{e^{-j2\pi \frac{1 \tau}{T}} - 1} = e^{-j\pi \left(\frac{N-1}{T}\right) \tau} \frac{\sin\left(\pi \frac{N}{T} \tau\right)}{\sin\left(\pi \frac{1}{T} \tau\right)} \end{aligned} \quad (4.56)$$

It follows that

$$\chi'(\tau,0) = \frac{(T-|\tau|)}{T} e^{-j\pi \left(\frac{N-1}{T}\right) \tau} \frac{\sin\left(\pi \frac{N}{T} \tau\right)}{N \sin\left(\pi \frac{1}{T} \tau\right)}, |\tau| \leq T \quad (4.57)$$

Observe from Equation (4.54) that  $\phi_{mn}(\tau,0)=0$  for  $|\tau| \geq T$ . Hence,

$$\chi'(\tau,0) = 0, \quad |\tau| \geq T \quad (4.58)$$

It is seen that the  $\tau$ -axis response beyond  $|\tau| = T$  is entirely due to the summation over the cross-correlation terms in Equation (4.52).

Costas [9] introduces the normalized delay variable

$$x = \frac{\tau}{T} \quad (4.59)$$

Since each subpulse is of width,  $T$ ,  $x$  is a measure of delay in units of subpulse width. Note that  $|\tau| \leq T$  implies  $|x| \leq 1$ . For this case  $\chi'(\tau,0)$  becomes

$$\chi'(x,0) = (1-|x|) e^{-j\pi(N-1)x} \frac{\sin(\pi N x)}{N \sin(\pi x)}, |x| \leq 1 \quad (4.60)$$

Observe that

$$\chi'(0,0) = 1 \quad (4.61)$$

Since Equation (4.22) is, also, valid, it can be deduced from Equation (4.61) that the cross-correlation terms do not contribute to the ambiguity function at the origin. The first zeros of  $\chi'(x,0)$  to either side of the origin occur at

$$x = \pm \frac{1}{N} \quad (4.62)$$

or, equivalently, at

$$\tau = \pm \frac{T}{N} \quad (4.63)$$

This is a measure of the delay resolution for the Costas signal.

It is of interest to evaluate the Doppler and delay resolutions in terms of the time-bandwidth product of the frequency-hopped pulse. The duration of this pulse is

$$T_d = NT \quad (4.64)$$

Because each subpulse is of duration  $T$ , the subpulse bandwidth is approximately  $1/T$ . In addition, the frequency hops span a frequency range of extent equal to  $N\Delta f = N/T$ . Thus, the bandwidth of the frequency-hopped pulse is approximately

$$BW = \frac{N}{T} \quad (4.65)$$

As a result, the time-bandwidth product of the Costas signal is approximately

$$T_d(BW) = (NT) \left( \frac{N}{T} \right) = N^2 \quad (4.66)$$

Note that

$$\frac{(BW)}{N^2} = \frac{1}{T_d} = \frac{1}{NT} \quad (4.67)$$

while

$$\frac{T_d}{N^2} = \frac{1}{BW} = \frac{T}{N} \quad (4.68)$$

Recall that the Doppler resolution, from Equation (4.48), is  $1/(NT)$  and the delay resolution, from Equation (4.63), is  $T/N$ . Therefore, the compression ratio for the Costas signal is  $N^2$  in both the Doppler and delay domains.

The cross-correlation terms in Equation (4.52) are now examined. For  $\tau = 0$  note that

$\phi_{nm}[\tau+(m-n)T,0]$  becomes  $\phi_{nm}[(m-n)T,0]$ . Because  $n \neq m$ ,  $|(m-n)T| \geq T$ . It follows from Equation (4.39) that.



$$\phi_{nm}[(m-n)T, 0] = 0, \quad n \neq m. \quad (4.69)$$

This is consistent with the observation, previously pointed out, that the cross-correlation terms do not contribute to the central peak of the ambiguity function at  $\tau = \nu = 0$ .

With reference to Equation (4.39), note that  $\phi_{nm}[\tau + (m-n)T, 0]$  is not identically zero only over the range of  $\tau$  governed by

$$|\tau + (m-n)T| \leq T. \quad (4.70)$$

This inequality can be rewritten as

$$-T \leq \tau + (m-n)T \leq T \quad (4.71)$$

or, equivalently, as

$$-T - (m-n)T \leq \tau \leq T - (m-n)T. \quad (4.72)$$

Hence, along the  $\tau$ -axis,  $\phi_{nm}[\tau + (m-n)T, 0]$  spans an interval of length  $2T$  centered at  $-(m-n)T$ . Since  $n \neq m$  in the summation over  $m$  in Equation (4.52), the interval given by  $-T \leq \tau \leq T$  is excluded. Nevertheless, for a fixed value of  $n$  and values of  $m$  that differ by unity, the corresponding cross-correlation terms do have intervals that overlap. The overlapping of these terms produces reinforcement and cancellation effects which are quite complex because of the amplitude and phase relationships involved. It is difficult to predict the exact peak values of the sidelobes. However, they are expected to be on the order of  $1/N$ , as suggested by the relevant Costas array.

From Equations (4.4) and (4.37) note that

$$\alpha_{nm} = f_n - f_m - \nu = \frac{\theta_n - \theta_m}{T} - \nu. \quad (4.73)$$

For  $|\tau + (m-n)T| \leq T$ , use of Equation (4.73) in Equation (4.39) yields

$$|\phi_{nm}[\tau + (m-n)T, \nu]| = A^2 \frac{(T - |\tau + (m-n)T|)}{T} \left| \frac{\sin[\pi(\frac{\theta_n - \theta_m}{T} - \nu)(T - |\tau + (m-n)T|)]}{\pi(\frac{\theta_n - \theta_m}{T} - \nu)(T - |\tau + (m-n)T|)} \right|. \quad (4.74)$$

Consider the case for which

$$\tau = (n-m)T. \quad (4.75)$$

Then the magnitude in Equation (4.74) becomes

$$|\phi_{nm}(0, v)| = A^2 \left| \frac{\sin \left[ \pi \left( \frac{\theta_n - \theta_m}{T} - v \right) T \right]}{\pi \left( \frac{\theta_n - \theta_m}{T} - v \right) T} \right| . \quad (4.76)$$

Now let

$$v = \frac{r}{T} \quad (4.77)$$

where  $r$  is any integer. Equation (4.76) can then be expressed as

$$\left| \phi_{nm} \left( 0, \frac{r}{T} \right) \right| = A^2 \left| \frac{\sin \beta}{\beta} \right| \quad (4.78)$$

where

$$\beta = \pi \left( \frac{\theta_n - \theta_m - r}{T} \right) T = \pi (\theta_n - \theta_m - r) . \quad (4.79)$$

Because  $(\theta_n - \theta_m - r)$  is an integer, it follows that

$$\left| \phi_{nm} \left( 0, \frac{r}{T} \right) \right| = \begin{cases} A^2 , & r = \theta_n - \theta_m \\ 0 , & r \neq \theta_n - \theta_m \end{cases} . \quad (4.80)$$

Therefore,  $\phi_{nm}[\tau + (m - n)T, v]$  attains its peak value of  $A^2$  for values of  $\tau$  and  $v$  given by

$$\tau_p = (n - m)T \text{ and } v_p = \frac{\theta_n - \theta_m}{T} . \quad (4.81)$$

Defining

$$L = n - m , \quad (4.82)$$

$\tau_p$  and  $v_p$  can be rewritten as

$$\tau_p = LT \text{ and } v_p = \frac{\theta_{m+L} - \theta_m}{T} = \frac{d_{L,m+1}}{T} \quad (4.83)$$

where  $d_{L,m+1}$  is the difference given by Equation (4.12). Consequently, the frequencies at which the cross-correlation terms peak, for a specified value of  $L$ , can be obtained from the difference triangle of Section 4.3. These peak positions are, also, reflected in the corresponding Costas array. Although the actual peak values of the

sidelobes in the pedestal are difficult to predict, they are expected to be small relative to the central peak. This is illustrated in the following examples.

The examples are based on an  $N=10$  and an  $N=30$  Costas array. For  $N=10$ , the firing order is given by the sequence of ordered integers in the set

$$\{\theta_n\} = \{1, 3, 7, 4, 9, 8, 6, 2, 5, 0\}. \quad (4.84)$$

For  $N=30$ , the firing order is determined from the set

$$\{\theta_n\} = \left\{ \begin{array}{l} 2, 8, 26, 18, 25, 15, 16, 19, 28, 24, 12, 7, 23, 9, 29, \\ 27, 21, 3, 11, 4, 14, 13, 10, 1, 5, 17, 22, 6, 20, 0 \end{array} \right\}. \quad (4.85)$$

They are referred to as Welch-codes because they can be constructed from a theorem proposed by L. R. Welch [11].

Various views of the ambiguity surface for the 10-pulse Welch code are shown in Figure 4.8 [9].  $|\chi(x, y)|$  is plotted where  $x$  and  $y$  are the normalized variables of Equations (4.59) and (4.49), respectively. In Figure 4.8(a) observe that the density of peaks increases towards the origin, as predicted by the difference triangle and the ambiguity matrix for the Costas array. A different perspective of the ambiguity surface is shown in Figure 4.8(b). Note that sidelobe peaks far from the origin remain below the  $1/N$  level. However, those near the origin tend to have their values above the  $1/N$  level due to the overlapping of the cross-correlation terms. Nevertheless, most peaks remain below the  $2/N$  level.

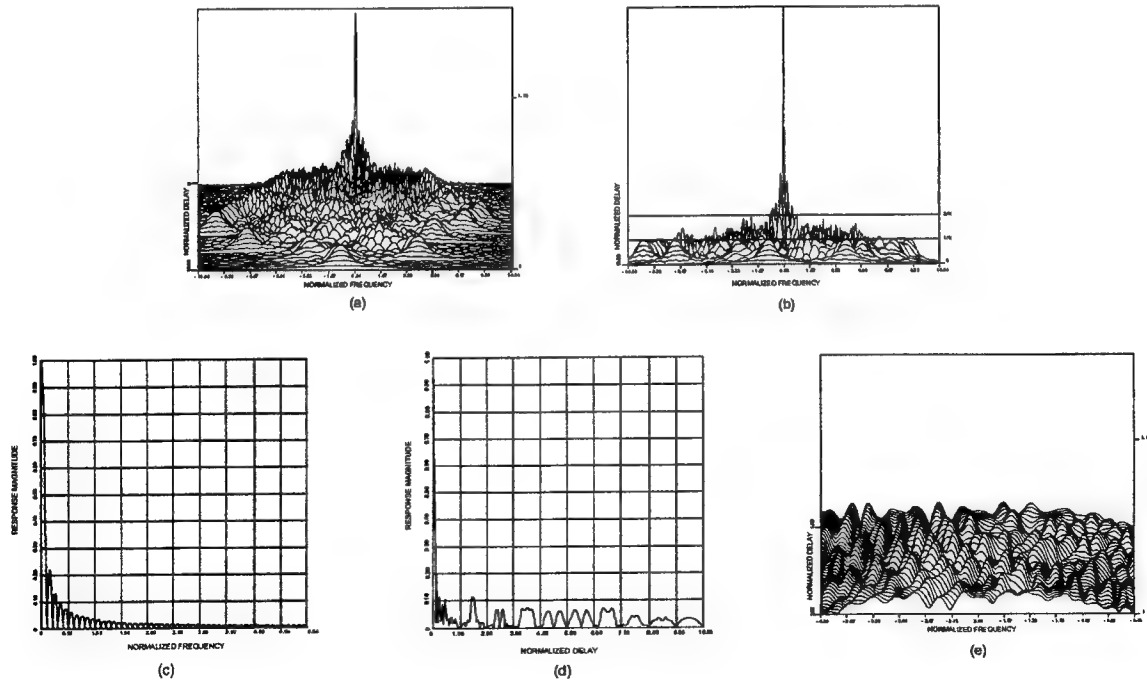


**Figure 4.8:** Various views of the ambiguity surface for the 10-pulse Welch code are shown: (a) an overview, (b) a different perspective, (c) Doppler response for  $x=0$ , (d) delay response for  $y=0$ , (e) pedestal region near the highest sidelobe peak.

The Doppler frequency response for  $x=0$  is shown in Figure 4.8(c). As predicted by Equation (4.50), a  $|\sin(\pi N y) / \pi N y|$  behavior is seen with the zero of the main lobe occurring at  $y=0.1=1/N$ . The delay response for  $y=0$  is shown in Figure 4.8(d). From  $x=0$  to  $x=1$  the  $|\sin(\pi N x) / N \sin(\pi x)|$  behavior, as noted in Equation (4.60), is seen. Beyond  $x=1$ , the  $\phi_{nm}(x,0)$  terms vanish and only the  $\phi_{nm}(x,0)$  cross-correlation terms contribute to the ambiguity function. As predicted by Equations (4.75) and (4.80), observe that  $|\chi(x,0)| = 0$  for all integer values of  $x$ .

The largest sidelobe peak, due to overlapping of cross-correlation terms, was found to have a value of 0.21. Because  $N=10$ , a single cross-correlation term would result in a sidelobe peak of height 0.1. Thus, the largest sidelobe peak has a value which is 2.1 times larger than would be expected from a single cross-correlation term. The general neighborhood of the largest sidelobe peak is shown in Figure 4.8(e). The phasing and overlap of the cross-correlation terms are seen to produce isolated peaks approximately twice the  $1/N$  value predicted by the Costas array.

Various views of the ambiguity surface for the 30-pulse Welch code are shown in Figure 4.9 [9]. As was done with Figure 4.8,  $|\chi(x,y)|$  is plotted where  $x$  and  $y$  are the normalized variables of Equations (4.59) and (4.49), respectively. Pedestal spiking above  $1/N$  is evident near the main peak of Figure 4.9(a). However, away from the main peak, most of the sidelobes have peak values approximately equal to  $1/N$ . The largest pedestal peaks are on the order of  $2/N$ . Clearly, the pedestal peaks can be reduced by increasing the value of  $N$ .

Figure 4.9(b) shows a plot of  $|\chi(x,y)|$  where values are evaluated only at integer values of  $x$  and  $y$ . As would be expected from Equations (4.75) and (4.80), the pedestal region of the ambiguity surface is either zero or  $1/N$  depending upon whether or not there is a cross-correlation peak. The peaks of the individual cross-correlation terms are clearly displayed by this artifice. However, note that triangles indicate isolated peaks while the flat-topped sections indicate two or more frequency-adjacent peaks. The density of peaks is seen to increase near the main lobe, as predicted by the ambiguity matrix for the corresponding Costas array.

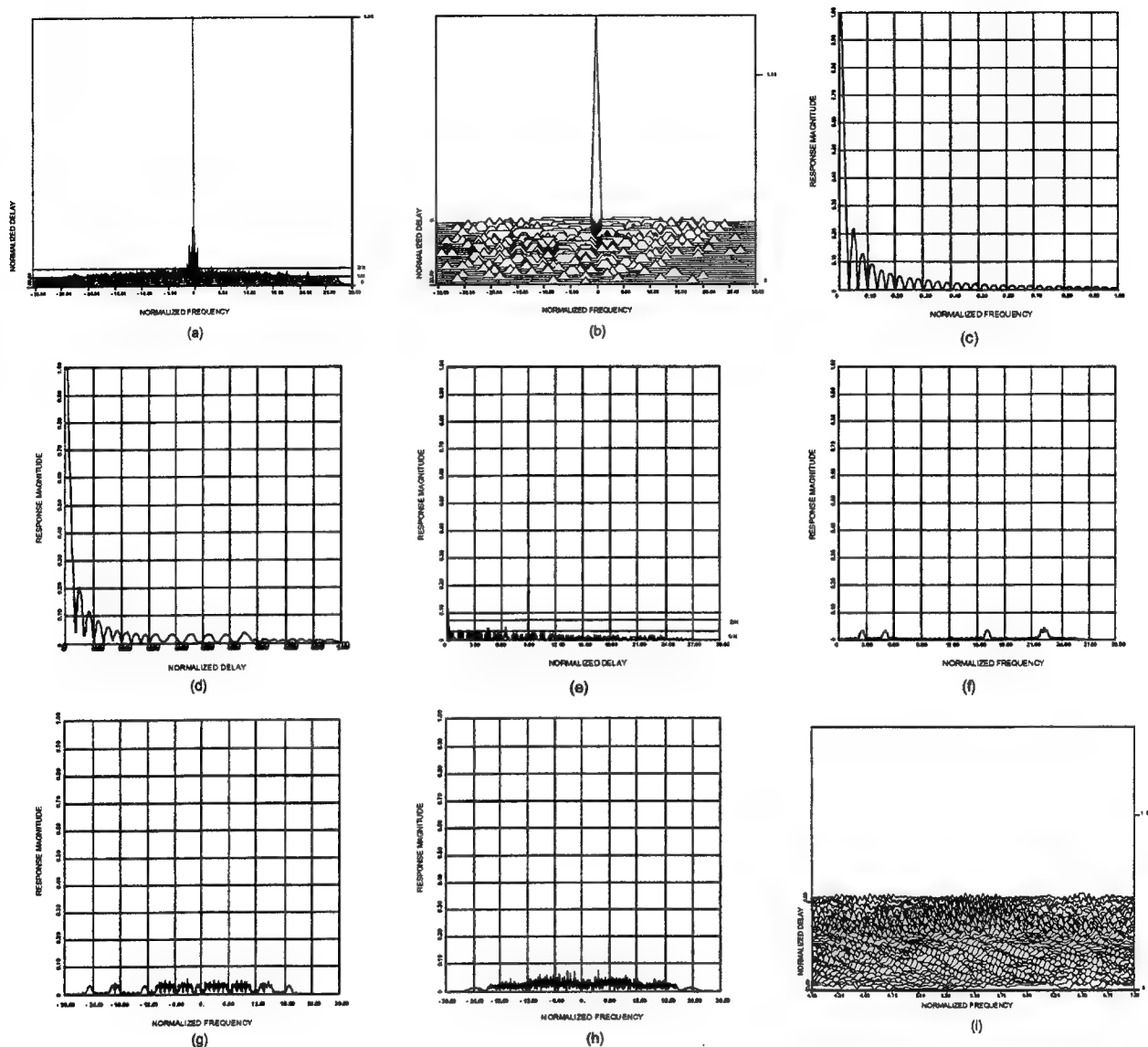


**Figure 4.9:** Various views of the ambiguity surface for the 30-pulse Welch code are shown: (a) an overview, (b) plot using only integer values for  $x$  and  $y$ , (c) Doppler response at  $x=0$ , (d) delay response at  $y=0$ , (e) complete delay axis response, (f) Doppler response at  $x=25$ , (g) Doppler response at  $x=5$ , (h) Doppler response at  $x=1.4$ , (i) pedestal region near the highest sidelobe peak.

The Doppler response at  $x=0$  is shown in Figure 4.9 (c) for values of  $y$  between 0 and 1. As was the case with Figure 4.8(c), the behavior is of the form  $|\sin(\pi N y) / \pi N y|$ . As expected, the first zero of the main lobe occurs at  $y=0.0333=1/30$ . The delay axis response at  $y=0$  is shown in Figure 4.9(d) for values of  $x$  between 0 and 1. As with Figure 4.8(d), the behavior is dictated by Equation (4.60). Consequently, the first zero appears in the vicinity of  $x=1/30$ . The complete positive delay axis for  $y=0$  is shown in Figure 4.9(e). The main peak is hard to see because of the scale chosen for the  $x$ -axis. However, this choice of scale clearly demonstrates that the sidelobes are very well behaved with relatively few excursions above the  $1/N$  value.

Figure 4.9(f) is a frequency cut taken at a delay of  $x=25$ . With reference to the set of ordered integers in Equation (4.85), the 25<sup>th</sup> row of the difference triangle is given by

$$d_{25,j} = \theta_{25+j-1} - \theta_{j-1} \quad (4.86)$$

where  $j$  assumes all positive integer values such that

$$25 + j \leq 30 \quad (4.87)$$

As a result,

$$\begin{aligned} d_{25,1} &= \theta_{25} - \theta_0 = 17 - 2 = 15 \\ d_{25,2} &= \theta_{26} - \theta_1 = 22 - 8 = 14 \\ d_{25,3} &= \theta_{27} - \theta_2 = 6 - 26 = -20 \\ d_{25,4} &= \theta_{28} - \theta_3 = 20 - 18 = 2 \\ d_{25,5} &= \theta_{29} - \theta_4 = 0 - 25 = -25 \end{aligned} \quad (4.88)$$

Recall from the discussion of the difference triangle in Section 4.3 that  $d_{ij}=k$  implies a peak at  $x=i$  and  $y=k$ . Therefore, for the frequency cut at  $x=25$ , peaks are predicted at  $y= -25, -20, 2, 14$ , and  $15$ . These sidelobe peaks are clearly seen in Figure 4.9(f). Observe that the isolated cross-correlation terms have their peak values equal to  $1/N=0.0333$ . However, the two peaks at  $y=14,15$  experience mutual interference effects that result in a wider peak whose magnitude exceeds  $1/N$  but is less than  $2/N$ .

A frequency cut for  $x=5$  is shown in Figure 4.9(g). Because this is closer to the main peak at the origin, many more sidelobes appear than was the case for  $x=25$ . Near the center of this plot the mutual interference effects due to groups of frequency-adjacent cross-correlation peaks are clearly evident. The largest peak values are approximately equal to  $2/N$ .

The largest peak in the pedestal region was found to be at  $x=1.4$  and had a value equal to  $0.078$  which is  $2.34$  times the  $1/N$  value of  $0.0333$ . Figure 4.9(h) shows a frequency cut at this delay with the largest peak occurring near  $y=3$ . The ambiguity surface for the region near the pedestal highest peak is shown in Figure 4.9(i). The rapid undulations of this surface are to be compared with the comparable surface in Figure 4.8(e). Note, also, the lower level of the surface for  $N=30$  as compared to that for  $N=10$ . Increasing  $N$  from  $10$  to  $30$  has increased both the range and Doppler resolution by a factor of  $3$  and has lowered the pedestal region by about the same factor.

An advantage of frequency-hopped waveforms is their flexibility with regard to ordering of the frequency steps. For some radar applications it may be more desirable to have a lower pedestal than the thumbtack shape approximated by the Costas signal. Figure 4.10 shows the ambiguity surface of a 10-pulse frequency stepped linear FM signal having spacings equal to  $1/T$ . The classic FM ridge is clearly in evidence and contains most of the volume under the surface. Comparison of this surface with that shown in Figure 4.8(a), which was, also, for a 10-pulse burst, reveals the much lower pedestal of the linear FM waveform. Although this is an advantage, there is potential for considerable ambiguity due to the ridge and nearby sidelobe structure.

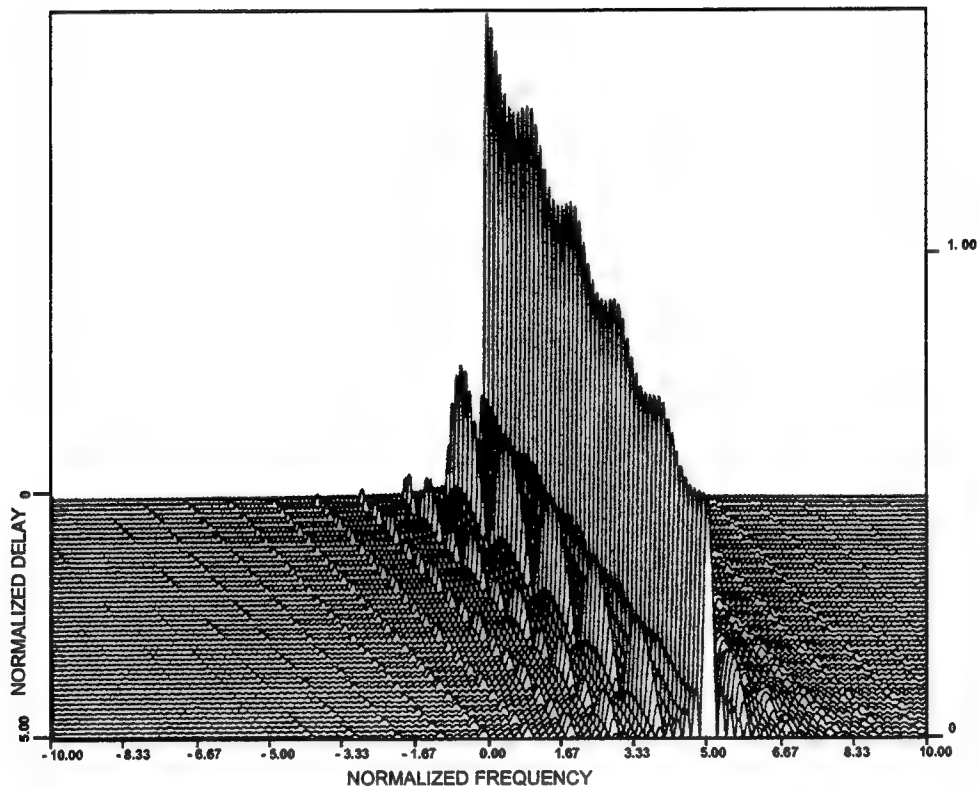


**Figure 4.10:** The ambiguity surface is shown for a 10-pulse frequency stepped linear FM signal with spacing equal to  $1/T$ .

## CHAPTER 5

### AN INTERFEROMETER WAVEFORM EMPLOYING ORTHOGONAL FREQUENCY DIVISION MULTIPLEXING

#### 5.1 Orthogonal Frequency Division Multiplexing [12]

##### 5.1.1 Overview of OFDM

Orthogonal frequency division multiplexing (OFDM) is a modulation technique that has been proposed recently for use in broad-band mobile multimedia applications. Because frequency-selective and time-variant channels are typically encountered in these applications, channel equalization must be incorporated to achieve an acceptable level of performance. The quality of service is usually measured in terms of data rate and bit error rate.

Fading channels can be frequency selective when multipath propagation is experienced and can become time-variant when the transmitter and/or receiver are in motion. The computational requirements for an equalizer to be used to compensate for a frequency-selective channel increases in complexity with the data rate. Furthermore, the system resources (or overhead) needed for the estimation of time-variant channel parameters can be considerable.

To overcome these drawbacks OFDM has been considered for high data-rate applications. In effect, OFDM divides the radio channel into many narrowband subchannels which appear to be frequency nonselective. Thus, the task of channel equalization is simplified to estimating a single complex factor (or transfer function) for each subcarrier. Such a channel estimation can be realized by inserting pilot symbols with known modulation into the transmitted signal. Based on these pilot symbols the receiver can measure the channel transfer functions for each subcarrier using interpolation techniques. In this case, each subcarrier can be demodulated coherently.

Alternatively, differential modulation can be performed in a manner similar to that used with M-ary differential phase shift keying (M-DPSK). With OFDM this has been extended for multi-level modulation to a combined differential amplitude and phase modulation in order to achieve a higher bandwidth efficiency and still rather good performance. This modulation technique is termed differential amplitude and phase shift keying (DAPSK). The performance of OFDM systems with differential modulation compares quite well with systems using nondifferential modulation and coherent demodulation. Furthermore, the computational complexity in the demodulation process is quite low for differential modulation.

Channel coding is an important ingredient for OFDM systems. Transmission over a frequency-selective channel implies that some of the subcarriers are strongly attenuated and errors occur even with a high average signal power. In this flat fading situation an efficient channel coding leads to a very high coding gain. For this reason, OFDM systems will always make use of channel coding.

Also, apart from simplifying the channel equalization with respect to single carrier systems, OFDM offers more possibilities to adapt the transmission system to the communications channel by varying the modulation of the subcarriers. However, an optimal adaptation is limited to quasistationary channels.

As compared to single carrier systems, the most important advantage of the OFDM transmission technique is obtained in frequency selective channels. The signal processing in the receiver is rather simple in this case because, after transmission over the communications channel, the orthogonality of the OFDM subcarriers is maintained and the channel interference effect is reduced to a multiplication of each subcarrier by a complex factor. Therefore, equalizing the signal is very simple, whereas equalization may not be feasible in the case of single carrier transmission covering the same bandwidth.



### 5.1.2 OFDM Signal Characterization

As was done in Section 4.4, the discussion is carried out at baseband through the use of complex envelopes. OFDM was chosen for the interferometer signal because it can be made to closely resemble the Costas signal selected in Chapter 4 for the radar waveform. This should greatly enhance the ability of the interferometer signal to mask the radar signal transmitted through the sidelobes of the main radar.

In general, an OFDM signal consists of  $M$  subcarriers, each of duration  $T_s$ . The baseband frequencies of the subcarriers are given by

$$f_m = \frac{m}{T_s}; m = 0, 1, \dots, (M-1). \quad (5.1)$$

Consequently, their spacing is

$$\begin{aligned} \Delta f &= f_{m+1} - f_m = \frac{m+1}{T_s} - \frac{m}{T_s} \\ &= \frac{1}{T_s}; m = 0, 1, \dots, (M-1). \end{aligned} \quad (5.2)$$

When  $T_s = T$  and  $M = N$ , the OFDM signal frequencies are identical to those used with the Costas signal.

The  $m^{\text{th}}$  subcarrier signal is described analytically by

$$g_m(t) = \begin{cases} B e^{j2\pi f_m t}, & 0 \leq t \leq T_s \\ 0, & \text{otherwise} \end{cases}. \quad (5.3)$$

Each subcarrier can be modulated independently with the complex modulation symbol,  $S_{k,m}$ , where  $k$  refers to time and  $m$  refers to the subcarrier frequency. Thus, the  $k^{\text{th}}$  OFDM block extending over the interval  $[kT_s, (k+1)T_s]$  is characterized by

$$s_k(t) = \sum_{m=0}^{M-1} S_{k,m} g_m(t - kT_s). \quad (5.4)$$

The total interferometer signal, consisting of  $K$  OFDM blocks is given by

$$s_{\text{IFM}}(t) = \sum_{k=0}^{K-1} s_k(t) = \sum_{k=0}^{K-1} \sum_{m=0}^{M-1} S_{k,m} g_m(t - kT_s). \quad (5.5)$$

The energy of the interferometer signal is

$$\begin{aligned} E_{\text{IFM}} &= \int_0^{KT_s} |s_{\text{IFM}}(t)|^2 dt = \int_0^{KT_s} s_{\text{IFM}}(t) s_{\text{IFM}}^*(t) dt \\ &= \int_0^{KT_s} \left\{ \sum_{k=0}^{K-1} \sum_{m=0}^{M-1} S_{k,m} g_m(t - kT_s) \right\} \left\{ \sum_{\ell=0}^{K-1} \sum_{n=0}^{M-1} S_{\ell,n}^* g_n^*(t - \ell T_s) \right\} dt. \end{aligned} \quad (5.6)$$

Because the OFDM blocks do not overlap when  $k \neq \ell$ ,

$$g_m(t - kT_s) g_n^*(t - \ell T_s) = 0, \quad k \neq \ell. \quad (5.7)$$

Consequently, the expression for  $E_{\text{IFM}}$  simplifies to

$$E_{\text{IFM}} = \sum_{k=0}^{K-1} \sum_{m=0}^{M-1} \sum_{n=0}^{M-1} S_{k,m} S_{k,n}^* \int_{kT_s}^{(k+1)T_s} g_m(t - kT_s) g_n^*(t - kT_s) dt . \quad (5.8)$$

However, through direct integration, it is readily shown that all subcarriers are mutually orthogonal over the time intervals  $[kT_s, (k+1)T_s]$  for  $k=0, 1, \dots, (K-1)$ . In particular,

$$\begin{aligned} & \int_{kT_s}^{(k+1)T_s} g_m(t - kT_s) g_n^*(t - kT_s) dt \\ &= B^2 \int_{kT_s}^{(k+1)T_s} e^{j2\pi f_m(t - kT_s)} e^{-j2\pi f_n(t - kT_s)} dt \\ &= \begin{cases} B^2 T_s, & m = n \\ 0, & \text{otherwise} \end{cases} . \end{aligned} \quad (5.9)$$

It follows that

$$E_{\text{IFM}} = B^2 T_s \sum_{k=0}^{K-1} \sum_{m=0}^{M-1} |S_{k,m}|^2 . \quad (5.10)$$

However, in general, the modulation symbols are selected randomly depending upon the data to be transmitted. Assuming stationarity such that the statistical average of  $|S_{k,m}|^2$  is constant independent of  $k$  and  $m$ , let

$$\sigma_s^2 = E[|S_{k,m}|^2] \quad (5.11)$$

where  $E[\cdot]$  denotes the expectation operator. The average energy of the interferometer signal is then given by

$$E\{E_{\text{IFM}}\} = KM\sigma_s^2 B^2 T_s . \quad (5.12)$$

The normalized interferometer signal with unit average energy is, therefore,

$$\begin{aligned} f_{\text{IFM}}(t) &= \frac{1}{\sqrt{E\{E_{\text{IFM}}\}}} S_{\text{IFM}}(t) \\ &= \frac{1}{B\sigma_s \sqrt{KMT_s}} \sum_{k=0}^{K-1} \sum_{m=0}^{M-1} S_{k,m} g_m(t - kT_s) . \end{aligned} \quad (5.13)$$

### 5.1.3 OFDM Signal Recovery Employing a Guard Interval

As shown in Equation (5.9), all subcarriers are mutually orthogonal over the time intervals given by  $[kT_s, (k+1)T_s]$  where  $k=0, 1, \dots, (K-1)$ . This orthogonality enables the employment of correlation to recover the modulation symbols,  $S_{k,m}$ . Specifically, for the  $k^{\text{th}}$  OFDM block, note that

$$\begin{aligned}
& \frac{1}{B^2 T_s} \int_{kT_s}^{(k+1)T_s} s_k(t) g_m^*(t - kT_s) dt \\
&= \frac{1}{B^2 T_s} \int_{kT_s}^{(k+1)T_s} \left\{ \sum_{n=0}^{M-1} S_{k,n} g_n(t - kT_s) \right\} g_m^*(t - kT_s) dt \\
&= S_{k,m}
\end{aligned} \tag{5.14}$$

where use was made of Equation (5.9).

In practice, a guard interval is added to the subcarrier signal in order to avoid intersymbol interference which may arise in multipath channels. Let the length of the guard interval be denoted by  $T_g$ . The total OFDM block duration is now equal to

$$T = T_g + T_s \tag{5.15}$$

The  $m^{\text{th}}$  subcarrier is redefined by

$$g_m(t) = \begin{cases} B e^{j2\pi f_m t} & , \quad -T_g \leq t \leq T_s \\ 0 & , \quad \text{otherwise} \end{cases} \tag{5.16}$$

where, even with the increase in block duration, the subcarrier frequencies are still determined from Equation (5.1). Because the symbol duration is  $T$ , Equation (5.4) and (5.5) are modified such that

$$s_k(t) = \sum_{m=0}^{M-1} S_{k,m} g_m(t - kT) \tag{5.17}$$

and

$$s_{\text{IFM}}(t) = \sum_{k=0}^{K-1} s_k(t) = \sum_{k=0}^{K-1} \sum_{m=0}^{M-1} S_{k,m} g_m(t - kT) \tag{5.18}$$

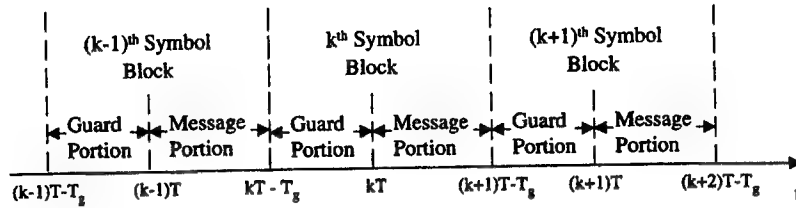
The guard interval is removed at the receiver and only the time intervals  $[kT, (k+1)T - T_g]$ , where  $k=0, 1, \dots, (K-1)$ , are actually processed. As a result, the guard interval in the  $k^{\text{th}}$  block is a pure system overhead. Observe that each processing interval is of length

$$(k+1)T - T_g - kT = T - T_g = T_s \tag{5.19}$$

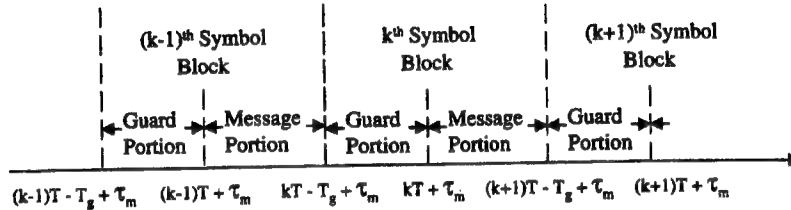
Consequently the orthogonality of Equation (5.9) is maintained and

$$S_{k,m} = \frac{1}{B^2 T_s} \int_{kT}^{(k+1)T - T_g} s_k(t) g_m^*(t - kT) dt \tag{5.20}$$

Assuming the guard interval length is larger than  $\tau_m$ , the maximum channel delay, no intersymbol interference will occur. This is illustrated in Figure 5.1. Note that the message portion of the maximally delayed  $k^{\text{th}}$  symbol block, arising from multipath, does not overlap the message portion of the direct path's  $(k+1)^{\text{th}}$  symbol block since  $T_g > \tau_m$ . Thus, there is no intersymbol interference between consecutive symbol blocks. However, the message portion of the maximally delayed  $k^{\text{th}}$  symbol block does overlap the message portion of the  $k^{\text{th}}$  symbol block in the direct path. This results in fading which is compensated for by channel equalization.



(a)



(b)

Figure 5.1: The guard and message intervals are shown for (a) the direct path signal and (b) the maximally delayed multipath signal.

#### 5.1.4 Use of Fast Fourier Transform in OFDM Implementation

OFDM is, in effect, a parallel system. A principal objection to the use of parallel systems is the complexity of the equipment (filters, modulators, etc.) required to implement the system. However, the modulation and demodulation processes involved with OFDM can be implemented in the digital signal processing parts of the transmitter and receiver employing Fast Fourier Transform techniques. This is discussed next.

From Equations (5.16) and (5.17) the  $k^{\text{th}}$  OFDM block is given by

$$s_k(t) = \sum_{m=0}^{M-1} BS_{k,m} e^{j2\pi f_m(t-kT)} \quad (5.21)$$

Although the above expression is valid for

$$kT - T_g \leq t \leq (k+1)T - T_g, \quad (5.22)$$

the message portion extends only over the interval

$$kT \leq t \leq (k+1)T - T_g, \quad (5.23)$$

as illustrated in Figure 5.1(a). An estimate of the Nyquist sampling rate for the  $k^{\text{th}}$  OFDM block is obtained by approximating its spectrum.

The spectrum of the  $m^{\text{th}}$  subcarrier is

$$\begin{aligned}
 G_m(f) &= \int_{-T_g}^{T_g} g_m(t) e^{-j2\pi f t} dt = \int_{-T_g}^{T_g} B e^{j2\pi(f_m - f)t} dt \\
 &= B \frac{e^{j2\pi(f_m - f)T_g} - e^{-j2\pi(f_m - f)T_g}}{j2\pi(f_m - f)} \\
 &= BT e^{j2\pi(f_m - f)\left(\frac{T_s - T_g}{2}\right)} \frac{\sin[\pi T(f - f_m)]}{\pi T(f - f_m)} .
 \end{aligned} \tag{5.24}$$

Observe that the first zeros in the spectral main lobe occur at  $f = f_m \pm 1/T$  where  $T \geq T_g$ . Therefore, the width of the main lobe is  $2/T$ . As noted by Equation (5.2), the subcarriers are spaced in frequency according to  $\Delta f = 1/T_g$ . Consequently, for  $M \gg 2$ , the bandwidth of each OFDM block is approximately

$$BW = M \Delta f = \frac{M}{T_g} . \tag{5.25}$$

This corresponds to the bandwidth of the bandpass transmitted signal. The baseband bandwidth is half of that. Doubling the baseband bandwidth to obtain the Nyquist sampling rate, it follows that the Nyquist rate is

$$f_s = BW = \frac{M}{T_g} . \tag{5.26}$$

Let  $s_k(t)$  be sampled only over the message portion of the  $k^{\text{th}}$  OFDM block. Since the time spacing between the samples is

$$\Delta t_s = \frac{1}{f_s} = \frac{T_g}{M} , \tag{5.27}$$

$M$  samples are required to cover the message portion of the  $k^{\text{th}}$  block. The sampling instants are given by

$$t_i = kT + i \Delta t_s = kT + \frac{i T_g}{M} ; i = 0, 1, \dots, (M-1) . \tag{5.28}$$

With reference to Equation (5.21), the  $i^{\text{th}}$  sample of  $s_k(t)$  becomes

$$\begin{aligned}
 s_k(t_i) \equiv s_{k,i} &= B \sum_{m=0}^{M-1} S_{k,m} e^{j2\pi f_m \left(kT + \frac{i T_g}{M} - kT\right)} \\
 &= B \sum_{m=0}^{M-1} S_{k,m} e^{j2\pi \frac{m}{T_g} \left(i \frac{T_g}{M}\right)} = B \sum_{m=0}^{M-1} S_{k,m} e^{j2\pi \frac{m}{M} i} .
 \end{aligned} \tag{5.29}$$

It follows that the  $M$  time samples ( $i=0, 1, \dots, (M-1)$ ) can be generated by performing the inverse discrete Fourier transform (IDFT) of the  $M$  modulation symbols of the  $k^{\text{th}}$  OFDM block,  $S_{k,m}$ , where  $m=0, 1, \dots, (M-1)$ . Of course, fast Fourier transform techniques can be used to implement the IDFT. This provides significant simplification for the transmitter. Given the  $M$  time samples,  $s_k(t)$  is readily generated using the usual reconstruction techniques based upon the sampling theorem.  $s_k(t)$  is then used to modulate a carrier waveform at the desired carrier frequency.

At the receiver the modulated carrier is converted to baseband in the usual way to produce  $s_k(t)$ .  $s_k(t)$  is then sampled to generate the  $M$  time samples  $s_{k,i} = s_k(t_i)$  where  $i=0, 1, \dots, (M-1)$ . The message symbols are then recovered by utilizing the discrete Fourier transform (DFT) such that

$$S_{k,m} = \frac{1}{B} \sum_{i=0}^{M-1} s_{k,i} e^{-j2\pi \frac{i}{M} m} . \quad (5.30)$$

As with the transmitter, fast Fourier transform techniques can be used to implement the DFT. This considerably simplifies implementation of the receiver.

When the subcarrier spacing,  $\Delta f$ , is designed to be much smaller than the channel coherence bandwidth and the symbol duration  $T$  is much smaller than the channel coherence time, the channel transfer function,  $H(f,t)$ , can be approximated by a complex constant within the bandwidth of each subcarrier signal and the duration of each modulation symbol. In such a situation, the effect of the radio channel is a simple multiplication of each subcarrier signal,  $S_{k,m} g_m(t-kT)$ , by the complex transfer constant,  $H_{k,m} = H(m\Delta f, kT)$ .

As a result, the  $k^{\text{th}}$  OFDM block results in the received signal

$$r_k(t) = \sum_{m=0}^{M-1} S_{k,m} H_{k,m} g_m(t-kT) + n_k(t) \quad (5.31)$$

where  $n_k(t)$  denotes the additive noise. As illustrated in Figure 5.1, intersymbol interference is avoided provided the guard interval length,  $T_g$ , is larger than the maximum multipath delay,  $\tau_m$ . Therefore, correlation can be used to recover the separate symbols associated with each subcarrier. Specifically,

$$R_{k,m} = \frac{1}{B^2 T_g} \int_{kT}^{(k+1)T - T_g} r_k(t) g_m^*(t-kT) dt . \quad (5.32)$$

Alternatively, the DFT could be used. During the  $k^{\text{th}}$  block time interval,

$$kT - T_g \leq t \leq (k+1)T - T_g , \quad (5.22)$$

the received waveform is

$$r_k(t) = \sum_{m=0}^{M-1} S_{k,m} H_{k,m} B e^{j2\pi f_m(t-kT)} + n_k(t) . \quad (5.33)$$

Sampling  $r_k(t)$  at the  $M$  sampling instants specified by Equation (5.28), yields the  $M$  time samples

$$r_k(t_i) = B \sum_{m=0}^{M-1} S_{k,m} H_{k,m} e^{j2\pi \frac{m}{M} i} + n_k(t_i) . \quad (5.34)$$

Application of the DFT to these  $M$  time samples generates

$$\begin{aligned} R_{k,m} &= \frac{1}{B} \sum_{i=0}^{M-1} r_k(t_i) e^{-j2\pi \frac{i}{M} m} \\ &= S_{k,m} H_{k,m} + N_{k,m} \end{aligned} \quad (5.35)$$

where

$$N_{k,m} = \frac{1}{B} \sum_{i=0}^{M-1} n_k(t_i) e^{-j2\pi \frac{i}{M} m} \quad (5.36)$$

denotes the scaled additive noise Fourier coefficients.

The above detection schemes imply perfect synchronization at the receiver. Time and frequency synchronization errors disturb the orthogonality of the subcarriers which can considerably impair performance.

A general block diagram of the OFDM communication system discussed above is shown in Figure 5.2. The S/P and P/S blocks indicate serial-to-parallel and parallel-to-serial encoders, respectively. IFFT and FFT refer to the inverse fast Fourier and fast Fourier transforms, respectively. The bit interleaver is used to scramble the bits so as to mitigate error bursts. In addition, convolutional encoding, which is readily decoded by the Viterbi algorithm, is performed on the data.

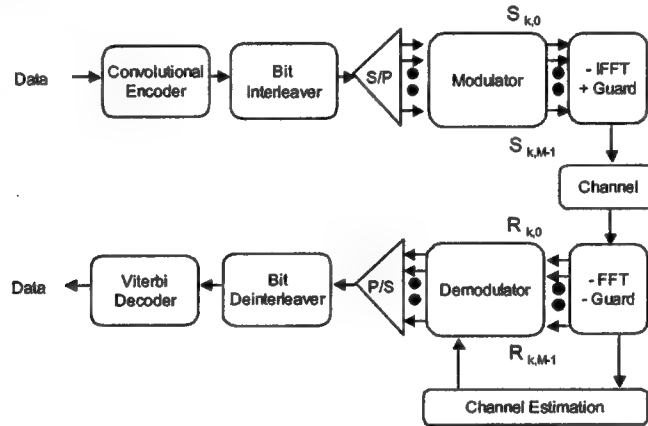


**Figure 5.2:** An OFDM communication system typically employs fast Fourier transform techniques, coding, and channel estimation.

### 5.1.5 Modulation and Demodulation Without Differential Encoding

As mentioned in Section 5.1.2, each subcarrier can be modulated independently with the complex modulation symbol,  $S_{k,m}$ . Generally, this complex value is generated using multilevel signaling whereby a sequence of  $p$  binary bits is mapped into one of  $2^p$  possible symbols.

If no differential encoding is applied, the data bits to be transmitted are directly mapped to the modulation symbols,  $S_{k,m}$ .  $M$ -ary phase-shift keying (MPSK) and  $M$ -ary quadrature amplitude modulation (MQAM) are examples of this modulation technique.

Coherent demodulation has to be applied when nondifferential modulation is used in the transmitter. Typically, this means that the mixer in the receiver is synchronized in both frequency and phase with the carrier frequency of the received signal. However, in the case of an OFDM transmission system, each subcarrier has to be synchronized in both frequency and phase. Also, if any kind of amplitude modulation, such as MQAM, is used in the transmitter, the attenuation of each subcarrier must be known.

To generate this information in the receiver, channel estimation needs to be performed which provides estimates,  $\hat{H}_{k,m}$ , of the channel transfer constants. Given

$$R_{k,m} = S_{k,m} H_{k,m} + N_{k,m} , \quad (5.35)$$

the decision is based on the statistic

$$D_{k,m}^C = \frac{R_{k,m}}{\hat{H}_{k,m}} = \frac{H_{k,m}}{\hat{H}_{k,m}} S_{k,m} + \frac{N_{k,m}}{\hat{H}_{k,m}} . \quad (5.37)$$

$\hat{S}_{k,m}$ , an estimate of the transmitted signal, is determined by noting the region of the decision space containing  $D_{k,m}^C$ . This decision procedure is indicated by

$$\hat{S}_{k,m} = \text{dec}\{D_{k,m}^C\} . \quad (5.38)$$

The estimate,  $\hat{H}_{k,m}$ , is obtained by using known pilot symbols which are inserted into the OFDM signal before transmission. The first step for the receiver is to extract the transfer constants at those times and frequencies at which the pilot symbols were transmitted. Interpolation is then used to estimate the transfer constants corresponding to particular values of  $k$  and  $m$ .

#### 5.1.6 Modulation and Demodulation With Differential Encoding

Differential encoding for narrowband channels means that the transmitted information is contained in the quotient of two successive modulation symbols. Therefore, the data bits to be transmitted are not mapped directly to the modulation symbols,  $S_{k,m}$ . Instead the quotient of two successively transmitted modulation symbols is designed to contain the data bit information.

This technique can be applied either with respect to time or frequency. In the time direction the operation of differential encoding is described analytically by

$$S_{k,m} = S_{k-1,m} \times C_{k,m} \quad (5.39)$$

where the  $p$  binary bits are first used to determine  $C_{k,m}$ .  $S_{k,m}$  is then determined by carrying out the product between  $C_{k,m}$  and  $S_{k-1,m}$ . Alternatively, differential encoding in the frequency direction is summarized by the product

$$S_{k,m} = S_{k,m-1} \times C_{k,m} . \quad (5.40)$$

As before, the  $p$  binary bits are first used to determine  $C_{k,m}$ .  $S_{k,m}$  is then calculated from the product.

In both cases the coherence time and coherence bandwidth of the channel need to be large compared to the symbol duration and subcarrier spacing, respectively, to ensure that the corresponding channel transfer constants,  $H_{k,m}$ , are adequate measures of the channel behavior. Cases are encountered in communication systems where differential encoding in the frequency direction has some advantages with respect to the system overhead needed to monitor the channel.

The topic of demodulation is now discussed. For this purpose, only differential encoding in the time direction is considered. When differential encoding is employed in the transmitter, demodulation at the receiver can be carried out noncoherently. From Equation (5.35)  $R_{k,m}$  and  $R_{k-1,m}$  are given by

$$\begin{aligned} R_{k,m} &= S_{k,m} H_{k,m} + N_{k,m} , \\ R_{k-1,m} &= S_{k-1,m} H_{k-1,m} + N_{k-1,m} . \end{aligned} \quad (5.41)$$

Employing Equation (5.39) in the expression for  $R_{k,m}$ , there results

$$R_{k,m} = S_{k-1,m} C_{k,m} H_{k,m} + N_{k,m} . \quad (5.42)$$

The quotient of  $R_{k,m}$  and  $R_{k-1,m}$  yields the statistic



$$\begin{aligned}
D_{k,m}^{nc} &= \frac{R_{k,m}}{R_{k-1,m}} = \frac{S_{k-1,m} C_{k,m} H_{k,m} + N_{k,m}}{S_{k-1,m} H_{k-1,m} + N_{k-1,m}} \\
&= \frac{S_{k-1,m} C_{k,m} H_{k,m} \left[ 1 + \frac{N_{k,m}}{S_{k-1,m} C_{k,m} H_{k,m}} \right]}{S_{k-1,m} H_{k-1,m} \left[ 1 + \frac{N_{k-1,m}}{S_{k-1,m} H_{k-1,m}} \right]} \quad (5.43)
\end{aligned}$$

In practice, successive channel transfer constants are strongly correlated such that

$$H_{k,m} \approx H_{k-1,m} \quad (5.44)$$

If, in addition, the noise is negligible such that

$$\begin{aligned}
\left| \frac{N_{k,m}}{S_{k-1,m} C_{k,m} H_{k,m}} \right| &\ll 1, \\
\left| \frac{N_{k-1,m}}{S_{k-1,m} H_{k-1,m}} \right| &\ll 1,
\end{aligned} \quad (5.45)$$

the statistic simplifies to

$$D_{k,m}^{nc} \approx C_{k,m} \quad (5.46)$$

An estimate of the message symbol,  $C_{k,m}$ , is obtained by noting the region of the decision space containing  $D_{k,m}^{nc}$ . This decision procedure is indicated by

$$\hat{C}_{k,m} = \text{dec}\{D_{k,m}^{nc}\} \quad (5.47)$$

Note that channel estimation does not have to be performed with the noncoherent demodulation scheme discussed above. Thus, the computational complexity of the receiver is relatively low. Unfortunately, the noncoherent statistic of Equation (5.46) is affected by twice as much noise power as the coherent statistic of Equation (5.37). This results in a higher bit error rate than does the coherent demodulation approach with good channel state information.

Another approach to detection, called quasi-coherent demodulation, involves both differential encoding and coherent demodulation. From Equation (5.39)

$$C_{k,m} = \frac{S_{k,m}}{S_{k-1,m}} \quad (5.48)$$

Coherent demodulation, as specified in Equation (5.38), is used to obtain estimates of  $S_{k,m}$  and  $S_{k-1,m}$ . The quasi-coherent detection statistic is then given by

$$D_{k,m}^{qc} = \frac{\hat{S}_{k,m}}{\hat{S}_{k-1,m}} = \frac{\text{dec} \left\{ \frac{R_{k,m}}{\hat{H}_{k,m}} \right\}}{\text{dec} \left\{ \frac{R_{k-1,m}}{\hat{H}_{k-1,m}} \right\}} . \quad (5.49)$$

In this way, the channel influence is removed before differential decoding takes place. As with the other detection procedures, the estimate of the message symbol,  $C_{k,m}$ , is determined by noting the region of the decision space containing  $D_{k,m}^{qc}$  and is indicated by writing

$$\hat{C}_{k,m} = \text{dec} \{ D_{k,m}^{qc} \} . \quad (5.50)$$

Apart from differential decoding, the processing in a quasi-coherent receiver is similar to that in a coherent one. However, because of differential encoding, an incorrect decision influences two successive symbols. Provided that the error rate is relatively small (i.e., less than 10%), it has been shown that the error probability with quasi-coherent demodulation is approximately twice that of coherent detection with perfect channel estimation.

### 5.1.7 M-ary Differential Amplitude and Phase Shift Keying

M-ary differential amplitude and phase shift keying (M-DAPSK) has been promoted as an effective modulation technique for achieving higher bandwidth efficiency. In fact, M-DAPSK has been shown to have a substantial performance improvement over M-ary differential phase shift keying (M-DPSK) for  $M \geq 16$ .

Before delving into M-DAPSK, M-ary amplitude and phase shift keying (M-APSK) is discussed first. Assume  $p$  input bits are used to determine each symbol. However, let  $p_a$  of these bits determine the amplitude of each symbol while  $p_p$  of these bits are used to specify the symbol phase. Note that

$$p = p_a + p_p , \quad (5.51)$$

the number of possible amplitudes is

$$N_a = 2^{p_a} , \quad (5.52)$$

the number of possible phases is

$$N_p = 2^{p_p} , \quad (5.53)$$

and the total number of symbols (or signal states) is

$$M_s = 2^p = 2^{p_a + p_p} = N_a N_p . \quad (5.54)$$

As an example, let  $p = 6$ ,  $p_a = 2$ , and  $p_p = 4$ . This results in 4 amplitudes, 16 phases, and a total of 64 symbols. A 64-APSK signal space is shown in Figure 5.3. The signal constellation consists of four different amplitude rings, each with 16 phase states. The amplitude values of the rings are 1,  $a$ ,  $a^2$ , and  $a^3$ . Hence, successive rings have amplitudes which differ by the constant factor,  $a$ . In general, the signal space diagram for M-APSK can be described by the signal set

$$\Psi = \left\{ a^A e^{j \frac{2\pi}{N_p} P} \right\} \quad (5.55)$$

where  $A$  and  $P$  are integers selected from the sets

$$\begin{aligned} A &= \{0, 1, \dots, (N_a - 1)\} \\ P &= \{0, 1, \dots, (N_p - 1)\} \end{aligned} \quad (5.56)$$

such that  $N_a$  and  $N_p$  satisfy Equation (5.54).

M-ary DAPSK is a logical extension of M-ary APSK. The  $p$  data bits for M-DAPSK first determine the message symbol,  $C_{k,m}$ . Let  $A(C_{k,m})$  and  $P(C_{k,m})$  denote integers selected from the sets  $A$  and  $P$  of Equation (5.56). The message symbol is then given by

$$C_{k,m} = a^{A(C_{k,m})} e^{j \frac{2\pi}{N_p} P(C_{k,m})} \quad (5.57)$$

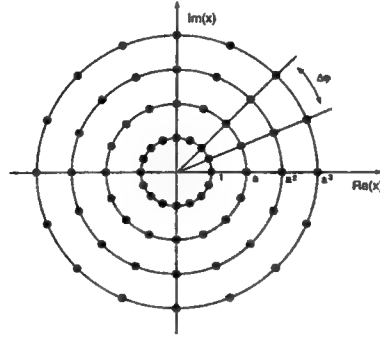


Figure 5.3: The signal space contains 64 possible symbols when there are 4 possible amplitudes and 16 possible phases.

Differential encoding generates the transmitted signal,  $S_{k,m}$ , according to Equation (5.39). Note that  $S_{k-1,m}$  is of the form

$$S_{k-1,m} = a^{A(S_{k-1,m})} e^{j \frac{2\pi}{N_p} P(S_{k-1,m})} \quad (5.58)$$

where  $A(S_{k-1,m})$  and  $P(S_{k-1,m})$  are, also, integers selected from the sets  $A$  and  $P$ . When  $S_{k-1,m}$  and  $C_{k,m}$  are multiplied, the amplitude exponents are added as are the phase exponents. However, to assure that  $S_{k,m}$  is contained in the set,  $\Psi$ , it is necessary to add  $A(S_{k-1,m})$  and  $A(C_{k,m})$  modulo  $N_a$ . Because of the inherent periodicity in the phase, it is not strictly necessary to add  $P(S_{k-1,m})$  and  $P(C_{k,m})$  modulo  $N_p$ . As a result, the transmitted symbol is

$$S_{k,m} = a^{[A(S_{k-1,m}) + A(C_{k,m})] \bmod N_a} \times e^{j \frac{2\pi}{N_p} [P(S_{k-1,m}) + P(C_{k,m})]} \quad (5.59)$$

By way of example, consider the signal space diagram of Figure 5.3 for which  $p = 6$ ,  $p_a = 2$ , and  $p_p = 4$ . Assume the first two message bits are used to determine the amplitude of  $C_{k,m}$  in accordance with

$$00 \rightarrow 1, \quad 01 \rightarrow a, \quad 11 \rightarrow a^2, \quad 10 \rightarrow a^3 \quad (5.60)$$

The remaining four bits determine the phase of  $C_{k,m}$ . Table 5.1 shows the magnitude of  $S_{k,m}$  as a function of the magnitude of  $S_{k-1,m}$  and the transformation indicated by Equation (5.60). Observe that  $|S_{k,m}|$  equals  $|C_{k,m}|$  when  $|S_{k-1,m}|$  is unity.

TABLE 5.1  
DIFFERENTIAL AMPLITUDE MODULATION FOR  $p_a = 2$

$ S_{k-1,m} $		$ S_{k,m} $			
1		1	a	$a^2$	$a^3$
a		a	$a^2$	$a^3$	1
$a^2$		$a^2$	$a^3$	1	a
$a^3$		$a^3$	1	a	$a^2$
AMPLITUDE BITS		00	01	11	10

Given a value of  $p$ , the optimal values for  $p_a$  and  $p_p$  so as to minimize the bit error rate when employing differential encoding are given in Table 5.2. When  $p < 4$  (or, equivalently,  $M_s < 16$ ), observe that differential phase shift keying is preferred where all symbols have the same amplitude.

TABLE 5.2  
OPTIMAL MODULATION PARAMETERS FOR DIFFERENTIAL ENCODING

$p/M_s$	$p_a/N_a$	$p_p/N_p$	Noncoherent Demodulation a	Quasi-Coherent Demodulation a
$<4/16$	0/1	$p/M_s$	1.0	1.0
4/16	1/2	3/8	2.0	1.8
5/32	1/2	4/16	1.6	1.45
6/64	2/4	4/16	1.4	1.38
7/128	2/4	5/32	1.3	1.21

It is possible to eliminate the modulo operation on the sum of the amplitude exponents by, in effect, integrating it into the amplitude mapping. For this purpose, let the transmitted symbol be given by

$$S_{k,m} = S_{k-1,m} C'_{k,m} \quad (5.61)$$

Define the extended set of integers given by

$$A' = \{(-N_a+1), (-N_a+2), \dots, -1, 0, 1, \dots, (N_a-1)\} . \quad (5.62)$$

Let  $A'(C'_{k,m})$  be an integer selected from  $A'$  and, as before, let  $P(C'_{k,m})$  be an integer selected from the set,  $P$ .  $C'_{k,m}$  is then defined by

$$C'_{k,m} = a^{A'(C'_{k,m})} e^{j \frac{2\pi}{N_p} P(C'_{k,m})} . \quad (5.63)$$

The integer selected for  $A'(C'_{k,m})$  depends both upon the  $p_a$  data bits and  $|S_{k-1,m}|$ . It is chosen in such a manner that

$$|S_{k,m}| = a^{[A(S_{k-1,m}) + A'(C'_{k,m})]} \quad (5.64)$$

is either 1,  $a$ ,  $a^2$ , ...,  $a^{(N_a-2)}$ ,  $a^{(N_a-1)}$ . By way of example, consider, once again, the signal space diagram of Figure 5.3. Table 5.3 shows the magnitudes of  $C'_{k,m}$  and  $S_{k,m}$  as a function of the magnitude of  $S_{k-1,m}$  and the amplitude data bits. Observe that

$$|C'_{k,m}| = \frac{|S_{k,m}|}{|S_{k-1,m}|} \quad (5.65)$$

as was the case with modulo arithmetic. However the amplitude bits are now decoded by recognizing that

$$\begin{aligned} |C'_{k,m}| = 1 &\rightarrow 00 \\ |C'_{k,m}| = a &\text{ or } 1/a^3 \rightarrow 01 \\ |C'_{k,m}| = a^2 &\text{ or } 1/a^2 \rightarrow 11 \\ |C'_{k,m}| = a^3 &\text{ or } 1/a \rightarrow 10 \end{aligned} \quad (5.66)$$

TABLE 5.3  
DIFFERENTIAL AMPLITUDE MODULATION FOR  $p_a = 2$

$ S_{k-1,m} $	$ C'_{k,m} $				$ S_{k,m} $			
1	1	a	a <sup>2</sup>	a <sup>3</sup>	1	a	a <sup>2</sup>	a <sup>3</sup>
a	1	a	a <sup>2</sup>	1/a	a	a <sup>2</sup>	a <sup>3</sup>	1
a <sup>2</sup>	1	a	1/a <sup>2</sup>	1/a	a <sup>2</sup>	a <sup>3</sup>	1	a
a <sup>3</sup>	1	1/a <sup>3</sup>	1/a <sup>2</sup>	1/a	a <sup>3</sup>	1	a	a <sup>2</sup>
AMPLITUDE BITS	00	01	11	10	00	01	11	10

Table 5.4 summarizes the mapping specified in Equation (5.66) and gives thresholds that would be employed in the detection process. Due to the division of two successively received noisy symbols, the exact thresholds for noncoherent demodulation are hard to calculate. However, a good approximation is given by the geometric average of two adjacent valid amplitudes. As a result, the thresholds in Table 5.4 are of the form

$$T_a^{nc} = a^j \sqrt{a}; \quad j = (-N_a + 1), \dots, 0, \dots, (N_a - 2) \quad (5.67)$$

The thresholds used to obtain the phase information bits are given by half the distance between two adjacent valid phases. Hence,

$$T_p^{nc} = \left( \frac{1}{2} + i \right) \frac{2\pi}{N_p}; \quad i = 0, 1, \dots, (N_p - 1) \quad (5.68)$$

TABLE 5.4  
THRESHOLDING SCHEME FOR EVALUATION OF AMPLITUDE  
INFORMATION BITS

$ C'_{k,m} $		$a^{-3}$	$a^{-2}$	$a^{-1}$	1	a	$a^2$	$a^3$
AMPLITUDE BITS		01	11	10	00	01	11	10
THRESHOLDS		$a^{-2.5}$	$a^{-1.5}$	$a^{-0.5}$	$a^{0.5}$	$a^{1.5}$	$a^{2.5}$	$a^{3.5}$

In the case of quasi-coherent demodulation with independent identically distributed symbols, the optimum thresholds are identical to those used with coherent demodulation. In particular, they are half the distance between two adjacent valid phases or amplitudes. Thus,

$$T_a^{qc} = T_a^c = a^j \frac{(1+a)}{2}; \quad j = 0, 1, \dots, (N_a - 2) \quad (5.69)$$

$$T_p^{qc} = T_p^c = T_p^{nc} = \left( \frac{1}{2} + i \right) \frac{2\pi}{N_p}; \quad i = 0, 1, \dots, (N_p - 1)$$

As indicated in Figure 5.2, channel coding should be implemented with OFDM. The radio channel attenuates each OFDM subcarrier by the complex transfer constant,  $H_{k,m}$ . If the channel is a multipath channel with many propagation paths and without a line-of-sight path, the amplitude of the transfer constants is Rayleigh. This means that, even at a very large average signal-to-noise ratio, there are always some subcarriers that are strongly attenuated and have a rather low signal-to-noise ratio. Hence, many bit errors would occur on these subcarriers. For this reason, channel coding is a very important component of OFDM systems. Soft decision decoding has been shown to be superior to hard decision decoding. A soft decision algorithm first decides the result based upon the statistic being above or below a decision threshold and then gives a "confidence" number that specifies how close the text statistic is to the threshold value. In hard decisions only the decision output is known. The Viterbi decoding algorithm examines the possible paths through a code tree and selects the best one based on some conditional probabilities.

## 5.2 Ambiguity Function of the OFDM Signal

The delay-Doppler ambiguity function of the interferometer waveform is defined in Equation (2.61) as

$$\Gamma(\tau, \nu) = \int_{-\infty}^{\infty} f_{\text{IFM}}^*(\sigma) f_{\text{IFM}}(\sigma - \tau) e^{j2\pi\nu\sigma} d\sigma. \quad (2.61)$$

Because of the odd symmetry for an ambiguity function, indicated by Equation (4.23), it is necessary to consider only nonnegative values of  $\tau$  and  $\nu$ .

Having chosen the interferometer signal to be the OFDM signal specified by Equation (5.13) and (5.3), the ambiguity function becomes

$$\Gamma(\tau, \nu) = \frac{1}{KMT_s B^2 \sigma_s^2} \int_{-\infty}^{\infty} \left\{ \sum_{k=0}^{K-1} \sum_{m=0}^{M-1} S_{k,m}^* g_m^*(\sigma - kT_s) \right\} \left\{ \sum_{\ell=0}^{K-1} \sum_{n=0}^{M-1} S_{\ell,n} g_n(\sigma - \tau - \ell T_s) \right\} e^{j2\pi\nu\sigma} d\sigma. \quad (5.70)$$

Interchanging the order of summation and integration results in

$$\Gamma(\tau, \nu) = \frac{1}{KMT_s B^2 \sigma_s^2} \sum_{k=0}^{K-1} \sum_{m=0}^{M-1} \sum_{\ell=0}^{K-1} \sum_{n=0}^{M-1} S_{k,m}^* S_{\ell,n} \int_{-\infty}^{\infty} g_m^*(\sigma - kT_s) g_n(\sigma - \tau - \ell T_s) e^{j2\pi\nu\sigma} d\sigma. \quad (5.71)$$

The four-fold summation in Equation (5.71) can be grouped into terms for four cases:

1)  $k = \ell, m = n$ , 2)  $k = \ell, m \neq n$ , 3)  $k \neq \ell, m = n$ , and 4)  $k \neq \ell, m \neq n$ . This yields

$$\begin{aligned} \Gamma(\tau, \nu) KMT_s B^2 \sigma_s^2 &= \sum_{k=0}^{K-1} \sum_{m=0}^{M-1} |S_{k,m}|^2 \int_{-\infty}^{\infty} g_m^*(\sigma - kT_s) g_m(\sigma - \tau - kT_s) e^{j2\pi\nu\sigma} d\sigma \\ &+ \sum_{k=0}^{K-1} \sum_{m=0}^{M-1} \sum_{\substack{n=0 \\ m \neq n}}^{M-1} S_{k,m}^* S_{k,n} \int_{-\infty}^{\infty} g_m^*(\sigma - kT_s) g_n(\sigma - \tau - kT_s) e^{j2\pi\nu\sigma} d\sigma \\ &+ \sum_{k=0}^{K-1} \sum_{m=0}^{M-1} \sum_{\substack{\ell=0 \\ k \neq \ell}}^{K-1} S_{k,m}^* S_{\ell,m} \int_{-\infty}^{\infty} g_m^*(\sigma - kT_s) g_m(\sigma - \tau - \ell T_s) e^{j2\pi\nu\sigma} d\sigma \\ &+ \sum_{k=0}^{K-1} \sum_{m=0}^{M-1} \sum_{\substack{\ell=0 \\ k \neq \ell, m \neq n}}^{K-1} \sum_{n=0}^{M-1} S_{k,m}^* S_{\ell,n} \int_{-\infty}^{\infty} g_m^*(\sigma - kT_s) g_n(\sigma - \tau - \ell T_s) e^{j2\pi\nu\sigma} d\sigma. \end{aligned} \quad (5.72)$$

Recall that the modulation symbols,  $S_{k,m}$  are selected randomly depending upon the data to be transmitted. Consequently,  $\Gamma(\tau, v)$  is a random function of the modulation symbols. Assuming statistical independence from one symbol to another and stationarity, the statistical average of Equation (5.72) involves expectations of the form  $E[|S_{k,m}|^2]$ ,  $E[S_{k,m}^*]$ , and  $E[S_{k,m}]$ . From Equation (5.11)

$$E[|S_{k,m}|^2] = \sigma_s^2 \quad (5.11)$$

In addition, assuming circular symmetry for the symbol constellation, such as shown in Figure 5.3,

$$E[S_{k,m}^*] = E[S_{k,m}] = 0 \quad (5.73)$$

It follows that

$$\begin{aligned} E[S_{k,m}^* S_{k,n}] &= E[S_{k,m}^*] E[S_{k,n}] = 0 ; m \neq n \\ E[S_{k,m}^* S_{\ell,m}] &= E[S_{k,m}^*] E[S_{\ell,m}] = 0 ; k \neq \ell \\ E[S_{k,m}^* S_{\ell,n}] &= E[S_{k,m}^*] E[S_{\ell,n}] = 0 ; k \neq \ell, m \neq n \end{aligned} \quad (5.74)$$

Consequently, taking the expected value of Equation (5.72) results in

$$E[\Gamma(\tau, v)] = \frac{1}{KMT_s B^2} \sum_{k=0}^{K-1} \sum_{m=0}^{M-1} \int_{-\infty}^{\infty} g_m^*(\sigma - kT_s) g_m(\sigma - \tau - kT_s) e^{j2\pi v \sigma} d\sigma \quad (5.75)$$

The expression in Equation 5.75 is further simplified by making the change of variables

$$\rho = \sigma - kT_s \quad (5.76)$$

Then

$$\begin{aligned} E[\Gamma(\tau, v)] &= \frac{1}{KMT_s B^2} \sum_{k=0}^{K-1} \sum_{m=0}^{M-1} \int_{-\infty}^{\infty} g_m^*(\rho) g_m(\rho - \tau) e^{j2\pi v (\rho + kT_s)} d\rho \\ &= \frac{1}{KMB^2} \sum_{k=0}^{K-1} \sum_{m=0}^{M-1} e^{j2\pi v kT_s} \psi_{mm}(\tau, v) \end{aligned} \quad (5.77)$$

where the autocorrelation function of  $g_m(t)$  was defined to be

$$\psi_{mm}(\tau, v) = \frac{1}{T_s} \int_{-\infty}^{\infty} g_m^*(\rho) g_m(\rho - \tau) e^{j2\pi v \rho} d\rho \quad (5.78)$$

Note that Equations (5.3) and (5.78) are identical in form to Equations (4.17) and (4.29), respectively. It follows from Equation (4.35) that

$$\psi_{mm}(\tau, v) = \begin{cases} B^2 \frac{(T_s - |\tau|)}{T_s} \frac{\sin[\pi v (T_s - |\tau|)]}{\pi v (T_s - |\tau|)} e^{j[\pi v (T_s + \tau) - 2\pi f_m \tau]} , & |\tau| \leq T_s \\ 0 & |\tau| > T_s \end{cases} \quad (5.79)$$



Observe that

$$\psi_{mn}(0,0) = B^2 . \quad (5.80)$$

Therefore, as would be expected due to our normalization,

$$E[\Gamma(0,0)] = 1 . \quad (5.81)$$

Although the terms corresponding to the expectations in Equation (5.74) average to zero, they contribute to significant fluctuations of the ambiguity function over the  $\tau$ - $\nu$  plane. A measure of these fluctuations is the variance of  $\Gamma(\tau, \nu)$ . By definition, this is given by

$$\text{Var}\{\Gamma(\tau, \nu)\} = E[|\Gamma(\tau, \nu)|^2] - |E[\Gamma(\tau, \nu)]|^2 . \quad (5.82)$$

$E[\Gamma(\tau, \nu)]$  is found from Equation (5.77). Therefore, it remains to determine  $E[|\Gamma(\tau, \nu)|^2]$ . For this purpose, it is convenient to return to Equation (5.71).

Making the change of variables

$$\rho = \sigma - kT_s \quad (5.76)$$

in Equation (5.71), it follows that

$$\begin{aligned} & \int_{-\infty}^{\infty} g_m^*(\sigma - kT_s) g_n(\sigma - \tau - \ell T_s) e^{j2\pi\nu\sigma} d\sigma \\ &= e^{j2\pi\nu kT_s} \int_{-\infty}^{\infty} g_m^*(\rho) g_n[\rho - \tau - (\ell - k)T_s] e^{j2\pi\nu\rho} d\rho \\ &= T_s e^{j2\pi\nu kT_s} \psi_{mn}[\tau + (\ell - k)T_s, \nu] \end{aligned} \quad (5.83)$$

where the cross-correlation function between  $g_m(t)$  and  $g_n(t)$  is defined to be

$$\psi_{mn}(\tau, \nu) = \frac{1}{T_s} \int_{-\infty}^{\infty} g_m^*(\rho) g_n(\rho - \tau) e^{j2\pi\nu\rho} d\rho . \quad (5.84)$$

Note that Equations (5.3) and (5.84) are identical in form to Equations (4.17) and (4.31), respectively. It follows from Equation (4.39) that

$$\psi_{mn}(\tau, \nu) = \begin{cases} B^2 \frac{(T_s - |\tau|)}{T_s} \frac{\sin[\pi\alpha_{mn}(T_s - |\tau|)]}{\pi\alpha_{mn}(T_s - |\tau|)} e^{-j[\pi\alpha_{mn}(T_s + \tau) + 2\pi f_n \tau]} , & |\tau| \leq T_s \\ 0 , & |\tau| \geq T_s \end{cases} \quad (5.85)$$

where  $\alpha_{mn}$  is given by

$$\alpha_{mn} = f_m - f_n - \nu . \quad (4.37)$$

Consequently, Equation (5.71) can be expressed as

$$\Gamma(\tau, v) = \frac{1}{\text{KMB}^2 \sigma_s^2} \sum_{k=0}^{K-1} \sum_{m=0}^{M-1} \sum_{\ell=0}^{K-1} \sum_{n=0}^{M-1} S_{k,m}^* S_{\ell,n} e^{j2\pi v k T_s} \psi_{mn} [\tau + (\ell - k) T_s, v] \quad (5.86)$$

It follows that

$$\begin{aligned} |\Gamma(\tau, v)|^2 &= \Gamma(\tau, v) \Gamma^*(\tau, v) \\ &= \left( \frac{1}{\text{KMB}^2 \sigma_s^2} \right)^2 \sum_{k=0}^{K-1} \sum_{m=0}^{M-1} \sum_{\ell=0}^{K-1} \sum_{n=0}^{M-1} S_{k,m}^* S_{\ell,n} e^{j2\pi v k T_s} \psi_{mn} [\tau + (\ell - k) T_s, v] \\ &\times \sum_{k'=0}^{K-1} \sum_{m'=0}^{M-1} \sum_{\ell'=0}^{K-1} \sum_{n'=0}^{M-1} S_{k',m'} S_{\ell',n'}^* e^{-j2\pi v k' T_s} \psi_{m'n'}^* [\tau + (\ell' - k') T_s, v] \quad (5.87) \\ &= \left( \frac{1}{\text{KMB}^2 \sigma_s^2} \right)^2 \sum_{k=0}^{K-1} \sum_{m=0}^{M-1} \sum_{\ell=0}^{K-1} \sum_{n=0}^{M-1} \sum_{k'=0}^{K-1} \sum_{m'=0}^{M-1} \sum_{\ell'=0}^{K-1} \sum_{n'=0}^{M-1} S_{k,m}^* S_{\ell,n} S_{k',m'} S_{\ell',n'}^* \\ &\times e^{j2\pi v (k - k') T_s} \psi_{mn} [\tau + (\ell - k) T_s, v] \psi_{m'n'}^* [\tau + (\ell' - k') T_s, v] \end{aligned}$$

The expected value of  $|\Gamma(\tau, v)|^2$  is, therefore,

$$\begin{aligned} E[|\Gamma(\tau, v)|^2] &= \left( \frac{1}{\text{KMB}^2 \sigma_s^2} \right)^2 \sum_{k=0}^{K-1} \sum_{m=0}^{M-1} \sum_{\ell=0}^{K-1} \sum_{n=0}^{M-1} \sum_{k'=0}^{K-1} \sum_{m'=0}^{M-1} \sum_{\ell'=0}^{K-1} \sum_{n'=0}^{M-1} \\ &E[S_{k,m}^* S_{\ell,n} S_{k',m'} S_{\ell',n'}^*] e^{j2\pi v (k - k') T_s} \quad (5.88) \\ &\psi_{mn} [\tau + (\ell - k) T_s, v] \psi_{m'n'}^* [\tau + (\ell' - k') T_s, v] \end{aligned}$$

Recall that the modulation symbols,  $S_{k,m}$ , are assumed to be stationary and statistically independent with zero means. Consequently, when  $E[S_{k,m}^* S_{\ell,n} S_{k',m'} S_{\ell',n'}^*]$  can be decomposed into a product for which one or more of the factors is the expectation of a single symbol or its conjugate, the expectation in Equation (5.88) is zero and the corresponding terms can be excluded from the eight-fold summation.

In addition, for some choices of the indices in Equation (5.88),  $E[S_{k,m}^* S_{\ell,n} S_{k',m'} S_{\ell',n'}^*]$  can be decomposed into a product involving factors of the form  $E[S_{k,m}^2]$  and  $E[(S_{k,m}^*)^2]$ . For circularly symmetric signal sets these expectations are, also, zero as explained next.

In general,  $S_{k,m}$  is a complex quantity which can be expressed in polar form as

$$S_{k,m} = A_{k,m} e^{j\theta_{k,m}} . \quad (5.89)$$

Consequently,

$$S_{k,m}^2 = A_{k,m}^2 e^{j2\theta_{k,m}} . \quad (5.90)$$

Assuming  $p_p$  data bits are used to specify the symbol, the number of possible phases is given by Equation (5.53). When the symbol constellation has circular symmetry, such as that in Figure 5.3, the phases are distributed by equal angular increments where the increment is given by

$$\Delta\phi = \frac{2\pi}{2^{p_p}} . \quad (5.91)$$

Beginning with symbols placed on the real positive axis, the symbol angles are given by

$$k\Delta\phi = \frac{2\pi k}{2^{p_p}} ; k=0,1, \dots, (N_p - 1) . \quad (5.92)$$

A total increment of  $\pi$  corresponds to

$$k\Delta\phi = \frac{2\pi k}{2^{p_p}} = \pi . \quad (5.93)$$

This requires that

$$k = 2^{p_p-1} = \frac{N_p}{2} \quad (5.94)$$

which is an integer in the set for  $k$  since  $N_p$  is guaranteed to be an even integer. Therefore, for each symbol in the set, there is a corresponding symbol with the same amplitude but displaced in phase by  $\pi$  radians. This justifies the conclusion that

$$E[e^{j\theta_{k,m}}] = 0 . \quad (5.95)$$

Now consider  $S_{k,m}^2$  for which the angle is given by  $2\theta_{k,m}$ . The symbols corresponding to  $S_{k,m}^2$  are distributed at equal angular increments given by

$$2\Delta\phi = 2\frac{2\pi}{2^{p_p}} = \frac{2\pi}{2^{(p_p-1)}} = \frac{2\pi}{2^{p'_p}} \quad (5.96)$$

where

$$p'_p = p_p - 1 . \quad (5.97)$$

In effect,  $S_{k,m}^2$  is distributed in the same manner as  $S_{k,m}$  except that the number of data bits used to specify the phase of  $S_{k,m}^2$  is reduced by unity. Therefore, the number of distinct phases for  $S_{k,m}^2$  is half of those for  $S_{k,m}$ . Based on these observations, it is concluded that

$$E[e^{j2\theta_{k,m}}] = 0 \quad (5.98)$$

Because the amplitude data bits are statistically independent of the phase data bits, it follows that

$$E[S_{k,m}^2] = E[A_{k,m}^2 e^{j2\theta_{k,m}}] = E[A_{k,m}^2] E[e^{j2\theta_{k,m}}] = 0 \quad (5.99)$$

Also, since the complex conjugate of zero is zero,

$$E[(S_{k,m}^*)^2] = 0 \quad (5.100)$$

Excluding those terms for which  $E[S_{k,m}^* S_{\ell,n} S_{k',m'} S_{\ell',n'}^*]$  is zero, the only remaining terms in the eight-fold summation of Equation (5.88) are those having the form

$E[|S_{k,m}|^4]$  and  $E[|S_{k,m}|^2 |S_{\ell,n}|^2]$  where  $k \neq \ell$  and  $m \neq n$ . These arise in the following ways:

- 1) Let  $k = \ell = k' = \ell'$  and  $m = n = m' = n'$ .

The corresponding terms in Equation (5.88) are given by

$$\left( \frac{1}{KMB^2 \sigma_s^2} \right)^2 \sum_{k=0}^{K-1} \sum_{m=0}^{M-1} E[|S_{k,m}|^4] |\psi_{mm}[\tau, \nu]|^2 \quad (5.101)$$

- 2) Let  $k = \ell$ ,  $m = n$  and  $k' = \ell'$ ,  $m' = n'$  but exclude  $k = \ell = k' = \ell'$  and  $m = n = m' = n'$ . The corresponding terms in Equation (5.88) are given by

$$\begin{aligned} & \left( \frac{1}{KMB^2 \sigma_s^2} \right)^2 \sum_{k=0}^{K-1} \sum_{m=0}^{M-1} \sum_{k'=0}^{K-1} \sum_{m'=0}^{M-1} E[|S_{k,m}|^2] E[|S_{k',m'}|^2] \\ & \quad k \neq k' \text{ \& } m \neq m' \\ & \quad \times e^{j2\pi \nu (k-k')T_s} \psi_{mm}[\tau, \nu] \psi_{m'm'}^*[\tau, \nu] \quad (5.102) \end{aligned}$$

- 3) Let  $k = k'$ ,  $m = m'$  and  $\ell = \ell'$ ,  $n = n'$  but exclude  $k = \ell = k' = \ell'$  and  $m = n = m' = n'$ . The corresponding terms in Equation (5.88) are given by

$$\left( \frac{1}{KMB^2 \sigma_s^2} \right)^2 \sum_{\substack{k=0 \\ k \neq \ell}}^{K-1} \sum_{\substack{m=0 \\ m \neq n}}^{M-1} \sum_{\ell=0}^{K-1} \sum_{n=0}^{M-1} E[S_{k,m}^2] E[S_{\ell,n}^2] \times |\psi_{mn}[\tau + (\ell - k)T_s, v]|^2 \quad (5.103)$$

Letting

$$\mu_4 = E[|S_{k,m}|^4] \quad (5.104)$$

and making use of Equations (5.11), (5.101), (5.102), and (5.103), Equation (5.88) becomes

$$\begin{aligned} E[|\Gamma(\tau, v)|^2] &= \left( \frac{1}{KMB^2 \sigma_s^2} \right)^2 \mu_4 K \sum_{m=0}^{M-1} |\psi_{mm}[\tau, v]|^2 \\ &+ \left( \frac{1}{KMB^2} \right)^2 \sum_{\substack{k=0 \\ k \neq k'}}^{K-1} \sum_{\substack{m=0 \\ m \neq m'}}^{M-1} \sum_{k'=0}^{K-1} \sum_{m'=0}^{M-1} e^{j2\pi v(k-k')T_s} \psi_{mm}[\tau, v] \psi_{m'm'}^*[\tau, v] \\ &+ \left( \frac{1}{KMB^2} \right)^2 \sum_{\substack{k=0 \\ k \neq \ell}}^{K-1} \sum_{\substack{m=0 \\ m \neq n}}^{M-1} \sum_{\ell=0}^{K-1} \sum_{n=0}^{M-1} |\psi_{mn}[\tau + (\ell - k)T_s, v]|^2 \quad (5.105) \end{aligned}$$

With reference to Equation (5.82), it is, also, necessary to evaluate  $|E[\Gamma(\tau, v)]|^2$ . From Equation (5.77) it follows that

$$\begin{aligned} |E[\Gamma(\tau, v)]|^2 &= E[\Gamma(\tau, v)] \{E[\Gamma(\tau, v)]\}^* \\ &= \left( \frac{1}{KMB^2} \right)^2 \sum_{k=0}^{K-1} \sum_{m=0}^{M-1} \sum_{k'=0}^{K-1} \sum_{m'=0}^{M-1} e^{j2\pi v(k-k')T_s} \psi_{mm}[\tau, v] \psi_{m'm'}^*[\tau, v] \\ &= \left( \frac{1}{KMB^2} \right)^2 \sum_{k=0}^{K-1} \sum_{m=0}^{M-1} |\psi_{mm}[\tau, v]|^2 \\ &+ \left( \frac{1}{KMB^2} \right)^2 \sum_{\substack{k=0 \\ k \neq k'}}^{K-1} \sum_{\substack{m=0 \\ m \neq m'}}^{M-1} \sum_{k'=0}^{K-1} \sum_{m'=0}^{M-1} e^{j2\pi v(k-k')T_s} \psi_{mm}[\tau, v] \psi_{m'm'}^*[\tau, v] \quad (5.106) \end{aligned}$$

Combining the results for  $E[|\Gamma(\tau, v)|^2]$  and  $|E[\Gamma(\tau, v)]|^2$  in Equation (5.82) yields

$$\begin{aligned} \text{Var} \{ \Gamma(\tau, \nu) \} &= \frac{1}{K} \left( \frac{1}{MB^2 \sigma_s^2} \right)^2 (\mu_4 - \sigma_s^4) \sum_{m=0}^{M-1} |\psi_{mm}[\tau, \nu]|^2 \\ &+ \left( \frac{1}{KMB^2} \right)^2 \sum_{\substack{k=0 \\ k \neq \ell}}^{K-1} \sum_{\substack{m=0 \\ m \neq n}}^{M-1} \sum_{\ell=0}^{K-1} \sum_{n=0}^{M-1} |\psi_{mn}[\tau + (\ell - k)T_s, \nu]|^2. \end{aligned} \quad (5.107)$$

An obvious choice for  $T_s$  is

$$T_s = T \quad (5.108)$$

where  $T$  is the duration of a subpulse in the Costas single proposed for the radar pulse waveform. Also, let

$$K = M = N \quad (5.109)$$

where  $N$  is the number of subpulses in the Costas single. Then the frequencies of the Costas and OFDM signals become identical and the duration of the OFDM signal equals that of the radar pulse.

Note that Equation (5.77) can be expressed as

$$E[\Gamma(\tau, \nu)] = \Gamma'(\tau, \nu) + \frac{1}{KMB^2} \sum_{\substack{k=0 \\ k \neq m}}^{K-1} \sum_{m=0}^{M-1} \psi_{mm}(\tau, \nu) e^{j2\pi \nu k T_s} \quad (5.110)$$

where

$$\Gamma'(\tau, \nu) = \frac{1}{KMB^2} \sum_{m=0}^{K-1} \psi_{mm}(\tau, \nu) e^{j2\pi \nu m T_s} \quad (5.111)$$

while Equation (4.32) can be expressed as

$$\chi(\tau, \nu) = \chi'(\tau, \nu) + \frac{1}{A^2 N} \sum_{n=0}^{N-1} \sum_{\substack{m=0 \\ m \neq n}}^{N-1} \phi_{nm}[\tau + (m - n)T, \nu] e^{j2\pi \nu n T} \quad (5.112)$$

where

$$\chi'(\tau, \nu) = \frac{1}{A^2 N} \sum_{m=0}^{N-1} \phi_{mm}(\tau, \nu) e^{j2\pi \nu m T} \quad (5.113)$$

As pointed out in Chapter 4, the central peak of the Costas signal ambiguity function is associated with  $\chi'(\tau, \nu)$ . Under the conditions of Equations (5.108) and (5.109)

$$\psi_{\text{mm}}(\tau, \nu) = \frac{B^2}{A^2} \phi_{\text{mm}}(\tau, \nu) \quad . \quad (5.114)$$

Then  $\Gamma'(\tau, \nu)$  becomes equal to  $\chi'(\tau, \nu)$  within a scale factor. This, in turn, implies that the central peaks of the ambiguity functions for the OFDM and Costas signals have identical shapes with identical resolutions in delay and Doppler. Because the non-cooperative bistatic radar does not know a priori in which direction the main radar is pointing, it must perform the difficult task of pulse chasing. However, it is likely to be unsuccessful in completing this task because it will be unable to distinguish between reflections involving either the OFDM or Costas signal. In addition, it will be difficult for the non-cooperative bistatic receiver to separate the OFDM and Costas signals because they contain the same frequencies and, assuming time synchronization, will experience amplitude transitions at the same time instants. As a result, performance of the non-cooperative bistatic radar will be severely degraded. This issue is investigated further in Chapter 6.

## CHAPTER 6

### NON-COOPERATIVE BISTATIC RADAR RECEIVER PERFORMANCE

#### 6.1 Cross Ambiguity Function for the Costas and OFDM Signals

As discussed in Section 2.3, the non-cooperative bistatic radar receiver performs detection by utilizing an estimate of the main radar transmitted signal for correlation with the received data. In this report it is assumed that the estimate is obtained from the direct path signal observed by the bistatic radar. As revealed by Equation (2.63), the detection statistic used by the non-cooperative bistatic radar receiver involves the cross ambiguity function,  $Z(\tau, \nu)$ , between the Costas and OFDM signal in addition to their delay-Doppler ambiguity functions. An expression for  $Z(\tau, \nu)$  is derived in this section.

With reference to Equation (2.54), the cross-ambiguity function is defined to be

$$Z(\tau, \nu) = \int_{-\infty}^{\infty} f_{\text{IFM}}^*(\sigma) f_{\text{RAD}}(\sigma - \tau) e^{j2\pi\nu\sigma} d\sigma \quad (2.54)$$

Substitution of Equations (4.16) and (5.13) into Equation (2.54) yields

$$Z(\tau, \nu) = \frac{1}{AB\sigma_s \sqrt{KMNT_s T}} \int_{-\infty}^{\infty} \left\{ \sum_{k=0}^{K-1} \sum_{m=0}^{M-1} S_{k,m}^* g_m^*(\sigma - kT_s) \right\} \left\{ \sum_{n=0}^{N-1} p_n(\sigma - \tau - nT) \right\} e^{j2\pi\nu\sigma} d\sigma \quad (6.1)$$

Once again, assume the conditions of Equations (5.108) and (5.109). Interchanging the order of summation and integration yields

$$Z(\tau, \nu) = \frac{1}{AB\sigma_s T N \sqrt{N}} \sum_{k=0}^{N-1} \sum_{m=0}^{N-1} \sum_{n=0}^{N-1} S_{k,m}^* \int_{-\infty}^{\infty} g_m^*(\sigma - kT) p_n(\sigma - \tau - nT) e^{j2\pi\nu\sigma} d\sigma \quad (6.2)$$

Making the change of variables

$$\rho = \sigma - kT \quad (6.3)$$

in Equation (6.2), it follows that

$$\begin{aligned} & \int_{-\infty}^{\infty} g_m^*(\sigma - kT) p_n(\sigma - \tau - nT) e^{j2\pi\nu\sigma} d\sigma \\ &= e^{j2\pi\nu kT} \int_{-\infty}^{\infty} g_m^*(\rho) p_n[\rho - \tau - (n-k)T] e^{j2\pi\nu\rho} d\rho \\ &= T e^{j2\pi\nu kT} \theta_{mn}[\tau + (n-k)T, \nu] \end{aligned} \quad (6.4)$$

where the cross-correlation function between  $g_m(t)$  and  $p_n(t)$  is defined to be



$$\theta_{mn}(\tau, v) = \frac{1}{T} \int_{-\infty}^{\infty} g_m^*(\rho) p_n(\rho - \tau) e^{j2\pi v \rho} d\rho . \quad (6.5)$$

Utilizing the same procedure employed to develop Equation (4.39), it follows that

$$\theta_{mn}(\tau, v) = \begin{cases} AB \frac{(T - |\tau|)}{T} \frac{\sin[\pi \alpha_{mn}(T - |\tau|)]}{\pi \alpha_{mn}(T - |\tau|)} e^{-j[\pi \alpha_{mn}(T + \tau) + 2\pi f_n \tau]} , & |\tau| \leq T \\ 0 , & |\tau| \geq T \end{cases} \quad (6.6)$$

where  $\alpha_{mn}$  is given by

$$\alpha_{mn} = f_m - f_n - v . \quad (6.7)$$

Consequently, Equation (6.2) can be expressed as

$$Z(\tau, v) = \frac{1}{AB\sigma_s N\sqrt{N}} \sum_{k=0}^{N-1} \sum_{m=0}^{N-1} \sum_{n=0}^{N-1} S_{k,m}^* e^{j2\pi v kT} \theta_{mn}[\tau + (n - k)T, v] . \quad (6.8)$$

Because the modulation symbols,  $S_{k,m}$ , are selected randomly based upon the data to be transmitted,  $Z(\tau, v)$  is a random function of the modulation symbols. Note that

$$E[Z(\tau, v)] = \frac{1}{AB\sigma_s N\sqrt{N}} \sum_{k=0}^{N-1} \sum_{m=0}^{N-1} \sum_{n=0}^{N-1} E[S_{k,m}^*] e^{j2\pi v kT} \theta_{mn}[\tau + (n - k)T, v] = 0 \quad (6.9)$$

where use was made of equation (5.73). Thus, as seen from Equation (2.63),  $Z(\tau, v)$  behaves as a zero-mean additive noise component of the detection statistic for the non-cooperative bistatic radar.

## 6.2 Non-Cooperative Bistatic Radar Detection Statistic Involving the Costas and OFDM Signals

As expressed in Equation (2.44) the detection statistic for the non-cooperative bistatic receiver is the sum of nine terms where the first four terms are given by Equations (2.51), (2.58), (2.59), and (2.60), respectively. The remaining five terms involve receiver noise and are developed next by carrying out the products indicated in Equation (2.43).

Making use of Equations (2.3), (2.38), (2.39), and (2.40), these five terms can be expressed as

$$I_5 = k_{RAD}^{TP} e^{-j2\pi [f^{DP} \tau^{TP} + f_B \tau + v \tau^{TP} - v \tau]} \int_{-\infty}^{\infty} f_{RAD}(t - \tau^{TP}) [n^{DP}(t - \tau_B + \tau)]^* e^{j2\pi (f^{DP} + v)t} dt , \quad (6.10)$$

$$I_6 = k_{IFM}^{TP} e^{-j2\pi [f^{DP} \tau^{TP} + f_B \tau + v \tau^{TP} - v \tau]} \int_{-\infty}^{\infty} f_{IFM}(t - \tau^{TP}) [n^{DP}(t - \tau_B + \tau)]^* e^{j2\pi (f^{DP} + v)t} dt , \quad (6.11)$$

$$I_7 = e^{-j2\pi [-f_B \tau^{TP} + f_B \tau + v \tau^{TP} - v \tau]} \int_{-\infty}^{\infty} n^{TP}(t) [n^{DP}(t - \tau_B + \tau)]^* e^{-j2\pi (f_B - v)t} dt , \quad (6.12)$$

$$I_8 = \left( k_{\text{RAD}}^{\text{DP}} \right)^* e^{j2\pi [f^{\text{TP}} \tau^{\text{TP}} - f^{\text{TP}} \tau - v \tau^{\text{TP}} + v \tau]} \int_{-\infty}^{\infty} n^{\text{TP}}(t) f_{\text{RAD}}^* (t - \tau^{\text{TP}} + \tau) e^{-j2\pi (f^{\text{TP}} - v)t} dt , \quad (6.13)$$

$$I_9 = \left( k_{\text{IFM}}^{\text{DP}} \right)^* e^{j2\pi [f^{\text{TP}} \tau^{\text{TP}} - f^{\text{TP}} \tau - v \tau^{\text{TP}} + v \tau]} \int_{-\infty}^{\infty} n^{\text{TP}}(t) f_{\text{IFM}}^* (t - \tau^{\text{TP}} + \tau) e^{-j2\pi (f^{\text{TP}} - v)t} dt . \quad (6.14)$$

The statistic can be written as

$$\ell = \ell_s + \ell_I \quad (6.15)$$

where the signal portion of the statistic is

$$\ell_s = I_1 \quad (6.16)$$

and the interference component of the statistic is

$$\ell_I = \sum_{i=2}^9 I_i . \quad (6.17)$$

Recall from Equation (2.39) and (2.40) that  $\tau$  and  $v$  denote the errors experienced in estimating  $\tau_B$  and  $f_B$ , respectively. Perfect estimates are obtained when

$$\tau = v = 0 . \quad (6.18)$$

In order to evaluate the best possible performance of the non-cooperative bistatic radar, it is assumed throughout the remainder of this chapter that Equation (6.18) is valid. The expressions for the nine terms of the detection statistic then simplify to

$$I_1 = k_1 \chi(0,0) , \quad (6.19)$$

$$I_2 = k_2 Z^*(0,0) , \quad (6.20)$$

$$I_3 = k_3 Z(0,0) , \quad (6.21)$$

$$I_4 = k_4 \Gamma(0,0) , \quad (6.22)$$

$$I_5 = k_{\text{RAD}}^{\text{TP}} e^{-j2\pi f^{\text{DP}} \tau^{\text{TP}}} \int_{-\infty}^{\infty} f_{\text{RAD}}(t - \tau^{\text{TP}}) [n^{\text{DP}}(t - \tau_B)]^* e^{j2\pi f^{\text{DP}} t} dt , \quad (6.23)$$

$$I_6 = k_{\text{IFM}}^{\text{TP}} e^{-j2\pi f^{\text{DP}} \tau^{\text{TP}}} \int_{-\infty}^{\infty} f_{\text{IFM}}(t - \tau^{\text{TP}}) [n^{\text{DP}}(t - \tau_B)]^* e^{j2\pi f^{\text{DP}} t} dt , \quad (6.24)$$

$$I_7 = e^{j2\pi f_B \tau^{\text{TP}}} \int_{-\infty}^{\infty} n^{\text{TP}}(t) [n^{\text{DP}}(t - \tau_B)]^* e^{-j2\pi f_B t} dt , \quad (6.25)$$

$$I_8 = \left( k_{\text{RAD}}^{\text{DP}} \right)^* e^{j2\pi f^{\text{TP}} \tau^{\text{TP}}} \int_{-\infty}^{\infty} n^{\text{TP}}(t) f_{\text{RAD}}^* (t - \tau^{\text{TP}}) e^{-j2\pi f^{\text{TP}} t} dt , \quad (6.26)$$

$$I_9 = (k_{IFM}^{DP})^* e^{j2\pi f^{TP} \tau^{TP}} \int_{-\infty}^{\infty} n^{TP}(t) f_{IFM}^*(t - \tau^{TP}) e^{-j2\pi f^{TP} t} dt \quad (6.27)$$

In general, the detection statistic is a complex random variable. However, because the Costas signal is deterministic,  $\chi(0,0)$  is a constant. Utilizing Equation (4.47), it follows that

$$E[\ell_s] = E[I_1] = k_1 \quad (6.28)$$

Thus, the signal portion of the detection statistic is a constant.

With respect to the interference component of the detection statistic, note that

$$E[I_2] = E[I_3] = 0 \quad (6.29)$$

due to Equation (6.9). Also, with reference to Equation (5.81)

$$E[I_4] = k_4 E[\Gamma(0,0)] = k_4 \quad (6.30)$$

Finally, assuming the complex envelopes of the receiver noises in the direct and total paths to be statistically independent with zero means, it follows that

$$E[I_5] = E[I_6] = E[I_7] = E[I_8] = E[I_9] = 0 \quad (6.31)$$

Consequently,

$$E[\ell_1] = k_4 \quad (6.32)$$

Hence, the interference component of the detection statistic is a random variable with a nonzero mean.

The variance of  $\ell_1$  is now derived. By definition,

$$\text{Var}\{\ell_1\} = E[|\ell_1|^2] - |E[\ell_1]|^2 \quad (6.33)$$

Note that

$$|\ell_1|^2 = \ell_1 \ell_1^* = \sum_{i=2}^9 \sum_{j=2}^9 I_i I_j^* \quad (6.34)$$

Therefore,

$$E[|\ell_1|^2] = \sum_{i=2}^9 \sum_{j=2}^9 E[I_i I_j^*] = \sum_{i=2}^9 E[|I_i|^2] + \sum_{i=2}^9 \sum_{\substack{j=2 \\ i \neq j}}^9 E[I_i I_j^*] \quad (6.35)$$

Observe that the double summation in Equation (6.35) contains 64 expectations that need to be evaluated.

To evaluate the expectations involving  $I_2$  and  $I_3$ , it is necessary to obtain an expression for  $Z(0,0)$ . From Equation (6.8)

$$Z(0,0) = \frac{1}{AB\sigma_s N\sqrt{N}} \sum_{k=0}^{N-1} \sum_{m=0}^{N-1} \sum_{n=0}^{N-1} S_{k,m}^* \theta_{mn}[(n-k)T,0] \quad (6.36)$$

where  $\theta_{mn}(\tau,0)$  is given by Equation (6.6). Since  $\theta_{mn}(\tau, v)$  is zero for  $|\tau| \geq T$ , it follows that

$$\theta_{mn}[(n-k)T,0] = 0 \text{ for } n \neq k \quad (6.37)$$

As a result,  $Z(0,0)$  becomes

$$Z(0,0) = \frac{1}{AB\sigma_s N\sqrt{N}} \sum_{k=0}^{N-1} \sum_{m=0}^{N-1} S_{k,m}^* \theta_{mk} [0,0] \quad (6.38)$$

However,

$$\theta_{mk}(0,0) = \begin{cases} AB & , \quad m=k \\ 0 & , \quad m \neq k \end{cases} \quad (6.39)$$

Thus, the expression for  $Z(0,0)$  simplifies to

$$Z(0,0) = \frac{1}{\sigma_s N\sqrt{N}} \sum_{k=0}^{N-1} S_{k,k}^* \quad (6.40)$$

$E[|I_2|^2]$  and  $E[|I_3|^2]$  are evaluated first. Note that

$$E[|I_2|^2] = |k_2|^2 E[|Z(0,0)|^2] \quad (6.41)$$

Utilizing Equation (6.40), it follows that

$$\begin{aligned} E[|Z(0,0)|^2] &= \frac{1}{\sigma_s^2 N^3} \sum_{k=0}^{N-1} \sum_{\ell=0}^{N-1} E[S_{k,k}^* S_{\ell,\ell}] \\ &= \frac{1}{\sigma_s^2 N^3} \left\{ \sum_{k=0}^{N-1} E[|S_{k,k}|^2] + \sum_{k=0}^{N-1} \sum_{\substack{\ell=0 \\ k \neq \ell}}^{N-1} E[S_{k,k}^*] E[S_{\ell,\ell}] \right\} \end{aligned} \quad (6.42)$$

where the statistical independence between different data symbols was invoked. However, the data symbols are random variables with zero mean and variance  $\sigma_s^2$ .

Consequently,

$$E[|Z(0,0)|^2] = \frac{1}{N^2} \quad (6.43)$$

and

$$E[|I_2|^2] = \frac{|k_2|^2}{N^2} \quad (6.44)$$

In a similar manner,

$$E[|I_3|^2] = \frac{|k_3|^2}{N^2} \quad . \quad (6.45)$$

Also,

$$E[I_2 I_3^*] = k_2 k_3^* E\{[Z^*(0,0)]^2\} \quad . \quad (6.46)$$

Use of Equations (6.40) and (5.99) and the statistical independence of the zero mean data symbols results in

$$\begin{aligned} E[I_2 I_3^*] &= \frac{k_2 k_3^*}{\sigma_s^2 N^3} \sum_{k=0}^{N-1} \sum_{\ell=0}^{N-1} E[S_{k,k} S_{\ell,\ell}^*] \\ &= \frac{k_2 k_3^*}{\sigma_s^2 N^3} \left\{ \sum_{k=0}^{N-1} E[S_{k,k}^2] + \sum_{k=0}^{N-1} \sum_{\substack{\ell=0 \\ k \neq \ell}}^{N-1} E[S_{k,k}] E[S_{\ell,\ell}^*] \right\} \\ &= 0 \quad . \end{aligned} \quad (6.47)$$

Similarly,

$$E[I_3 I_2^*] = 0 \quad . \quad (6.48)$$

Next observe that

$$E[Z(0,0)] = \frac{1}{\sigma_s N \sqrt{N}} \sum_{k=0}^{N-1} E[S_{k,k}^*] = 0 \quad (6.49)$$

due to the zero mean value of the data symbols. It is concluded that

$$\begin{aligned} E[I_2 I_4^*] &= E[I_4 I_2^*] = E[I_2 I_5^*] = E[I_5 I_2^*] \\ &= E[I_2 I_7^*] = E[I_7 I_2^*] = E[I_2 I_8^*] = E[I_8 I_2^*] \\ &= E[I_3 I_4^*] = E[I_4 I_3^*] = E[I_3 I_5^*] = E[I_5 I_3^*] \\ &= E[I_3 I_7^*] = E[I_7 I_3^*] = E[I_3 I_8^*] = E[I_8 I_3^*] = 0 \quad . \end{aligned} \quad (6.50)$$

Also, because the receiver noises are zero mean and statistically independent, it follows that

$$\begin{aligned}
E[I_2 I_6^*] &= E[I_6 I_2^*] = E[I_2 I_9^*] = E[I_9 I_2^*] \\
&= E[I_3 I_6^*] = E[I_6 I_3^*] = E[I_3 I_9^*] = E[I_9 I_3^*] \\
&= E[I_4 I_5^*] = E[I_5 I_4^*] = E[I_4 I_6^*] = E[I_6 I_4^*] \\
&= E[I_4 I_7^*] = E[I_7 I_4^*] = E[I_4 I_8^*] = E[I_8 I_4^*] \\
&= E[I_4 I_9^*] = E[I_9 I_4^*] = E[I_5 I_7^*] = E[I_7 I_5^*] \\
&= E[I_5 I_8^*] = E[I_8 I_5^*] = E[I_5 I_9^*] = E[I_9 I_5^*] \\
&= E[I_6 I_7^*] = E[I_7 I_6^*] = E[I_6 I_8^*] = E[I_8 I_6^*] \\
&= E[I_6 I_9^*] = E[I_9 I_6^*] = E[I_7 I_8^*] = E[I_8 I_7^*] \\
&= E[I_7 I_9^*] = E[I_9 I_7^*] = 0 \quad .
\end{aligned} \tag{6.51}$$

Finally, from Equation (5.13), it is noted that

$$E[f_{\text{IFM}}(t)] = \frac{1}{B\sigma_s \sqrt{KMT_s}} \sum_{k=0}^{K-1} \sum_{m=0}^{K-1} E[S_{k,m}] g_m(t - kT_s) = 0 \tag{6.52}$$

due to the zero mean value of the data symbols. Thus,

$$E[I_5 I_6^*] = E[I_6 I_5^*] = E[I_8 I_9^*] = E[I_9 I_8^*] = 0 \quad . \tag{6.53}$$

At this point 58 of the 64 expectations in Equation (6.35) have been evaluated. It remains to evaluate  $E[|I_4|^2]$ ,  $E[|I_5|^2]$ ,  $E[|I_6|^2]$ ,  $E[|I_7|^2]$ ,  $E[|I_8|^2]$ , and  $E[|I_9|^2]$ .

Note from Equation (6.22) that

$$E[|I_4|^2] = |k_4| E[|\Gamma(0,0)|^2] \quad . \tag{6.54}$$

An expression for  $E[|\Gamma(\tau, \nu)|^2]$  is given by Equation (5.105). Observing from Equation (5.79) that

$$\psi_{mm}(0,0) = B^2 \tag{6.55}$$

and from Equation (5.85) that

$$\psi_{mn}(0,0) = 0 ; \quad m \neq n , \tag{6.56}$$

the expression for  $E[|\Gamma(0,0)|^2]$  simplifies to

$$E[|\Gamma(0,0)|^2] = \left( \frac{1}{N^2 B^2 \sigma_s^2} \right)^2 \mu_4 N \sum_{m=0}^{N-1} B^4 + \left( \frac{1}{N^2 B^2} \right)^2 \sum_{k=0}^{N-1} \sum_{\substack{k'=0 \\ k \neq k'}}^{N-1} \sum_{\substack{m=0 \\ m \neq m'}}^{N-1} \sum_{m'=0}^{N-1} B^4 \quad (6.57)$$

where the conditions of Equations (5.108) and (5.109) have been employed.

With respect to Equation (6.57), observe that there are  $N$  terms in the single summation involving the index  $m$ . In addition, there are  $(N^2 - N)$  terms in the double summation involving the indexes  $k$  and  $k'$  where  $k \neq k'$  and there are  $(N^2 - N)$  terms in the double summation involving the indexes  $m$  and  $m'$  where  $m \neq m'$ . Consequently, there are

$$(N^2 - N)(N^2 - N) = N^2 (N-1)^2 \quad (6.58)$$

terms in the four-fold summation involving the indexes  $k, k', m, m'$  where  $k \neq k'$  and  $m \neq m'$ . It follows that

$$E[|\Gamma(0,0)|^2] = \frac{1}{N^2} \left[ \frac{\mu_4}{\sigma_s^4} + (N-1)^2 \right] \quad (6.59)$$

Thus,

$$E[|I_4|^2] = \frac{|k_4|^2}{N^2} \left[ \frac{\mu_4}{\sigma_s^4} + (N-1)^2 \right] \quad (6.60)$$

An expression for  $I_5$  is given by Equation (6.23). Therefore,

$$E[|I_5|^2] = |k_{RAD}^{TP}|^2 \int_{-\infty}^{\infty} \int_{-\infty}^{\infty} f_{RAD}(t - \tau^{TP}) f_{RAD}^*(\mu - \tau^{TP}) E \left\{ [n^{DP}(t - \tau_B)]^* n^{DP}(\mu - \tau_B) \right\} e^{j2\pi f^{DP}(t-\mu)} dt d\mu \quad (6.61)$$

Denote the autocorrelation function of  $n^{DP}(t)$  by  $R_{n^{DP}}(\tau)$  where

$$R_{n^{DP}}(\tau) = E \left\{ [n^{DP}(t)]^* n^{DP}(t + \tau) \right\} \quad (6.62)$$

Consequently,

$$E \left\{ [n^{DP}(t - \tau_B)]^* n^{DP}(\mu - \tau_B) \right\} = R_{n^{DP}}(\mu - t) \quad (6.63)$$

Assume that  $n^{DP}(t)$  can be approximated as white noise with a two-sided power spectral density given by  $N_0$ . Then

$$R_{n^{DP}}(\tau) = N_0 \delta(\tau) \quad (6.64)$$

where  $\delta(\tau)$  is the Dirac delta function. Hence,

$$\begin{aligned}
E \left[ |I_5|^2 \right] &= \left| k_{RAD}^{TP} \right|^2 \int_{-\infty}^{\infty} \int_{-\infty}^{\infty} f_{RAD}(t - \tau^{TP}) f_{RAD}^*(\mu - \tau^{TP}) \\
&\quad N_0 \delta(\mu - t) e^{j2\pi f^{DP}(t-\mu)} dt d\mu \\
&= \left| k_{RAD}^{TP} \right|^2 N_0 \int_{-\infty}^{\infty} \left| f_{RAD}(t - \tau^{TP}) \right|^2 dt \\
&= \left| k_{RAD}^{TP} \right|^2 N_0
\end{aligned} \tag{6.65}$$

since, by Equation (4.21),  $f_{RAD}(t)$  has unit energy.

An expression for  $I_6$  is given by Equation (6.24). As a result,

$$\begin{aligned}
E \left[ |I_6|^2 \right] &= \left| k_{IFM}^{TP} \right|^2 \int_{-\infty}^{\infty} \int_{-\infty}^{\infty} E \left[ f_{IFM}(t - \tau^{TP}) f_{IFM}^*(\mu - \tau^{TP}) \right] \\
&\quad E \left\{ \left[ n^{DP}(t - \tau_B) \right]^* n^{DP}(\mu - \tau_B) \right\} e^{j2\pi f^{DP}(t-\mu)} dt d\mu \\
&= \left| k_{IFM}^{TP} \right|^2 \int_{-\infty}^{\infty} \int_{-\infty}^{\infty} E \left[ f_{IFM}(t - \tau^{TP}) f_{IFM}^*(\mu - \tau^{TP}) \right] \\
&\quad N_0 \delta(\mu - t) e^{j2\pi f^{DP}(t-\mu)} dt d\mu \\
&= \left| k_{IFM}^{TP} \right|^2 N_0 \int_{-\infty}^{\infty} E \left[ \left| f_{IFM}(t - \tau^{TP}) \right|^2 \right] dt \\
&= \left| k_{IFM}^{TP} \right|^2 N_0
\end{aligned} \tag{6.66}$$

where use was made of Equation (6.64) and the fact that  $f_{IFM}(t)$  is normalized by Equation (5.13) to have unit average energy.

An expression for  $I_7$  is given by Equation (6.25). It follows that

$$\begin{aligned}
E \left[ |I_7|^2 \right] &= \int_{-\infty}^{\infty} \int_{-\infty}^{\infty} E \left\{ n^{TP}(t) \left[ n^{TP}(\mu) \right]^* \right\} \\
&\quad E \left\{ \left[ n^{DP}(t - \tau_B) \right]^* n^{DP}(\mu - \tau_B) \right\} e^{j2\pi f_B(\mu-t)} dt d\mu \quad .
\end{aligned} \tag{6.67}$$

The autocorrelation function of  $n^{TP}(t)$  is defined to be

$$R_{n^{TP}}(\tau) = E \left\{ \left[ n^{TP}(t) \right]^* n^{TP}(t + \tau) \right\} \quad . \tag{6.68}$$

Making use of Equations (6.63) and (6.68), Equation (6.67) becomes



$$E[|I_7|^2] = \iint_{-\infty}^{\infty} R_{n^{TP}}(t-\mu) R_{n^{DP}}(\mu-t) e^{j2\pi f_B(\mu-t)} dt d\mu \quad (6.69)$$

At this point it would be convenient to approximate both  $n^{DP}(t)$  and  $n^{TP}(t)$  as statistically independent white noise processes. However, this leads to the integrand of Equation (6.69) containing a squared impulse with the end result being that  $E[|I_7|^2]$  is infinite. This unrealistic result is caused by the simplifying but idealized assumption of white noise.

In actuality, the non-cooperative bistatic radar will have a receiver bandwidth of  $2W$ . A realistic assumption is that the power spectral density of the receiver noise is constant over this bandwidth. Therefore, it is assumed that the power spectral density of the noise complex envelopes is rectangular with height,  $N_0$ , and extending from  $-W$  to  $+W$  Hz. The autocorrelation function of this bandlimited noise is then given by

$$R_{n^{DP}}(\tau) = R_{n^{TP}}(\tau) = \int_{-W}^W N_0 e^{j2\pi f \tau} df = 2N_0 W \frac{\sin 2\pi W \tau}{2\pi W \tau} \quad (6.70)$$

Another point that need to be addressed is the infinite limits of integration that appear in Equation (6.69). They arise from Equation (2.42) where the infinite limits of integration are permitted because of the actual finite time extent of the integrand. (Recall that a radar will employ time gates to extract time segments of the received signal equal in duration to the radar pulse width.) In the absence of estimation errors, Equation (2.42) would be expressed as

$$\ell = \int_{-\infty}^{\infty} [s^{DP}(t-\tau_B)]^* s^{TP}(t) e^{-j2\pi f_B(t-\tau^{DP}-\tau_B)} dt \quad (6.71)$$

Under the conditions of Equations (5.108) and (5.109) both the main radar and interferometer signals contained within  $s^{DP}(t-\tau_B)$  and  $s^{TP}(t)$  are zero outside the time interval

$$\tau^{TP} \leq t \leq \tau^{TP} + NT \quad (6.72)$$

Consequently, Equation (6.71) can be written as

$$\ell = \int_{\tau^{TP}}^{\tau^{TP}+NT} [s^{DP}(t-\tau_B)]^* s^{TP}(t) e^{-j2\pi f_B(t-\tau^{TP})} dt \quad (6.73)$$

where use was made of Equation (2.3). Introducing the change of variable

$$\tau = t - \tau^{TP}, \quad (6.74)$$

Equation (6.73) becomes

$$\begin{aligned} \ell &= \int_0^{NT} [s^{DP}(\tau + \tau^{TP} - \tau_B)]^* s^{TP}(\tau + \tau^{TP}) e^{-j2\pi f_B \tau} d\tau \\ &= \int_0^{NT} [s^{DP}(t + \tau^{DP})]^* s^{TP}(t + \tau^{TP}) e^{-j2\pi f_B t} dt \end{aligned} \quad (6.75)$$

where use was, again, made of Equation (2.3) and the variable,  $t$ , was substituted for the variable,  $\tau$ . Focusing on the noise components of Equations (2.28) and (2.35), the component of  $\ell$  corresponding to  $I_7$  is given by

$$I_7 = \int_0^{NT} [n^{DP}(t + \tau^{DP})]^* n^{TP}(t + \tau^{TP}) e^{-j2\pi f_B t} dt \quad (6.76)$$

Equation (6.76) is now used to determine an expression for  $E[|I_7|^2]$ .

Utilizing Equation (6.76), it follows that

$$\begin{aligned} E[|I_7|^2] &= \int_0^{NT} \int_0^{NT} E\left\{[n^{DP}(t+\tau^{DP})]^* n^{DP}(u+\tau^{DP})\right\} \\ &E\left\{n^{TP}(t+\tau^{TP}) [n^{TP}(u+\tau^{TP})]^*\right\} e^{j2\pi f_B(u-t)} dt du \\ &= \int_0^{NT} \int_0^{NT} R_{n^{DP}}(u-t) R_{n^{TP}}(t-u) e^{j2\pi f_B(u-t)} dt du . \end{aligned} \quad (6.77)$$

Observe that Equation (6.77) is identical to Equation (6.69) except that the limits of integration are now finite. Note from Equation (6.70) that the noise correlation function is an even function of  $\tau$ . Consequently,

$$R_{n^{TP}}(t-u) = R_{n^{TP}}(u-t) . \quad (6.78)$$

Employing Equations (6.70) and (6.78), it follows that

$$E[|I_7|^2] = (2N_0 W)^2 \int_0^{NT} \int_0^{NT} \left[ \frac{\sin 2\pi W(u-t)}{2\pi W(u-t)} \right]^2 e^{j2\pi f_B(u-t)} dt du . \quad (6.79)$$

Attention is now devoted to evaluation of the double integral in Equation (6.79). Introduce the change of variable

$$\tau = u - t . \quad (6.80)$$

We wish to replace the double integral involving  $u$  and  $t$  by a double integral involving  $\tau$  and  $t$ . The regions of integration in the  $t$  vs.  $u$  and  $t$  vs.  $\tau$  planes are shown in Figure 6.1. Observe that the boundaries for the region of integration in the  $t$  vs.  $\tau$  plane are given by

$$\begin{aligned} \text{I: } & t = NT, \quad \tau = u - NT \\ \text{II: } & t = 0, \quad \tau = u \\ \text{III: } & u = NT, \quad \tau = NT - t \\ \text{IV: } & u = 0, \quad \tau = -t \end{aligned} \quad (6.81)$$

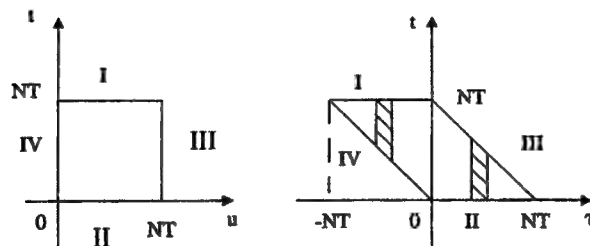


Figure 6.1:  $E[|I_7|^2]$  is evaluated by integrating over the regions indicated.

Carrying out the integration in the  $t$  vs.  $\tau$  plane,

$$\begin{aligned}
 E[|I_7|^2] &= (2N_0 W)^2 \int_0^{NT} \left[ \frac{\sin 2\pi W \tau}{2\pi W \tau} \right]^2 e^{j2\pi f_B \tau} \left\{ \int_0^{NT-\tau} dt \right\} d\tau \\
 &\quad + (2N_0 W)^2 \int_{-NT}^0 \left[ \frac{\sin 2\pi W \tau}{2\pi W \tau} \right]^2 e^{j2\pi f_B \tau} \left\{ \int_{-\tau}^{NT} dt \right\} d\tau \\
 &= (2N_0 W)^2 \int_0^{NT} \left[ \frac{\sin 2\pi W \tau}{2\pi W \tau} \right]^2 e^{j2\pi f_B \tau} (NT - \tau) d\tau \\
 &\quad + (2N_0 W)^2 \int_{-NT}^0 \left[ \frac{\sin 2\pi W \tau}{2\pi W \tau} \right]^2 e^{j2\pi f_B \tau} (NT + \tau) d\tau \\
 &= (2N_0 W)^2 \int_{-NT}^{NT} \left[ \frac{\sin 2\pi W \tau}{2\pi W \tau} \right]^2 (NT - |\tau|) e^{j2\pi f_B \tau} d\tau
 \end{aligned} \tag{6.82}$$

where the strips of integration with respect to  $t$  are shown in Figure 6.1. Unfortunately, even though the expression for  $E[|I_7|^2]$  has been reduced to a single integration, a closed form result does not appear possible.

To obtain an estimate of  $E[|I_7|^2]$ , a rectangular approximation is made for  $\sin 2\pi W \tau / 2\pi W \tau$ . The height of the rectangle is chosen to be unity, which is the maximum value of  $\sin 2\pi W \tau / 2\pi W \tau$ , and the width of the rectangle is chosen to be  $1/W$ , which is the width of the main lobe of  $\sin 2\pi W \tau / 2\pi W \tau$ . The rectangular approximation is centered at the origin because the main lobe of  $\sin 2\pi W \tau / 2\pi W \tau$  is, also, centered at the origin. Hence, we introduce the approximation

$$\frac{\sin 2\pi W \tau}{2\pi W \tau} \approx \begin{cases} 1, & -\frac{1}{2W} \leq \tau \leq \frac{1}{2W} \\ 0, & \text{otherwise} \end{cases} \tag{6.83}$$

Consequently,

$$\begin{aligned}
E[|I_7|^2] &\approx (2N_0 W)^2 \int_{-\frac{1}{2W}}^{\frac{1}{2W}} (NT - |\tau|) e^{j2\pi f_B \tau} d\tau \\
&= (2N_0 W)^2 \int_{-\frac{1}{2W}}^0 (NT + \tau) e^{j2\pi f_B \tau} d\tau \\
&\quad + (2N_0 W)^2 \int_0^{\frac{1}{2W}} (NT - \tau) e^{j2\pi f_B \tau} d\tau .
\end{aligned} \tag{6.84}$$

Utilizing the integral relation that

$$\int \tau e^{a\tau} d\tau = \frac{e^{a\tau}}{a^2} (a\tau - 1) \tag{6.85}$$

and combining results, it follows that

$$E[|I_7|^2] \approx (2N_0 W)^2 \left\{ \frac{1}{2(\pi f_B)^2} \left[ 1 - \cos \frac{\pi f_B}{W} \right] + \left( NT - \frac{1}{2W} \right) \frac{\sin \frac{\pi f_B}{W}}{\pi f_B} \right\} . \tag{6.86}$$

From Equation (4.65) and (5.26) the baseband bandwidth of both the Costas and OFDM signals is approximately given by

$$BW = \frac{N}{T} \tag{6.87}$$

where the conditions of Equations (5.108) and (5.109) are assumed to apply. Assuming the receiver bandwidth of the non-cooperative bistatic radar receiver is twice the baseband bandwidth of the signals,

$$W = \frac{N}{T} . \tag{6.88}$$

As a result, Equation (6.86) can be expressed as

$$E[|I_7|^2] \approx \frac{\left( 2N_0 \frac{N}{T} \right)^2}{\pi f_B} \left\{ \frac{1 - \cos \left( \frac{\pi f_B T}{N} \right)}{2\pi f_B} + \left( NT - \frac{T}{2N} \right) \sin \left( \frac{\pi f_B T}{N} \right) \right\} \tag{6.89}$$

where  $f_B$  is the bistatic Doppler shift given by Equation (2.38).

Finally, following the same reasoning that led to the results of Equations (6.65) and (6.66), it is concluded that

$$E[|I_8|^2] = |k_{RAD}^{DP}|^2 N_0 \quad (6.90)$$

and

$$E[|I_9|^2] = |k_{IFM}^{DP}|^2 N_0 \quad (6.91)$$

With reference to Equations (6.47), (6.48), (6.50), (6.51), and (6.53), it is noted that all terms are zero in the double summation of Equation (6.35) for which  $i \neq j$ . Hence,

$$E[|\ell_1|^2] = \sum_{i=2}^9 E[|I_i|^2] \quad (6.92)$$

Substitution of Equations (2.45), (6.44), (6.45), (6.60), (6.65), (6.66), (6.89), (6.90), and (6.91) into Equation (6.92) yields

$$\begin{aligned} E[|\ell_1|^2] &\approx \frac{|k_{RAD}^{DP}|^2 |k_{IFM}^{TP}|^2}{N^2} + \frac{|k_{IFM}^{DP}|^2 |k_{RAD}^{TP}|^2}{N^2} \\ &+ \frac{|k_{IFM}^{DP}|^2 |k_{IFM}^{TP}|^2}{N^2} \left[ \frac{\mu_4}{\sigma_s^4} + (N-1)^2 \right] + |k_{RAD}^{TP}|^2 N_0 \\ &+ |k_{IFM}^{TP}|^2 N_0 + |k_{RAD}^{DP}|^2 N_0 + |k_{IFM}^{DP}|^2 N_0 \\ &+ \frac{\left(2N_0 \frac{N}{T}\right)^2}{\pi f_B} \left\{ \frac{1 - \cos\left(\frac{\pi f_B T}{N}\right)}{2\pi f_B} + \left(NT - \frac{T}{2N}\right) \sin\left(\frac{\pi f_B T}{N}\right) \right\} . \end{aligned} \quad (6.93)$$

On the other hand, making use of Equations (2.45) and (6.32),

$$|E[\ell_1]|^2 = |k_4|^2 = |k_{IFM}^{DP}|^2 |k_{IFM}^{TP}|^2 \quad (6.94)$$

The variance of  $\ell_1$ , as given by Equation (6.33), then becomes

$$\begin{aligned}
Var\{\ell_I\} \approx & |k_{RAD}^{DP}|^2 \left[ N_0 + \left| \frac{k_{IFM}^{TP}}{N} \right|^2 \right] + |k_{IFM}^{DP}|^2 \left[ N_0 + \left| \frac{k_{RAD}^{TP}}{N} \right|^2 \right] \\
& + |k_{IFM}^{TP}|^2 \left[ N_0 + \left| \frac{k_{IFM}^{DP}}{N} \right|^2 \left( \frac{\mu_4}{\sigma_s^4} - 2N + 1 \right) \right] + |k_{RAD}^{TP}|^2 N_0 \\
& + \frac{\left( 2N_0 \frac{N}{T} \right)^2}{\pi f_B} \left\{ \frac{1 - \cos\left( \frac{\pi f_B T}{N} \right)}{2\pi f_B} + \left( NT - \frac{T}{2N} \right) \sin\left( \frac{\pi f_B T}{N} \right) \right\}.
\end{aligned} \tag{6.95}$$

One measure of performance for a radar is signal-to-noise ratio. For a monostatic radar operating in an additive thermal noise background with variance,  $N_0$ , the signal-to-noise ratio is given by

$$(SNR)_{Monostatic} = \frac{|E[\ell_s]|^2}{Var\{Noise\}} = \frac{|E[\ell_s]|^2}{N_0}. \tag{6.96}$$

For the non-cooperative bistatic radar, the signal-to-noise ratio is

$$(SNR)_{Non-cooperative}^{Bistatic} = \frac{|E[\ell_s]|^2}{Var\{\ell_I\}} \tag{6.97}$$

where  $Var\{\ell_I\}$  is given by Equation (6.95). The loss factor is defined to be

$$\begin{aligned}
LF &= \frac{(SNR)_{Monostatic}}{(SNR)_{Non-cooperative Bistatic}} = \frac{VAR\{\ell_I\}}{N_0} \\
&\approx |k_{RAD}^{DP}|^2 \left[ 1 + \frac{1}{N_0} \left| \frac{k_{IFM}^{TP}}{N} \right|^2 \right] + |k_{IFM}^{DP}|^2 \left[ 1 + \frac{1}{N_0} \left| \frac{k_{RAD}^{TP}}{N} \right|^2 \right] \\
&+ |k_{IFM}^{TP}|^2 \left[ 1 + \frac{1}{N_0} \left| \frac{k_{IFM}^{DP}}{N} \right|^2 \left( \frac{\mu_4}{\sigma_s^4} - 2N + 1 \right) \right] + |k_{RAD}^{TP}|^2 \\
&+ \frac{4N_0}{\pi f_B} \left( \frac{N}{T} \right)^2 \left\{ \frac{1 - \cos\left(\frac{\pi f_B T}{N}\right)}{2\pi f_B} + \left( NT - \frac{T}{2N} \right) \sin\left(\frac{\pi f_B T}{N}\right) \right\} .
\end{aligned} \tag{6.98}$$

Observe that the loss factor, LF, is defined to be a positive number greater than or equal to unity since the signal-to-noise ratio of the monostatic radar is expected to be larger than that of the non-cooperative bistatic radar. The more effective is the interferometer in masking the transmitted radar waveform, the larger will be the value for LF.

### 6.3 Non-Cooperative Bistatic Radar Receiver Performance

#### 6.3.1 False Alarm Probability

Because  $Z(0,0)$ ,  $\Gamma(0,0)$ , and  $f_{IFM}(t)$  consist of a large number of random components due to the randomness of the data symbols, the central limit theorem can be invoked to justify modeling the detection statistic,  $\ell$ , as a complex Gaussian random variable. By definition, the probability of false alarm is the conditional probability of detecting a target given that a target is not present. With reference to Equations (2.35), (2.36), and (2.37), the absence of a target is equivalent to

$$\sigma_T = k_{RAD}^{TP} = k_{IFM}^{TP} = 0 . \tag{6.99}$$

Then

$$s^{TP}(t) = n^{TP}(t) . \tag{6.100}$$

The mean value of the signal component of the detection statistic is given by Equation (6.28). In view of Equations (2.45) and (6.99), it follows that

$$E[\ell_s] = k_1 = 0 \tag{6.101}$$

in the absence of a target. In addition, the mean value of the interference component of the detection statistic is given by Equation (6.32). Hence, in the absence of a target, it is concluded from Equations (2.45) and (6.99) that

$$E[\ell_I] = k_4 = 0 \quad . \quad (6.102)$$

Thus, given that a target is not present,

$$E[\ell] = E[\ell_s] + E[\ell_I] = 0 \quad . \quad (6.103)$$

Let  $\sigma_{\ell_0}^2$  denote the variance of the detection statistic in the absence of a target. Because  $\ell_s$  is a constant,

$$\begin{aligned} \sigma_{\ell_0}^2 = \text{Var}\{\ell_I\} &\approx |k_{RAD}^{DP}|^2 N_0 + |k_{IFM}^{DP}|^2 N_0 \\ &+ \frac{(2N_0 N/T)^2}{\pi f_B} \left\{ \frac{1 - \cos\left(\frac{\pi f_B T}{N}\right)}{2\pi f_B} + \left(NT - \frac{T}{2N}\right) \sin\frac{\pi f_B T}{N} \right\} \end{aligned} \quad (6.104)$$

where use was made of Equations (6.99) and (6.95). The absence of a target is conventionally referred to as hypothesis,  $H_0$ . Therefore, under  $H_0$ , the detection statistic,  $\ell$ , can be modeled as a zero-mean complex Gaussian random variable with its variance given by Equation (6.104).

Denote the real and imaginary parts of the detection statistic by

$$\ell_r = \text{Re}\{\ell\} \quad (6.105)$$

and

$$\ell_i = \text{Im}\{\ell\} \quad . \quad (6.106)$$

In the absence of a target, the probability density function of  $\ell$  is

$$\begin{aligned} p_{\ell|H_0}(L = L_r + j L_i | H_0) &= p_{\ell_r, \ell_i | H_0}(L_r, L_i | H_0) \\ &= \frac{1}{2\pi \sigma_{\ell_0}^2} e^{-\frac{|L|^2}{2\sigma_{\ell_0}^2}} = \frac{1}{2\pi \sigma_{\ell_0}^2} e^{-\frac{(L_r^2 + L_i^2)}{2\sigma_{\ell_0}^2}} \end{aligned} \quad (6.107)$$

where  $\sigma_{\ell_0}^2$  is given by Equation (6.104).

Let  $H_1$  refer to the hypothesis that a target is present. The statistical test employed for detection is then described by

$$\begin{array}{c} H_1 \\ |L| > \gamma \\ H_0 \end{array} \quad (6.108)$$

where  $\gamma$  is a constant that denotes the threshold. A statistically equivalent test, which is easier to analyze, is



$$|L|^2 = L_r^2 + L_i^2 \begin{matrix} > \\ < \end{matrix} \begin{matrix} H_1 \\ H_0 \end{matrix} \gamma^2 \quad . \quad (6.109)$$

As a result, the probability of false alarm is given by

$$P_F = \mathbf{Pr} \{ \ell_r^2 + \ell_i^2 \geq \gamma^2 | H_0 \} = \mathbf{Pr} \{ \ell_r, \ell_i \in R | H_0 \} \quad (6.110)$$

where  $R$  is the shaded region sketched in Figure 6.2. Consequently,

$$\begin{aligned} P_F &= \iint_R p_{\ell_r, \ell_i | H_0}(L_r, L_i | H_0) dL_r dL_i \\ &= \iint_R \frac{1}{2\pi\sigma_{\ell_o}^2} e^{-\frac{(L_r^2 + L_i^2)}{2\sigma_{\ell_o}^2}} dL_r dL_i \quad . \end{aligned} \quad (6.111)$$

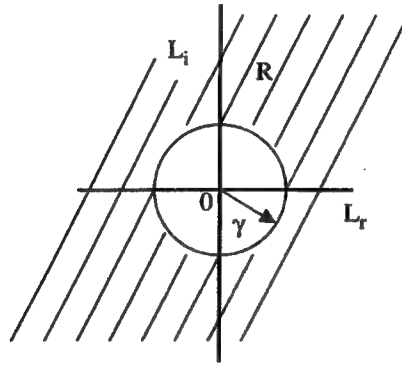


**Figure 6.2:** A target is declared present when  $|L|^2$  falls into the shaded region.

To evaluate the double integration in Equation (6.110), it is convenient to introduce polar coordinates. Let

$$L_r = Z \cos \beta \quad (6.111)$$

and

$$L_i = Z \sin \beta \quad . \quad (6.112)$$

It follows that

$$Z = \sqrt{L_r^2 + L_i^2} \quad (6.113)$$

and

$$\beta = \tan^{-1} \frac{L_i}{L_r} \quad . \quad (6.114)$$

Equation (6.110) can then be expressed as

$$P_F = \frac{1}{2\pi\sigma_{\ell_0}^2} \int_{-\pi}^{\pi} d\beta \int_{-\infty}^{\infty} Z e^{-\frac{Z^2}{2\sigma_{\ell_0}^2}} dZ \quad (6.115)$$

where use was made of the differential relationship

$$dL_r dL_i = Z dZ d\beta \quad (6.116)$$

Evaluation of the integrals results in

$$\begin{aligned} P_F &= \frac{1}{2\pi\sigma_{\ell_0}^2} \int_{-\pi}^{\pi} d\beta \left[ -\sigma_{\ell_0}^2 e^{-\frac{Z^2}{2\sigma_{\ell_0}^2}} \right]_{-\infty}^{\infty} \\ &= \frac{1}{2\pi} e^{-\frac{\gamma^2}{2\sigma_{\ell_0}^2}} \int_{-\pi}^{\pi} d\beta = e^{-\frac{\gamma^2}{2\sigma_{\ell_0}^2}} \end{aligned} \quad (6.117)$$

From Equation (6.117) it follows that

$$\gamma = \sigma_{\ell_0} \sqrt{2 \ln (1/P_F)} \quad (6.118)$$

Consequently, the threshold is readily determined from a knowledge of  $\sigma_{\ell_0}^2$  and specification of the false alarm probability. Note that the smaller is  $P_F$  and the larger is  $\sigma_{\ell_0}$  the larger is the required value of the threshold.

### 6.3.2 Detection Probability

By definition, the probability of detection is the conditional probability of detecting a target given that a target is present. The presence of a target is typically designated as hypothesis,  $H_1$ . Under  $H_1$  the detection statistic,  $\ell$ , is modeled as a complex Gaussian random variable with mean

$$m_{\ell_1} = m_{\ell_r} + j m_{\ell_i} \quad (6.119)$$

and variance  $\sigma_{\ell_1}^2$ . From Equations (6.28), (6.32), and (2.45) it follows that

$$m_{\ell_1} = E[\ell_s | H_1] + E[\ell_i | H_1] = (k_{RAD}^{DP})^* k_{RAD}^{TP} + (k_{IFM}^{DP})^* k_{IFM}^{TP} \quad (6.120)$$

$\sigma_{\ell_1}^2$  is given by Equation (6.95).

In the presence of a target, the probability density function of  $\ell$  is

$$\begin{aligned} p_{\ell | H_1}(L | H_1) &= p_{\ell_r, \ell_i | H_1}(L_r, L_i | H_1) \\ &= \frac{1}{2\pi\sigma_{\ell_1}^2} e^{-\frac{|L - m_{\ell_1}|^2}{2\sigma_{\ell_1}^2}} \end{aligned} \quad (6.121)$$

However,

$$\begin{aligned}
|L - m_{\ell_1}|^2 &= [(L_r - m_{\ell_r}) + j(L_i - m_{\ell_i})][(L_r - m_{\ell_r}) - j(L_i - m_{\ell_i})] \\
&= m_{\ell_r}^2 + m_{\ell_i}^2 + L_r^2 + L_i^2 - 2(m_{\ell_r} L_r + m_{\ell_i} L_i)
\end{aligned} \quad (6.122)$$

As a result, Equation (6.121) becomes

$$p_{\ell|H_1}(L|H_1) = \frac{1}{2\pi\sigma_{\ell_1}^2} e^{-\frac{m_{\ell_r}^2 + m_{\ell_i}^2}{2\sigma_{\ell_1}^2}} e^{-\frac{L_r^2 + L_i^2 - 2(m_{\ell_r} L_r + m_{\ell_i} L_i)}{2\sigma_{\ell_1}^2}} \quad (6.123)$$

Employing the test specified in Equation (6.109) the probability of detection is given by

$$P_D = \Pr\{\ell_r^2 + \ell_i^2 \geq \gamma^2 | H_1\} = \Pr\{\ell_r, \ell_i \in R | H_1\} \quad (6.124)$$

where R, once again, is the shaded region sketched in Figure 6.2. Consequently,

$$\begin{aligned}
P_D &= \iint_R p_{\ell_r, \ell_i | H_1}(L_r, L_i | H_1) dL_r dL_i \\
&= \frac{1}{2\pi\sigma_{\ell_1}^2} e^{-\frac{m_{\ell_r}^2 + m_{\ell_i}^2}{2\sigma_{\ell_1}^2}} \iint_R e^{-\frac{L_r^2 + L_i^2 - 2(m_{\ell_r} L_r + m_{\ell_i} L_i)}{2\sigma_{\ell_1}^2}} dL_r dL_i
\end{aligned} \quad (6.125)$$

Evaluation of the double integral in Equation (6.125) is, as before, facilitated through introduction of the polar coordinates defined by Equations (6.111) and (6.112). It follows that

$$P_D = \frac{1}{2\pi\sigma_{\ell_1}^2} e^{-\frac{m_{\ell_r}^2 + m_{\ell_i}^2}{2\sigma_{\ell_1}^2}} \int_{\gamma}^{\infty} Z e^{-\frac{Z^2}{2\sigma_{\ell_1}^2}} \left[ \int_{-\pi}^{\pi} e^{\frac{Z(m_{\ell_r} \cos \beta + m_{\ell_i} \sin \beta)}{\sigma_{\ell_1}^2}} d\beta \right] dZ \quad (6.126)$$

From a table of integrals it is known that

$$\frac{1}{2\pi} \int_{-\pi}^{\pi} e^{r \cos \beta + s \sin \beta} d\beta = I_0 \left[ \sqrt{r^2 + s^2} \right] \quad (6.127)$$

where  $I_0(\cdot)$  is a zeroth-order modified Bessel function of the first kind. Therefore, the detection probability becomes

$$P_D = \frac{1}{\sigma_{\ell_1}^2} e^{-\frac{m_{\ell_r}^2 + m_{\ell_i}^2}{2\sigma_{\ell_1}^2}} \int_{\gamma}^{\infty} Z e^{-\frac{Z^2}{2\sigma_{\ell_1}^2}} I_0 \left[ \frac{Z}{\sigma_{\ell_1}^2} \sqrt{m_{\ell_r}^2 + m_{\ell_i}^2} \right] dZ \quad (6.128)$$

With reference to Equation (6.119), observe that

$$|m_{\ell_1}|^2 = m_{\ell_r}^2 + m_{\ell_i}^2 \quad (6.129)$$

Thus, the expression for  $P_D$  can be simplified to

$$P_D = \frac{1}{\sigma_{\ell_1}^2} e^{-\frac{|m_{\ell_1}|}{2\sigma_{\ell_1}^2}} \int_{\gamma}^{\infty} Z e^{-\frac{Z^2}{2\sigma_{\ell_1}^2}} I_0 \left[ \frac{|m_{\ell_1}|}{\sigma_{\ell_1}^2} Z \right] dZ . \quad (6.130)$$

Having integrated out  $\beta$ , it has been determined that the probability density function on  $z$  is given by

$$p_z(z) = \begin{cases} \frac{1}{\sigma_{\ell_1}^2} e^{-\frac{|m_{\ell_1}|^2}{2\sigma_{\ell_1}^2}} Z e^{-\frac{Z^2}{2\sigma_{\ell_1}^2}} I_0 \left[ \frac{|m_{\ell_1}|}{\sigma_{\ell_1}^2} Z \right] , & Z \geq 0 \\ 0 , & Z < 0 \end{cases} . \quad (6.131)$$

Consequently,

$$\int_0^{\infty} p_z(z) dz = 1 \quad (6.132)$$

and the probability of detection can be expressed as

$$P_D = 1 - \frac{1}{\sigma_{\ell_1}^2} e^{-\frac{|m_{\ell_1}|^2}{2\sigma_{\ell_1}^2}} \int_0^{\gamma} Z e^{-\frac{Z^2}{2\sigma_{\ell_1}^2}} I_0 \left[ \frac{|m_{\ell_1}|}{\sigma_{\ell_1}^2} Z \right] dZ . \quad (6.133)$$

The above result can be further simplified by introducing the incomplete Toronto function [13,14] which is defined as

$$T_B(m,n,r) = 2r^{n-m+1} e^{-r^2} \int_0^B t^{m-n} e^{-t^2} I_n[2rt] dt . \quad (6.134)$$

Let

$$r = \frac{|m_{\ell_1}|}{\sqrt{2} \sigma_{\ell_1}} \quad (6.135)$$

and

$$t = \frac{Z}{\sqrt{2} \sigma_{\ell_1}} . \quad (6.136)$$

Substitution of Equations (6.135) and (6.136) into Equation (6.133) yields

$$\begin{aligned} P_D &= 1 - 2e^{-r^2} \int_0^{\frac{\gamma}{\sqrt{2} \sigma_{\ell_1}}} t e^{-t^2} I_0[2rt] dt \\ &= \frac{1}{\sqrt{2} \sigma_{\ell_1}} T_{\gamma} \left( 1, 0, \frac{|m_{\ell_1}|}{\sqrt{2} \sigma_{\ell_1}} \right) . \end{aligned} \quad (6.137)$$

Plots of  $T_{\sqrt{v}}(1, 0, \sqrt{q})$  are presented in Figures 13 and 14 of the Marcum paper [13] for various choices of  $v$  and  $q$ . Although the Toronto function needs to be evaluated numerically, Equations (6.130) and (6.133) clearly reveal that the detection probability is decreased by increasing  $\gamma$  and  $\sigma_{\ell_1}^2$ . This observation is useful in selecting system parameters to effectively degrade the operation of the non-cooperative bistatic radar.

## CHAPTER 7

### CONCLUSIONS

#### 7.1 Summary

Radar receivers typically utilize a replica of the transmitted waveform for processing the radar return. In an attempt to estimate this transmitted waveform, non-cooperative bistatic radars normally intercept a direct path signal emitted through the side lobes of the host radar.

This report investigates the use of an interferometer along with the host radar to deny coherent reference signals to unwanted observers. The interferometer signal is intended to be

- 1) effective in masking the host radar signal emitted through the side lobes,
- 2) orthogonal to the signal transmitted through the main lobe of the host radar so as not to degrade radar performance,
- 3) useful for data/voice communications,
- 4) controllable such that separate communication signals can be directed to different receivers located in different directions.

In addition, the host radar signal is intended to be flexible to allow for multi-mission operations.

The time domain cannot be used to achieve orthogonality between the interferometer and radar waveforms because, assuming perfect synchronization and temporal orthogonality, the non-cooperative radar could correlate the direct path signal with its radar return without experiencing any loss due to presence of the interferometer signal. In fact, for effective masking, the radar and interferometer signals should be highly correlated in the time domain.

Consequently, the desired orthogonality must be achieved in the spatial domain. Analysis of the two-element interferometer array factor reveals that a relatively broad spatial null exists in its end fire position when the element spacing is an odd integer number of half wavelengths of the transmitted interferometer signal. This null cannot be steered electronically. Therefore, when the host radar main lobe points broadside to the x-axis, the interferometer elements must be placed along the y-axis in order to take advantage of the broad null. Should the main lobe be steered to different directions, it would be necessary to mechanically rotate the interferometer elements in order to maintain the spatial orthogonality between the interferometer and radar waveforms.

In order to communicate separate signals in different directions, it will be necessary to steer the interferometer without destroying the broad null in the end fire position. This can be accomplished by frequency hopping the transmitted carrier such that the odd integer relationship between the element spacing and wavelength is maintained while the carrier changes from one frequency to another.

The flexibility of frequency hopping makes it attractive for design of the host radar waveform. Depending upon the particular mission, the frequency hops can be arranged to synthesize a discrete frequency quantized approximation to the frequency modulated signal that produces a desired delay-Doppler ambiguity function.

Because the ideal shape of the ambiguity function is an impulse function, the Costas signal is proposed for the host radar waveform. It yields a thumb tack shaped ambiguity function with a relatively low pedestal. For a fixed number of frequency hops within a radar pulse, there are many different hopping patterns that result in essentially the same thumb tack shaped ambiguity function. Hence, different frequency hopping patterns can be utilized to further complicate the coherent reference estimation task of the non-cooperative radar.

Having selected the Costas signal for the transmitted radar waveform, orthogonal frequency division multiplexing (OFDM) becomes an attractive communication technique for the interferometer. The hopping frequencies of the Costas signal are required to be orthogonal over a hopping interval of duration,  $T$ . The subcarrier

frequencies of an OFDM signal are required to be orthogonal over a symbol duration,  $T_s$ . By selecting  $T = T_s$ , the two sets of frequencies become identical. In addition, the use of M-ary amplitude and phase shift keying to modulate the subcarriers makes it very difficult to separate the Costas and OFDM signals when their amplitude transitions are synchronized in time.

Utilization of OFDM for communications has many important advantages. Both modulation and demodulation can be implemented using fast Fourier transforms. The difficult tasks of channel estimation and equalization are simplified significantly when communicating over fading and time-variant broadband channels. Also, the parallel nature of OFDM makes it an efficient scheme for the transmission of data.

Performance of the non-cooperative bistatic radar receiver was analyzed. In addition to noise terms, the detection statistic was shown to involve the delay-Doppler ambiguity functions of the host radar and interferometer waveforms as well as their cross ambiguity function. Analytical expressions for these functions were obtained under the assumption that the host radar and interferometer employ Costas and OFDM signals, respectively. Taking advantage of the result that the detection statistic consists of a random sum of many terms, none of which are dominant, the detection statistic was approximated as a complex Gaussian random variable. Analytical expressions were then derived for the false alarm and detection probabilities of the non-cooperative bistatic radar.

## **7.2 Suggestions for Future Work**

### **7.2.1 Performance Evaluation of the Complete System Using Realistic Scenarios**

Although analytical expressions needed for performance of the non-cooperative bistatic radar were obtained, time did not permit for assessment of the complete system. It is desirable to

- 1) Construct plots of the OFDM ambiguity function and the cross ambiguity function between OFDM and Costas signals for both individual sample functions and the entire ensemble of the OFDM signal,
- 2) Obtain analytical expressions for the false alarm and detection probabilities of the host radar,
- 3) Postulate realistic scenarios along with the corresponding numerical values for the system parameters,
- 4) Evaluate complete system performance for the realistic scenarios postulated in (3) and adjust the system parameters where necessary to improve performance,
- 5) Perform computer simulations to verify the predicted theoretical results.

### **7.2.2 Extension of the Interferometer to More than Two Elements**

The two-element interferometer, under a specified constraint, produced a broad null in the end fire position which was useful in obtaining spatial orthogonality between the host radar and interferometer waveforms. However, this null could not be steered electronically. It is conjectured that introduction of a third interferometer element will enable steering of the broad null. Should this prove to be possible, the advantages to be gained by adding additional elements would be investigated.

The concept of the tri-element interferometer is illustrated in Figure 7.1. Elements 1 and 2 can be replaced by an equivalent element, denoted by E. Elements E and 3 then comprise an equivalent two-element interferometer. By adjusting the amplitudes and phases of the sinusoidal signals applied to elements 1 and 2, the position of element E can be moved horizontally along the line connecting elements 1 and 2. Selection of the frequency of excitation such that the distance,  $d$ , is an odd integer of half wave lengths would then produce a broad null in the end fire position of the equivalent two-element interferometer. In this manner the broad null could be electronically steered by appropriately selecting the amplitudes and frequencies of the sinusoidal signals applied to elements 1, 2, and 3.

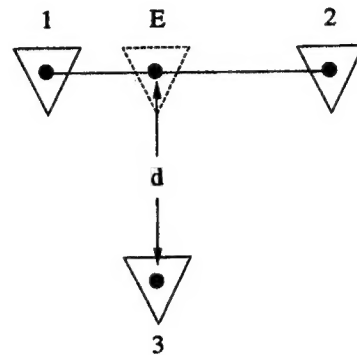


Figure 7.1: The tri-element interferometer can be viewed as an equivalent two-element interferometer.

### 7.2.3 Generalization of the Ambiguity Function to Include Direction of Arrival

Because both spatial and temporal processing is performed in a radar, an ambiguity function generalized to include the direction of arrival would be extremely useful. As a first step, it is proposed to carry out this generalization by incorporating the antenna radiation patterns as a function of angle.

More generally, the transformation of operators approach, introduced by Cohen [15], may be useful in developing a combined delay-Doppler, spatial displacement-spatial frequency ambiguity function. This would be applicable to pulse propagation where there is a strong correlation between temporal and spatial frequencies.



## REFERENCES

- [1] Nicholas J. Willis, Bistatic Radar, Artech House, Boston, 1991.
- [2] Daniel Thomas, Jr., "Synchronization of Non-Cooperative Bistatic Radar Receivers", Ph.D. Dissertation, Syracuse University, Syracuse, NY, May, 1999.
- [3] Richard G. Wiley, Electronic Intelligence: The Analysis of Radar Signals, Artech House, Boston, 1982.
- [4] Clayton Paul, Introduction to Electromagnetic Compatibility, John Wiley & Sons, New York, 1992.
- [5] Magdy Iskander, Electromagnetic Fields and Waves, Prentice Hall, Englewood Cliffs, New Jersey, 1992.
- [6] Don Johnson and Dan Dudgeon, Array Signal Processing, Prentice Hall, Englewood Cliffs, New Jersey, 1993.
- [7] Nadav Levanon, Radar Principles, John Wiley & Sons, New York.
- [8] Fred E. Nathanson, Radar Design Principles, Second Edition, McGraw-Hill, Inc., New York, 1991.
- [9] John P. Costas, "A Study of a Class of Detection Waveforms Having Nearly Ideal Range-Doppler Ambiguity Properties", Proc. IEEE, Vol. 72, No. 8, August 1984, pp. 996-1009.
- [10] Solomon W. Golomb and Herbert Taylor, "Construction and Properties of Costas Arrays", Proc. IEEE, Vol. 72, No. 9, September 1984, pp. 1143-1163.
- [11] Solomon W. Golomb and Herbert Taylor, "Two-Dimensional Synchronization Patterns for Minimum Ambiguity", IEEE Trans. Information Theory, Vol. IT-28, No. 4, July 1982, pp. 600-604.
- [12] Hermann Rohling, Thomas May, Karsten Bruninghaus and Rainer Grunheid, "Broad-Band OFDM Radio Transmission for Multimedia Applications", Proc. IEEE, Vol. 87, No. 10, October 1999, pp. 1778-1789.
- [13] J. I. Marcum, "A Statistical Theory of Target Detection by Pulsed Radar", IRE Trans. Information Theory, Vol. IT-6, No. 2, April 1960, pp. 59-267.
- [14] A. H. Heatley, "A Short Table of the Toronto Functions", Trans. Royal Society of Canada, Vol. 37, Section III, 1943, pp. 13-29.
- [15] Leon Cohen, "Transformation of Operators", Journal of Mathematical Physics, Vol. 17, 1976, pp. 684-690.